Measurement of the Ratio of Branching Fractions $\mathcal{B}(B_s^0 \to D_s^- D_s^+)/\mathcal{B}(B^0 \to D^- D_s^+)$ with the CDF detector

by

Boris Iyutin

Submitted to the Department of Physics
in partial fulfillment of the requirements for the degree of

Doctor of Philosophy

at the

MASSACHUSETTS INSTITUTE OF TECHNOLOGY

March 2007

© Boris Iyutin, MMVII. All rights reserved.

The author hereby grants to MIT permission to reproduce and distribute publicly paper and electronic copies of this thesis document in whole or in part.

Author .....
Department of Physics
March 2, 2007

Certified by .....
Christoph M. E. Paus
Associate Professor
Thesis Supervisor

Accepted by .....
Thomas J. Greytak
Associate Department Head for Education, Professor

Measurement of the Ratio of Branching Fractions $\mathcal{B}(B_s^0 \to D_s^- D_s^+)/\mathcal{B}(B^0 \to D^- D_s^+)$ with the CDF detector

by

Boris Iyutin

Submitted to the Department of Physics
on March 2, 2007, in partial fulfillment of the
requirements for the degree of
Doctor of Philosophy

Abstract

In this thesis we report the measurement of ratios of branching fractions: $\mathcal{B}(B_s^0 \to D_s^- \pi^+\pi^+\pi^-)/\mathcal{B}(B^0 \to D^-\pi^+\pi^+\pi^-)$, and $\mathcal{B}(B^0 \to D^- D_s^+)/\mathcal{B}(B^0 \to D^-\pi^+\pi^+\pi^-)$, using 355 pb^{-1} of data collected by CDF detector at the Tevatron $p\overline{p}$ collider at $\sqrt{s} = 1.96$ TeV. We measure

$$\frac{\mathcal{B}(B_s^0 \to D_s^-\pi^+\pi^+\pi^-)}{\mathcal{B}(B^0 \to D^-\pi^+\pi^+\pi^-)} = 1.05 \pm 0.10 \pm 0.08 \pm 0.15(f_s/f_d) \pm 0.14(\mathcal{B}), \quad (1)$$

$$\frac{\mathcal{B}(B^0 \to D^- D_s^+)}{\mathcal{B}(B^0 \to D^-\pi^+\pi^+\pi^-)} = 1.51 \pm 0.10 \pm 0.11 \pm 0.20(\mathcal{B}). \quad (2)$$

For $B^0 \to D^{(*)-} D_s^{(*)+}$ decay modes using the same dataset we determine

$$\frac{\mathcal{B}(B^0 \to D^- D_s^{*+})}{\mathcal{B}(B^0 \to D^- D_s^+)} = 0.89 \pm 0.20 \pm 0.08, \quad (3)$$

$$\frac{\mathcal{B}(B^0 \to D^{*-} D_s^+)}{\mathcal{B}(B^0 \to D^- D_s^+)} = 1.47 \pm 0.45 \pm 0.07, \quad (4)$$

$$\frac{\mathcal{B}(B^0 \to D^{*-} D_s^{*+})}{\mathcal{B}(B^0 \to D^- D_s^+)} = 2.59 \pm 0.51 \pm 0.16. \quad (5)$$

Using the same dataset, we observe for the first time the decay $B_s^0 \to D_s^- D_s^+$ with the significance of better than 7.5 standard deviations. We measure the ratios of branching fractions

$$\frac{\mathcal{B}(B_s^0 \to D_s^- D_s^+)}{\mathcal{B}(B^0 \to D^- D_s^+)} = 1.44^{+0.38\ +0.11}_{-0.31\ -0.14} \pm 0.21(f_s/f_d) \pm 0.21(\mathcal{B}), \quad (6)$$

$$\frac{\mathcal{B}(B_s^0 \to D_s^- D_s^+)}{\mathcal{B}(B_s^0 \to D_s^-\pi^+\pi^+\pi^-)} = 2.07^{+0.56\ +0.17}_{-0.46\ -0.22} \pm 0.04(\mathcal{B}) \pm 0.27(\mathcal{B}(D_s^- \to \phi\pi^-)). \quad (7)$$

Using the ratio of branching fractions (6) and the latest world average $\mathcal{B}(B^0 \to D^- D_s^+) = (6.5 \pm 2.1) \times 10^{-3}$ [1], we measure

$$\mathcal{B}(B_s^0 \to D_s^- D_s^+) = (9.4^{+4.4}_{-4.2}) \times 10^{-3}. \tag{8}$$

We use this measurement to obtain the lower bound on the relative decay width difference between the two B_s^0 CP eigenstates

$$\Delta\Gamma_s^{\mathrm{CP}}/\Gamma_s \geq 1.2 \times 10^{-2} \text{ at } 95\% \text{ C.L.} \tag{9}$$

Thesis Supervisor: Christoph M. E. Paus
Title: Associate Professor

Contents

Chapter 1

Introduction

All the high energy experimental data gathered by now is accounted for by the Standard Model of Particle Physics [2]. According to this model, all matter is made of *fermions*, particles with spin 1/2, and all interactions between particles are carried by *bosons*, particles with integer spin. There are twelve known elementary fermions. Six of them are *quarks* and six of them are *leptons* (Table 1.1).

Particles	Charge	Spin	Generations		
quarks	$+2/3$	$1/2$	u	c	t
	$-1/3$	$1/2$	d	s	b
leptons	-1	$1/2$	e	μ	τ
	0	$1/2$	ν_e	ν_μ	ν_τ

Table 1.1: Quarks and leptons.

For every fermion particle (u, d, e^-, ν_e) there is an *antiparticle* with opposite charge $(\bar{u}, \bar{d}, e^+, \bar{\nu}_e)$. Leptons are observable as free particles while quarks, due to the nature of the strong force [3], are only observed confined within *mesons* or *baryons*. A meson is the combination of a quark and an antiquark and a baryon is the combination of three quarks. No other combinations of quarks have yet been observed despite active searches [4].

Quarks u and d, together with electron e and electron neutrino ν_e, form the first generation of elementary particles and make up most of the world's matter. The quarks of the other two generations form mesons and baryons too, but those are

unstable and it takes them a fraction of a second to decay into lighter particles made of u and d quarks. Table 1.2 shows the quark content of some of the particles mentioned later in this thesis.

	baryons		mesons							
Particle	p	n	π^+	π^-	K^+	K^0	D^-	D_s^-	B^0	B_s^0
Quark content	uud	udd	$u\bar{d}$	$\bar{u}d$	$u\bar{s}$	$\bar{s}d$	$\bar{c}d$	$\bar{c}s$	$b\bar{d}$	$b\bar{s}$

Table 1.2: Some baryons and mesons.

There are four known fundamental types of interactions: electromagnetic, weak, strong, and gravity. Each of them is carried by a mediator particle (Table 1.3).

Particle	Spin	Interaction
γ - photon	1	electroweak
$W^{\pm}, Z^0$	1	
G - gluon	1	strong
g - graviton	2	gravity

Table 1.3: Interaction carriers.

Gravitational interaction [5] is mediated by as yet unconfirmed *graviton* and appears between particles with mass. It is very weak and only becomes noticeable on the astronomical scale when masses of the interacting objects become very large. *Electromagnetic* interaction [6] is between electrically charged particles. It is mediated by *photons* and is responsible for most of the common life phenomenas.

Strong and weak interactions are bound to atomic scales. The *strong* interaction is responsible for binding quarks into mesons and baryons, and holding the nucleus together in the atom. Described by quantum chromodynamics [7], it has three color-charges (red, green, and blue) and is mediated by *gluons*. There are no long range strong forces because stable combinations of quarks do not carry color charge. Mesons are made of the combination of two quarks with a given color and its corresponding anti color. Baryons are made of three quarks of three different colors which gives the superposition of white.

The *weak* interaction is mediated by massive, hence short-ranged, $W^{\pm}$ [8] and

Z^0 [9] bosons. Quarks and leptons can change flavor via $W^{\pm}$ boson exchange. The decay modes of B mesons, studied in this thesis, give us additional insight into the nature of the weak interaction.

1.1 Weak Interactions and the CKM Matrix

The weak interaction enables quarks to change flavor and makes it possible for heavier mesons and baryons to decay into lighter ones, releasing energy. Table 1.4 shows the examples of meson decays with the revealed quark content of the reactions.

Meson decay	Quark content
$\phi \to K^+K^-$	$\overline{s}s \to \overline{s}u + s\overline{u}$
$D^- \to K^+\pi^-\pi^-$	$\overline{c}d \to s\overline{u} + d\overline{u} + d\overline{u}$
$D_s^- \to \phi\pi^-$	$\overline{c}s \to s\overline{s} + d\overline{u}$
$B_s^0 \to D^-D_s^+$	$\overline{b}s \to \overline{c}d + c\overline{s}$
$B_s^0 \to D_s^-D_s^+$	$\overline{b}s \to \overline{c}s + c\overline{s}$

Table 1.4: Heavy flavored mesons decaying into lighter mesons.

In the decay $D_s^- \to \phi\pi^-$, for example, the $\overline{c}$ quark from the D_s^- meson changes its flavor to an $\overline{s}$ quark with a release of virtual W^- boson (here and below the charge conjugate decay is alsways implied). The dominant diagram for this decay is shown on Figure 1-1.

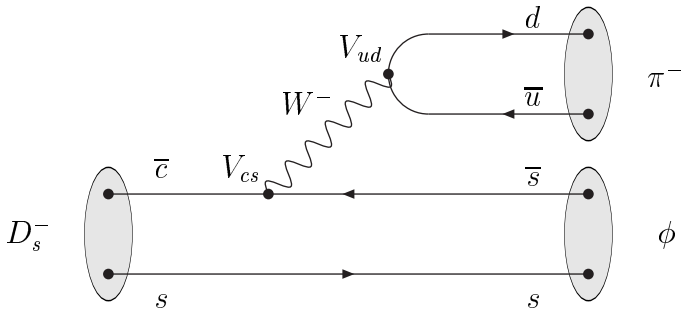

Figure 1-1: Color allowed "Tree" diagram for $D_s^- \to \phi\pi^-$ decay.

The flavour changing transitions between quarks are mediated by a $W^\pm$ boson. The probabilities of these transitions are defined by the Cabibbo-Kobayashi-Maskawa (CKM) matrix [10]. The elements of the CKM matrix (1.1) enter the calculations of the branching amplitudes as vertex factors as shown on Figure 1-1.

$$\mathbf{V} = \begin{pmatrix} V_{ud} & V_{us} & V_{ub} \\ V_{cd} & V_{cs} & V_{cb} \\ V_{td} & V_{ts} & V_{tb} \end{pmatrix}. \tag{1.1}$$

From 9 real parameters of a general 3×3 unitary matrix, 5 parameters of the CKM matrix are unobservable and subject to convention. They can be absorbed in 1 global phase, 2 relative phases between u,c,t, and 2 relative phases between d,s,b. The 4 independent parameters usually treated as 3 angles, defining rotations in 3 dimensional quark space, and one CP-violating imaginary parameter

$$\begin{pmatrix} c_x c_z & s_x c_z & s_z e^{-i\phi} \\ -s_x c_y - c_x s_y s_z e^{-i\phi} & c_x c_y - s_x s_y s_z e^{-i\phi} & s_y c_z \\ s_x s_y - c_x c_y s_z e^{-i\phi} & -c_x s_y - s_x c_y s_z e^{-i\phi} & c_y c_z \end{pmatrix}. \tag{1.2}$$

where x, y and z, are the rotation angles, ϕ is the phase, and c_x and s_x are standing for $\cos(x)$ and $\sin(x)$. A common parametrization for the CKM matrix given by Wolfenstein [11] defines four independent parameters: λ, A, ρ and η as $\sin(x) = \lambda \approx 0.22$, $\sin(y) = A\lambda^2$, and $\sin(z)e^{-i\phi} = A\lambda^3(\rho + i\eta)$. Expanded to the term of the order of λ^4 it could be written as

$$\mathbf{V} = \begin{pmatrix} 1 - \frac{\lambda^2}{2} & \lambda & A\lambda^3(\rho - i\eta) \\ -\lambda & 1 - \frac{\lambda^2}{2} & A\lambda^2 \\ A\lambda^3(1 - \rho - i\eta) & -A\lambda^2 & 1 \end{pmatrix} + O(\lambda^4). \tag{1.3}$$

The matrix has complex terms of the order of $A\lambda^3$, which have very important implications to symmetry breaking. Electromagnetic and QCD processes in the particle physics are symmetric under the exchange of particles with antiparticles (C -symmetry) and under the change of right-hand space with the left-hand space (P-symmetry). The simultaneous CP-symmetry is also preserved in most of the physics processes. The weak interaction violates C and P symmetries in the strongest possible way. For example, a $W^{\pm}$ boson couples to the electron with left-handed spin e^-_L or positron with right-handed spin e^+_R. It does not couple to to left-handed positron -

e_L^+ or right-handed electron - e_R^-. While C and P symmetries are separately violated by the weak interaction, the combined CP-symmetry stays preserved for many weak processes. However, in general, CP-symmetry is also violated.

Within the Standard Model, CP-violation is described by the complex phase ϕ of the CKM matrix. It gives a W-boson a CP-violating coupling to up-type antiquark and down-type quark. It is illustrated by writing the unitarity condition of the CKM matrix $\mathbf{V}\mathbf{V}^\dagger = 1$

$$\sum_j V_{ij} V_{kj}^* = \delta_{ik}. \tag{1.4}$$

For $(i \neq k)$, the equations represent connected triangles in the complex plane because three vectors add up to zero. The area of the triangle is proportional to the contribution of the complex phase and the CP-violating effect.

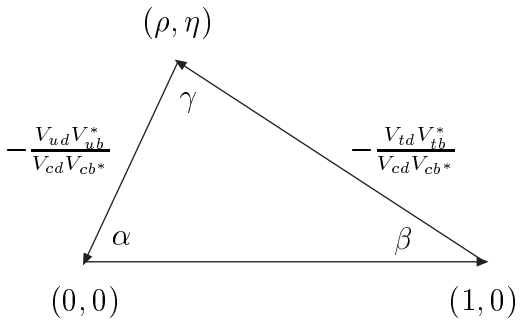

Figure 1-2: The Unitarity Triangle in the complex plane.

One of the triangles is particularly well studied due to the fortunate conditions making its sides roughly equal:

$$V_{ud}V_{ub}^* + V_{cd}V_{cb}^* + V_{td}V_{tb}^* = 0. \tag{1.5}$$

This equation defines the Bjorken (Unitarity) Triangle [12]. Its graphical representation in the complex plane is shown on Figure 1-2. In Wolfenstein parametrization it is given as

$$A\lambda^3(\rho + i\eta) - A\lambda^3 + A\lambda^3(1 - \rho - i\eta) = 0. \tag{1.6}$$

One side of the triangle has been measured by the recent observation of B_s-mixing at CDF [13]. The $B_s^0 \to D_s^- \pi^+ \pi^+ \pi^-$ modes, reconstructed in this analysis, improve the statistical power of the sample of fully reconstructed hadronic modes, used for B_s^0-mixing observation at CDF. Figure 1-3 shows the diagrams for the $\overline{B_s^0} \to B_s^0$ transition.

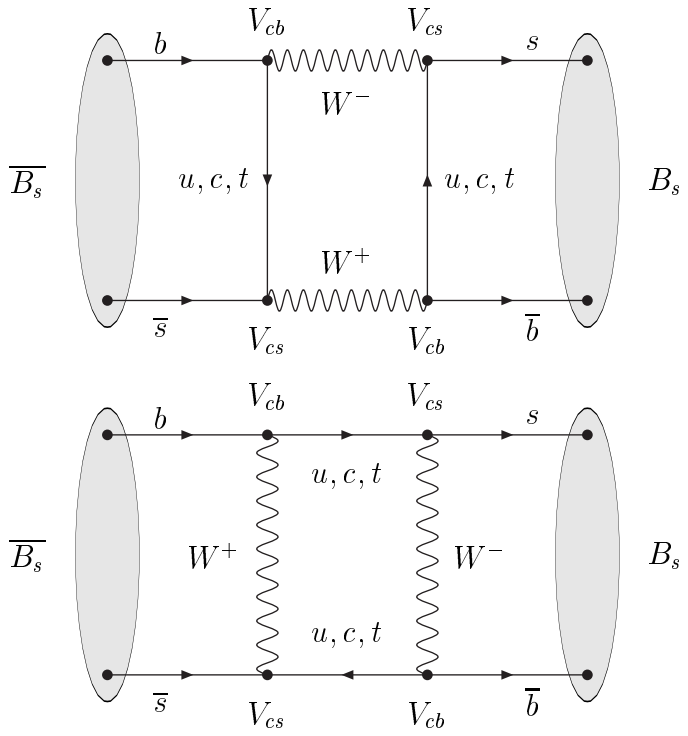

Figure 1-3: Diagrams for $\overline{B_s^0} \to B_s^0$ transition.

The B_s^0 system rapidly oscillates between two mass eigenstates B_s^H and B_s^L with the mass difference Δm_s defined as $\Delta m_s = m_s^H - m_s^L$. The widths of the states are conventionally denoted as Γ_s^L and Γ_s^H and are used to define the observables

$$\Gamma_s = \frac{\Gamma_s^H + \Gamma_s^L}{2}, \ \Delta\Gamma_s = \Gamma_s^L - \Gamma_s^H. \tag{1.7}$$

In CP basis with $CP|B_s^0\rangle = -|\overline{B_s^0}\rangle$ the system has CP eigenstates

$$|B_s^{even}\rangle = \frac{1}{\sqrt{2}}(|B_s^0\rangle - |\overline{B_s^0}\rangle), \ |B_s^{odd}\rangle = \frac{1}{\sqrt{2}}(|B_s^0\rangle + |\overline{B_s^0}\rangle). \tag{1.8}$$

The time evolution of the system is described by the Schrödinger equation

$$i\frac{\partial}{\partial t}\begin{pmatrix} |B_s^0\rangle(t) \\ |\overline{B_s^0}\rangle(t) \end{pmatrix} = \left(\mathbf{M} - \frac{i}{2}\mathbf{\Gamma}\right) \times \begin{pmatrix} |B_s^0\rangle(t) \\ |\overline{B_s^0}\rangle(t) \end{pmatrix}. \tag{1.9}$$

With the mass matrix $\mathbf{M} = \mathbf{M}^\dagger$, decay matrix $\mathbf{\Gamma} = \mathbf{\Gamma}^\dagger$, and the off-diagonal elements $\Gamma_{12} = \Gamma_{12}^*$ corresponding to $B_s^0 - \overline{B_s^0}$ mixing. The two mass eigenstates are expected to be eigenstates of CP to a good approximation, so that $\Delta\Gamma_s \approx \Delta\Gamma_s^{\rm CP}$, with $\Delta\Gamma_s^{\rm CP} = \Gamma(B_s^{even}) - \Gamma(B_s^{odd})$ by definition. It is shown [14] that

$$\Delta\Gamma_s = \Delta\Gamma_s^{\rm CP}\cos\phi, \quad \text{where} \quad \Delta\Gamma_s^{\rm CP} \equiv 2|\Gamma_{12}| = (\Gamma(B_s^{\rm even}) - \Gamma(B_s^{\rm odd})). \tag{1.10}$$

where ϕ is the $B_s^0 - \overline{B_s^0}$ mixing phase. The relation 1.10 is derived assuming that Γ_{12} is dominated by a single weak and predominantly CP-even phase $b \to c\overline{c}s$, with the biggest contribution from $B_s^0 \to D_s^{(*)+}D_s^{(*)-}$. It is possible then to indirectly constrain $\Delta\Gamma_s^{\rm CP}/\Gamma_s$ lower bound by measuring the branching fraction of $B_s^0 \to D_s^- D_s^+$ decay.

$$\frac{\Delta\Gamma_s^{\rm CP}}{\Gamma_s} \equiv \frac{2|\Gamma_{12}|}{\Gamma_s} = \frac{(\Gamma(B_s^{\rm even}) - \Gamma(B_s^{\rm odd}))}{\Gamma_s} \geq 2(\mathcal{B}(B_s^0 \to D_s^{(*)-}D_s^{(*)+})). \tag{1.11}$$

The lower bound estimate was previously reported using inclusive $B_s^0 \to \phi\phi X$ [15]. The most recent theoretical prediction for the ratio [14, 16] is

$$\frac{\Delta\Gamma_s^{\rm CP}}{\Gamma_s} = 0.12 \pm 0.06. \tag{1.12}$$

1.2 Theory of Hadronic B Decays

Strong interactions described by quantum chromodynamics (QCD) [3], do not distinguish the flavors of the quarks and are only affected through kinematics by the different masses of the quarks with different flavors. There is a vast difference between the "light" and "heavy" quark masses as shown in Table 1.5.

	"light"			"heavy"		
Quark	d	u	s	c	b	t
Mass MeV/c^2	3	5	150	1500	4500	171000

Table 1.5: Light and heavy quarks [17].

Typical energy exchanges in quark interactions via color fields are of the order of $\Lambda_{QCD} \sim 200$ MeV [18], which is much less than the masses of the "heavy" quarks. In this environment, "heavy" quarks are approximated as static sources of color fields. Therefore, the properties of the meson do not depend on the flavor of the "heavy" quark in the meson. For example, the mass difference between the D_s^- and D^- mesons compared to mass difference between B_s^0 and B^0 mesons is the same within 10% [19].

Interacting "light" quarks cannot be treated the same way since their masses are comparable to the energy exchange during the interaction. However, non-interacting (spectator) "light" quarks do not affect the decay properties of mesons. The small differences between the masses of the light quarks introduce small corrections to the decay branching fractions of mesons.

The "heavy" and the "light" quark symmetries allow us to cancel out most of the QCD effects by studying carefully constructed ratios of branching fractions. As a positive side effect, many experimental systematic uncertainties are also canceled in the ratios. In this thesis we study several ratios of branching fractions:

$$\frac{\mathcal{B}(B_s^0 \to D_s^- \pi^+ \pi^+ \pi^-)}{\mathcal{B}(B^0 \to D^- \pi^+ \pi^+ \pi^-)}, \tag{1.13}$$

$$\frac{\mathcal{B}(B^0 \to D^- D_s^+)}{\mathcal{B}(B^0 \to D^- \pi^+ \pi^+ \pi^-)}, \tag{1.14}$$

$$\frac{\mathcal{B}(B_s^0 \to D_s^- D_s^+)}{\mathcal{B}(B^0 \to D^- D_s^+)}, \tag{1.15}$$

$$\frac{\mathcal{B}(B_s^0 \to D_s^- D_s^+)}{\mathcal{B}(B_s^0 \to D_s^- \pi^+ \pi^+ \pi^-)}. \tag{1.16}$$

where $D_s^- \to \phi\pi^-, K^{*0}K^-, \pi^+\pi^-\pi^-$, and $D^- \to K^+\pi^-\pi^-$.

The decay modes used in the ratios above have six tracks in the final state and similar topologies. For each mode the B meson decays into two secondary resonances. Each of the secondary particles decay into three long-lived particles, kaons or pions. The use of the same D_s^- and D^- decay channels allows one to optimize the reconstruction procedure and reduce the systematic uncertainty.

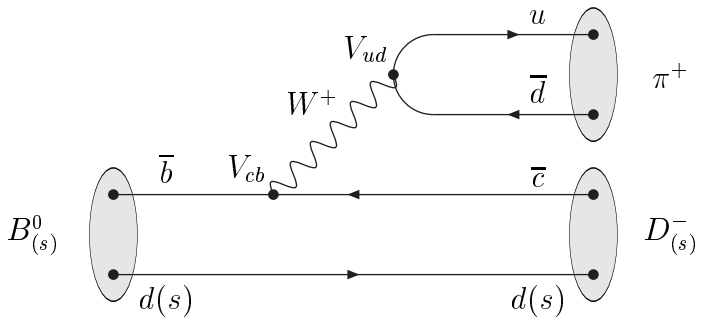

Figure 1-4: "Tree" diagram for $B^0 \to D^-\pi^+$ and $B_s^0 \to D_s^-\pi^+$ decays.

The ratio of branching fractions (1.13) is very similar to the ratio $\mathcal{B}(B_s^0 \to D_s^-\pi^+)/\mathcal{B}(B^0 \to D^-\pi^+)$, with $D_s^- \to \phi\pi^-$, and $D^- \to K^+\pi^-\pi^-$, studied before at CDF [20]. In the leading diagram, shown on Figure 1-4, the light quark of the B meson does not interract and stays as a "spectator". By using the "light" quark symmetry, we would expect the ratio of the branching fractions to be equal to one.

Apart from the "light" quark symmetry not being exact, due to the differences in masses of d quark and s quark, there is also a diagram shown in Figure 1-5, which contributes to the $B^0 \to D^-\pi^+$ decay mode, but not to the $B_s^0 \to D_s^-\pi^+$ decay mode. The colors of the quarks in the internal pair on Figure 1-5 are required to match the colors of the quarks in the external pair in order to produce color neutral mesons. This

requirement suppresses the amplitude of the diagram by a factor of $(1/3)^2$, where 3 is a number of the QCD colors, hence the name "color suppressed". The requirement is not applied to the diagram on Figure 1-4, where the quarks emerge from the color neutral W^+ boson with their colors matched, and form a color neutral π^+ meson. A similar diagram for $B_s^0 \to D_s^- \pi^+$ decay contains a V_{us} vertex, which suppresses the contribution of the diagram by a factor of $\lambda^2 \approx 1/20$ and makes it negligible.

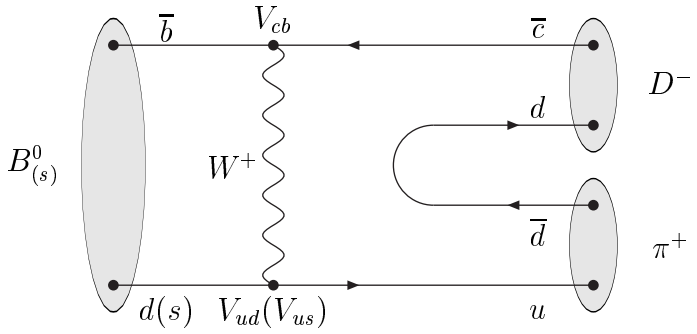

Figure 1-5: Color suppressed "W-exchange" diagram for $B^0 \to D^- \pi^+$ decay.

Similar diagrams exist for $B^0 \to D^- \pi^+ \pi^+ \pi^-$and $B_s^0 \to D_s^- \pi^+ \pi^+ \pi^-$with the addition of a $\pi^+ \pi^-$ pair emerging from the vacuum. The "tree" diagram (Figure 1-6) contributes to both B^0 and B_s^0 decays. The color suppressed "W-exchange" diagram (Figure 1-7) contains a V_{us} vertex for $B_s^0 \to D_s^- \pi^+ \pi^+ \pi^-$decay mode. It makes this diagramm negligible by suppressing its contribution for this mode by a factor of λ^2.

There is experimental evidence [21, 22] that the $B_{(s)}^0 \to D_{(s)}^- a_1^+$, followed by $a_1^+ \to \pi^+ \pi^+ \pi^-$ dominates the $B_{(s)}^0 \to D_{(s)}^- \pi^+ \pi^+ \pi^-$ decay. The absolute branching fraction for $B_{(s)}^0 \to D_{(s)}^- V$, where V is a vector meson, is calculated in [23].

For "double-charm" B meson decays, the "Tree" diagram shown on Figure 1-8 makes a leading contribution to both $B^0 \to D^- D_s^+$ and $B_s^0 \to D_s^- D_s^+$ decay modes. The "W-exchange" diagram shown on Figure 1-9 only contributes to the $B_s^0 \to D_s^- D_s^+$ decay mode.

The ratios of the branching fractions $\mathcal{B}(B_s^0 \to D_s^- \pi^+ \pi^+ \pi^-)/\mathcal{B}(B^0 \to D^- \pi^+ \pi^+ \pi^-)$ and $\mathcal{B}(B_s^0 \to D_s^- D_s^+)/\mathcal{B}(B^0 \to D^- D_s^+)$ are expected to be close to 1, assuming flavor symmetry and that the contribution from the subleading diagrams in the $B_{(s)}^0 \to D_{(s)}^- \pi^+ \pi^+ \pi^-$ and $B_{(s)}^0 \to D_{(s)}^- D_s^-$ decay modes is small.

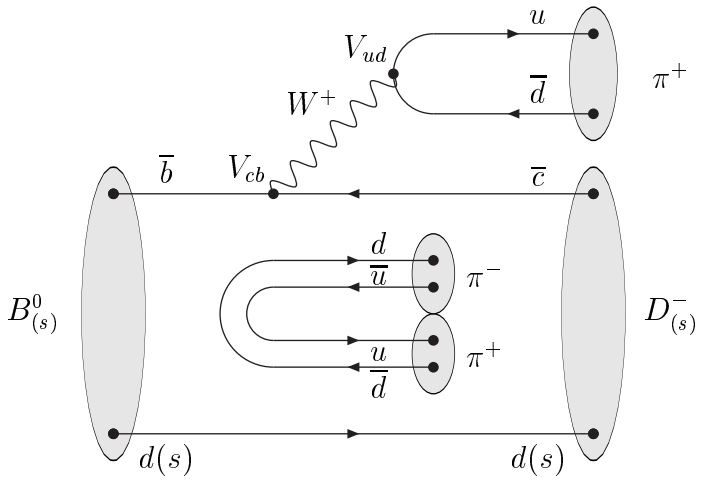

Figure 1-6: "Tree" diagram for $B^0 \to D^-\pi^+\pi^+\pi^-$ and $B_s^0 \to D_s^-\pi^+\pi^+\pi^-$ decays.

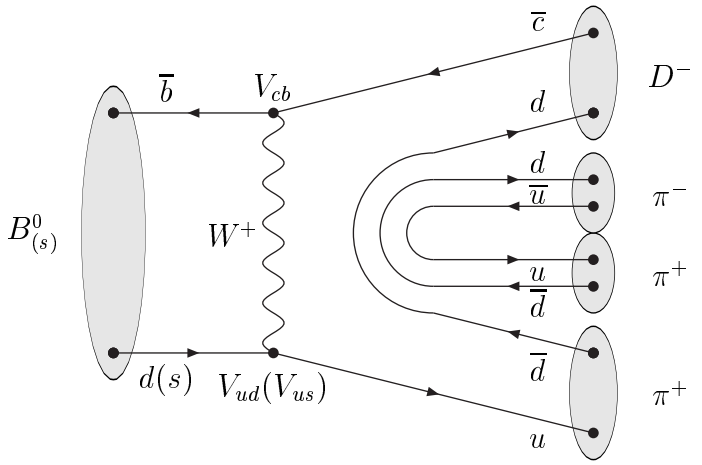

Figure 1-7: Color suppressed "W-exchange" diagram for $B^0 \to D^-\pi^+\pi^+\pi^-$ decay.

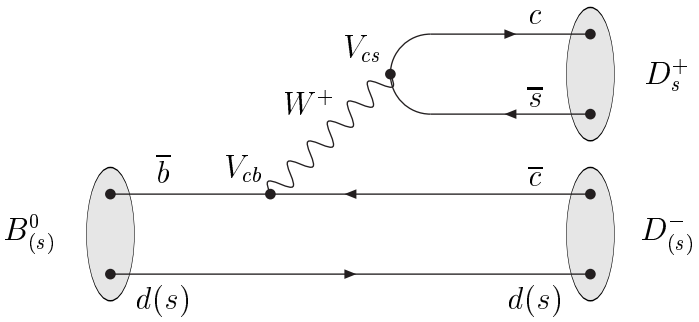

Figure 1-8: "Tree" diagram for $B^0 \to D^- D_s^+$ and $B_s^0 \to D_s^- D_s^+$ decays.

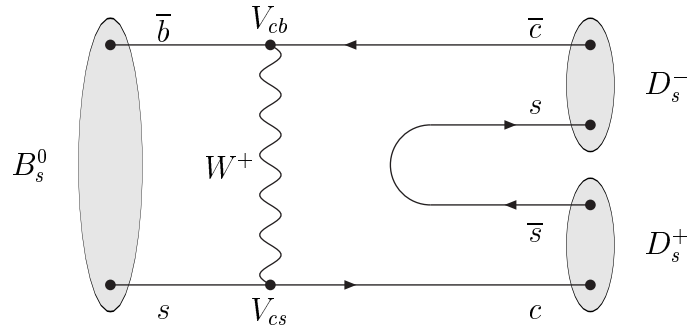

Figure 1-9: Color suppressed "W-exchange" diagram for for $B_s^0 \to D_s^- D_s^+$ decays.

Chapter 2

Experimental Apparatus

2.1 Fermilab Tevatron

The Fermi National Accelerator Laboratory, one of the worlds largest experimental physics facilities, hosts the most powerful operating hadron collider called Tevatron. Fermilab Tevatron, which allowed the discovery of b and t quarks [24, 25], currently produces proton-antiproton collisions with a center of mass energy of 1.96 TeV. The simplified sketch of the collider is shown on Figure 2-1.

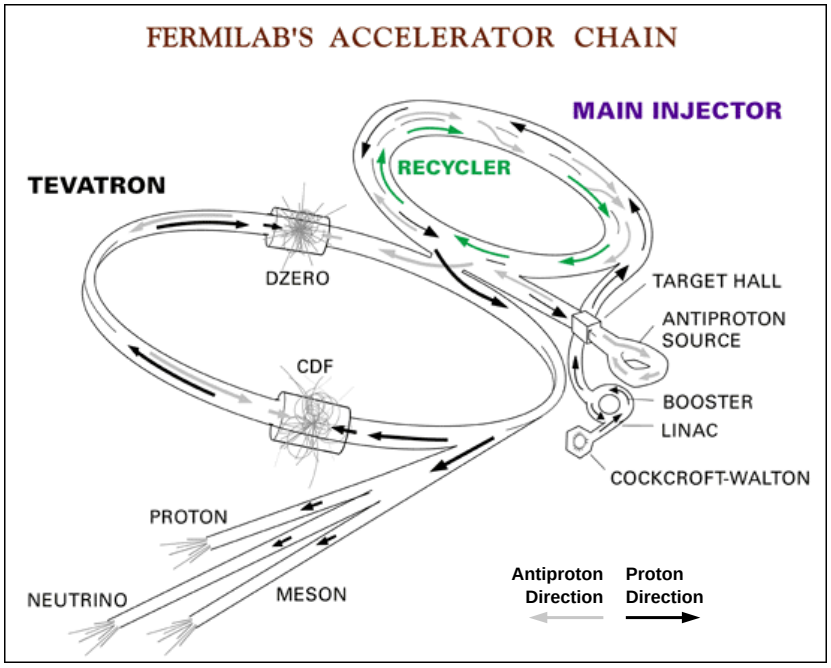

Figure 2-1: Fermilab Tevatron.

After a sophisticated multistage acceleration process the unpolarized bunches of protons and antiprotons are collided at the rate of 2.5 million bunch crossings per second with the record instantaneous luminosity reaching $1.4 \times 10^{32}\text{cm}^{-2}\text{s}^{-1}$ [26]. The collision region has a Gaussian longitudinal density profile with R.M.S. about 30 cm. The collisions happen between the quark constituents of the hadrons (partons) carrying only a part of the hadron momentum. To avoid ambiguity due to the unknown parton momentum in the longitudinal direction, CDF physics analyzes use the quantities defined in the transverse plane.

2.2 CDF Detector

This analysis uses data recorded by the CDF detector installed in one of the collision points of the Tevatron. The CDF detector is shown on Figure 2-2. It is designed to measure the properties of particles formed in the $p\overline{p}$ collisions and reconstruct their kinematic properties. The design of the detector is a compromise between different physics requirements. The detailed description of the apparatus is given in the Technical Design Report [26]. This analysis relies on the performance of the tracking system which has a cylindrical design with the Tevatron beampipe as the axis and the collision point in the center of the symmetry. Tracking system consist of the Silicon Vertex Tracker (SVX), located on the beam pipe and is surrounded by the Central Outer Tracker (COT). Both tracking devices are submerged into a 1.4 T magnetic field, generated by the superconducting solenoidal magnet.

The CDF detector uses a cylindrical coordinate system with the origin in the center of the detector. In this system, ϕ is the azimuthal angle, r is the radius from the symmetry axis, y points up and z points in the direction of the proton beam. The transverse plane is the plane perpendicular to the z axis.

Particles emanating from the collision point in the magnetic field follow helical trajectories. Passing through the tracking volumes, charged particles ionize the material along the track. Sensitive coordinate detectors of the tracking systems register and digitize the signals induced by the ionized trace. The CDF data acquisition system

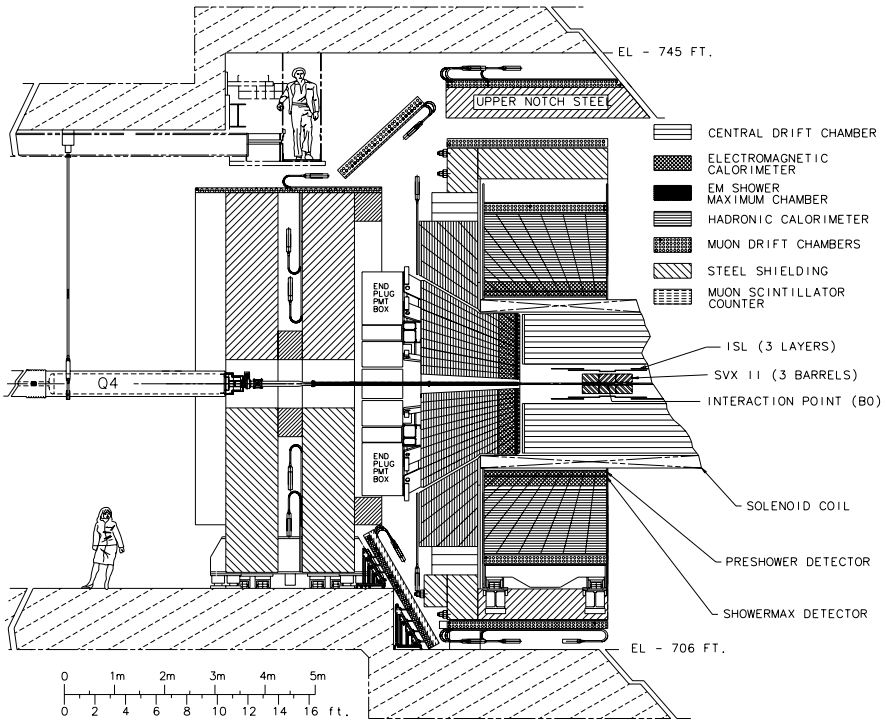

Figure 2-2: The CDF detector.

(DAQ) reads the digitized signals for later use in the reconstruction of the particle trajectories.

The success of this analysis depends on the ability of the detector to precisely measure the coordinates of the tracks in the vicinity of their origin, and also on the ability to define the curvature of the track with high accuracy, which allow the precise measurement of the particle momentum. The silicon micro-strip detectors located right on the beampipe are the closest to the primary vertex and the most precise (Figure 2-3). The CDF Silicon VerteX Detector, SVX [26], is composed of L00 (single layer of silicon placed close to the beam pipe) [27], SVX II (five cylindrical layers of double-sided sensors) [28], and ISL (outermost layer of silicon) [29], providing up to 8 coordinate measurements in the r-ϕ view [30]. Charged particles traveling through silicon wafers interact with the material, creating small ionized clusters in the semiconductor. The position of the clusters is recorded with high accuracy and used later for track reconstruction.

Around the silicon detector there is a Central Outer Tracker `COT` [26] - a cylindrical

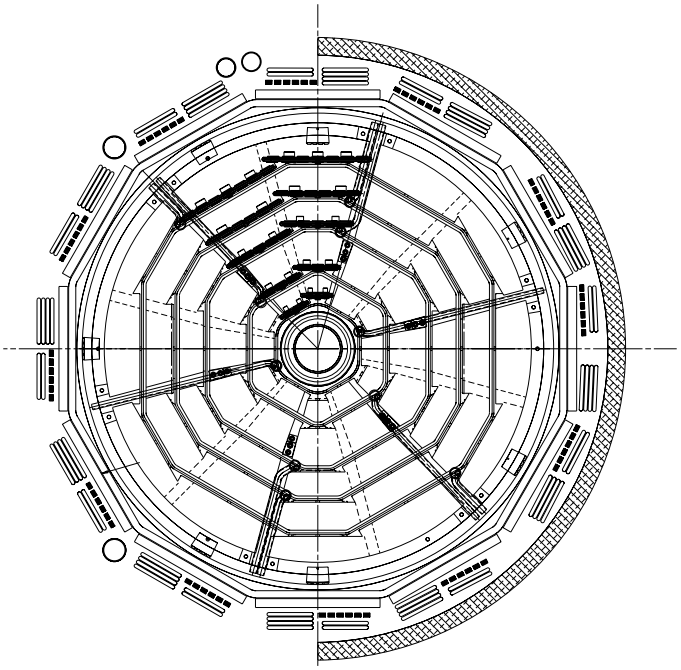

Figure 2-3: The SVX detector.

multi-wire open-cell drift chamber. A particle traveling through the Argonne-Ethane gas mixture leaves a trail of ionized atoms and electrons. Free electrons drift to the sense wires driven by the electric field created by an intricate system of cathode panels and potential wires. Figure 2-4 shows the endplate of the drift chamber with tilted wire planes organizing 96 layers of wires into 8 superlayers. In superlayers 2,4,6, and 8, called *stereo layers*, the wires are tilted with respect to the endplane. It allows the measurement of a z position of the track with a resolution of about 1 cm.

The precise determination of track parameters makes it possible to distinguish the secondary vertices of the particles with lifetime (B and D mesons) from the overwhelming combinatorial background originating from the primary vertex. Using the unique impact parameter resolution, the CDF trigger system, which is described in the next chapter, enriches the data sample with long-living particles by looking for the displacements of tracks.

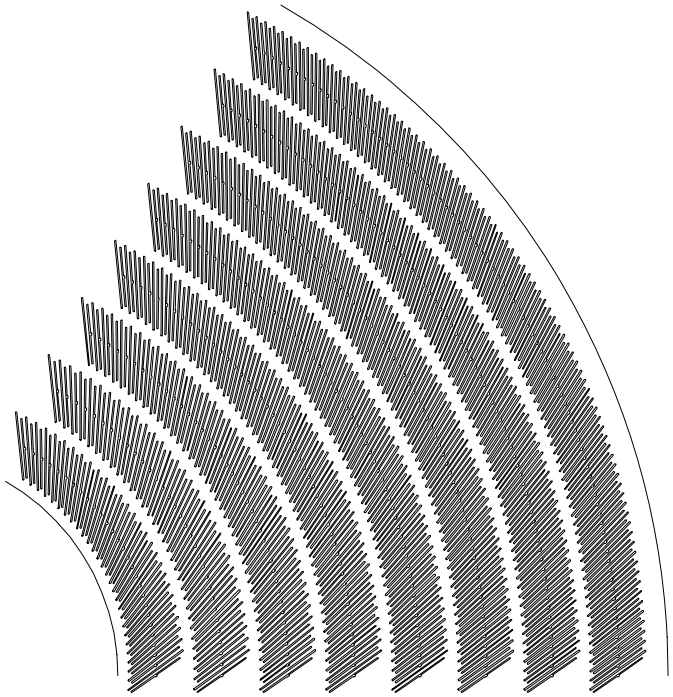

Figure 2-4: COT detector endplate.

2.3 The CDF DAQ System

At about 2.5 million collisions in the center of the detector the CDF trigger system plays an important role in choosing the most promising collision events online, and allow to store data on tape at the rate of about a hundred events per second. The three-level CDF trigger system relies on pipelined architecture to parallelize the processing of the events. While events are stored in the pipline buffers, trigger algorithms implemented at Level1 and Level2 use tiny pieces of event information such as track multiplicity or missing transverse energy to chose interesting events. Trigger criterias become more sophisticated as event makes its way through the trigger filters. As a result the the event rate after Level2 goes down to about 300 events per second.

While Level1 and Level2 are making their decision based on the partial event information, the event fragments from the detector systems are stored in $\approx$150 Front End (FE) crates. If the Level2 decides to keep the event, the Event Builder reads the event fragments from the Front End crates, puts them together and sends the event to the Level3 [31].

Level3 receives an event from the Event Builder and makes a final trigger decision based on the full event information. Events which pass Level3 are sent to the storage facility with a small fraction of events distributed to the monitors in the Control Room, where the shift crew supervises the quality of the incoming data.

2.4 CDF Trigger System

CDF detector is a flexible multipurpose tool which enable a wide variety of physics analyzes. The flexibility is achieved by using a large number of different triggers. *Trigger* is a set of the requirements applied to the event at one of the levels of the CDF DAQ system. Every event has a set of trigger bits to keep count of the triggers it passed.

A set of consequent Level1, Level2 and Level3 triggers is called a *trigger path*. Only those events which have all of the required Level1, Level2 and Level3 bits can pass the trigger path. A given trigger path is intended to determine potentially interesting events for a particular type of physics (top-quark physics, QCD-physics, b-physics etc.). To accommodate the different physics interests, several trigger paths are used at the same time and all compete for DAQ bandwidth. For this analysis, we use events which pass the so called `B_CHARM` and `B_CHARM_LOWPT` trigger paths tuned to select B mesons.

The mechanism called *prescale* is designed to control the high input rates from the detector. It allows to avoid overload of the trigger system by discarding events randomly at Level1. We define the prescale rate as a number of events after the prescale divided by the number of the input events. Figure 2-5 illustrates the prescale, which by our definition can not be larger than 1.0.

A collection of trigger paths and prescales used for data taking is called a *trigger table*. The trigger table structure and preferences are the result of a sophisticated compromise between multiple physical and technical requirements. Several trigger tables designed for different instantaneous luminosities are used for different data taking regimes. The trigger table is enforced by the Trigger Supervisor and Level3

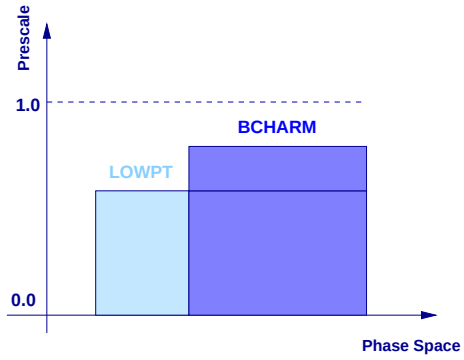

Figure 2-5: Trigger prescale versus generalized phase space of data samples passing `B_CHARM` and `B_CHARM_LOWPT` triggers.

filter.

At Level1 tracks are reconstructed using COT hits by the track trigger processor XFT [32]. XFT is used to determine transverse momentum of the track (p_T) from track curvature and the azimutal angle of the track (ϕ). The Level2 silicon vertex tracker SVT [33] associates SVXII r-ϕ position measurements with XFT tracks, providing a precise measurement of the track impact parameter (d_0), i.e. the distance of the closest approach of the track helix to the beam axis in the transverse plane. The complete event is used by the Level3 trigger for event reconstruction applying Level1 and Level2 selection cuts to the offline quality quantities. The summary of the selection requirements at different trigger levels for the `B_CHARM` trigger path is given below:

- Level1
  - two XFT tracks with opposite charge (*trigger pair*),
  - each of the two tracks has $p_T > 2.0$ GeV/c,
  - for the same two tracks $p_{T1} + p_{T2} > 5.5$ GeV/c, and the opening angle between the two tracks $0^\circ \leq |\Delta\phi| \leq 135^\circ$.
- Level2
  - two SVT (Silicon Vertex Tracker) tracks should match XFT tracks,
  - each of the two tracks has $p_T > 2.0$ GeV/c,

- for the same two tracks $p_{T1} + p_{T2} > 5.5$ GeV/c, and the opening angle between the two tracks $2^\circ \leq |\Delta\phi| \leq 90^\circ$,
- impact parameter (d_0) of each of the two tracks $0.12\text{mm} \leq d_0 \leq 1\text{mm}$,
- two-track vertex with $L_{xy} > 0.2$ mm,
- goodness of SVT vertex fit $\chi^2 < 25$.

where L_{xy} is defined as the distance in the transverse plane from the beam line to the two-track vertex projected onto the two-track momentum vector. The `B_CHARM_LOWPT` trigger path is very similar to the `B_CHARM` trigger path, but does not require the opposite charge of the *trigger pair* tracks and does not apply the selection based on the scalar sum of the transverse momenta.

While Level1 and Level2 systems are making their decisions, the disjointed pieces of event data are waiting in the Front End crates. The Trigger Supervisor controls the decision making process. It receives Level1 and Level2 trigger bits for each event and makes a final Level2 decision based on the trigger table used for the data taking.

When the Level2 decision is made, the Trigger Supervisor sends a confirmation to the controlling entity of the Event Builder called the Scanner Manager. Following the commands of the Scanner Manager, the Event Builder crates fetch data packets from all the Front End crates and assemble them. The assembling is a two-stage process which could be followed using Figure 2-6.

1. Event pieces from Front End crates are loaded to 15 Event Builder crates.

2. 15 event fragments from Event Builder crates are sent to *one* of 16 Level3 *subfarms* where the event is reconstructed and processed.

Level3 operations start at the point where the Event Builder operations are done. We use a computer farm of 300 dual CPU Linux computers (nodes) to parallelize the processing of the events. Each of the 300 computers runs an instance of Level3 filter code on each of two CPUs and processes two events in parallel. The Level3 designed input rate is about 300 events per second and the output rate is about 75 events per

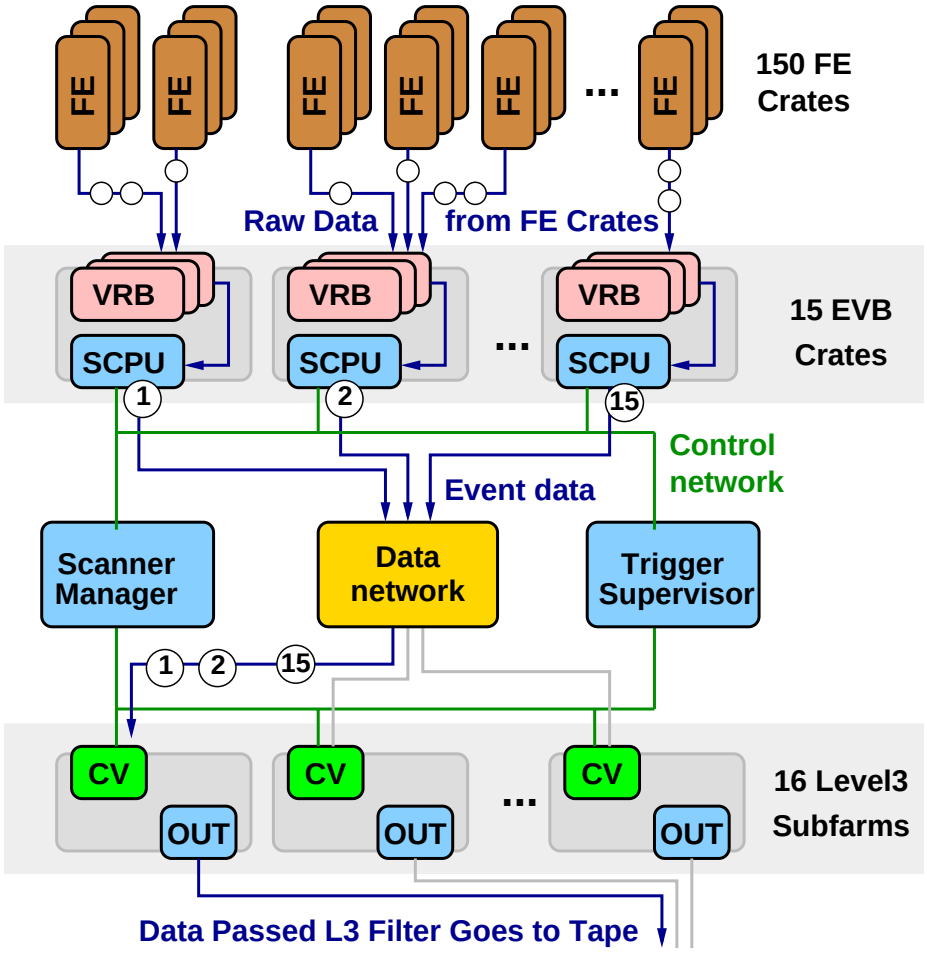

Figure 2-6: Event Builder block diagram. The arrows show the data flow with white circles representing the event fragments. Event Builder (EVB) crates assemble small pieces of event data from Front End (FE) crates into bigger chunks (circles with 1, 2, 15 on the picture). All the chunks for one event are sent to one of the converter nodes (CV) of the subfarm where the whole event is assembled. The control network is used by the Scanner Manager of the Event Builder to communicate with the Trigger Supervisor and synchronize the data flow between Event Builder crates and Level3 subfarms.

second. Both rates almost quadrupled over the years of data taking due to multiple upgrades.

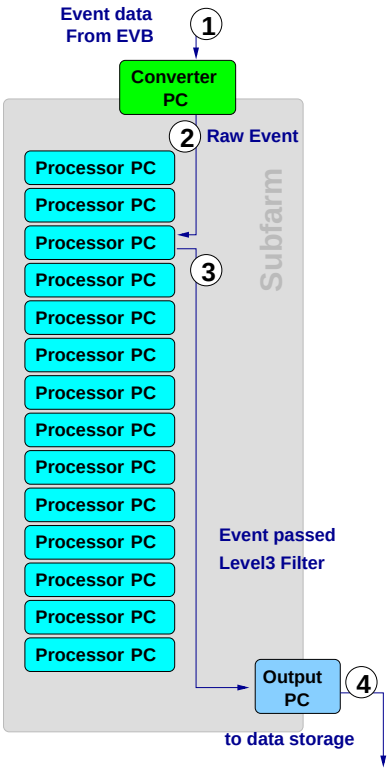

Figure 2-7: Level3 subfarm operations. (1) Event Builder data fragments arrive at the converter node. (2) Converter node puts data fragments together and sends Raw Event to a free processor node. (3) Processor node reconstructs event, applies Level3 filter and sends passed events to the output node. (4) Output node sends event to the offline data storage.

For modularity and maintenance purposes, the Level3 computer farm is divided into 16 roughly equal subfarms of 14-20 processor nodes each (Figure 2-7). 16 nodes (one per subfarm) called *converter* nodes serve as Level3 input. Each converter node also serves as a coordinator for one subfarm. It distributes events over the subfarm evenly by choosing processor nodes in a Round-Robin fashion, skipping busy or broken nodes. 8 nodes called *output* nodes are dedicated to the output task of sending events which passed the Level3 trigger to the data storage.

The Level3 farm reconstructs the event and applies a software trigger repeating trigger table requirements. For `B_CHARM` trigger path Level3 filter repeats Level2 requirements using offline quality track parameters and applies cut on the longitudional

displacement (Δz) of two trigger tracks $\Delta z < 5$cm to discard events with multiple collisions.

Events which passed Level3 are sent to the offline storage facility where data goes through the quality checks and a round of physics dependent offline reconstruction. The reconstructed datasets are stored on tape and available for the use of the collaboration. In this analysis we use the hadronic dataset, which gets its name because it is rich in long-living b and c hadrons.

Chapter 3

Data Samples and Offline Production

3.1 Datasets and Run Ranges

In this thesis we present the analysis performed using a data sample selected by the displaced track trigger at CDF. The sample represents 355 pb^{-1} integrated luminosity of Tevatron $p\bar{p}$ collisions at $\sqrt{s} = 1.96$ TeV. Hadronic decay modes are reconstructed using the data set which passed the `B_CHARM` and the `B_CHARM_LOWPT` trigger paths introduced in Section 2.4. Adding `B_CHARM_LOWPT` trigger data to our dataset improves the statistical significance of our sample for all the modes as shown by Monte Carlo study results shown in Table 3.1.

Prior to the offline reconstruction, data go through the quality checks to ensure that the readouts from all the relevant systems of the detector are present and in good condition. Tracks are reconstructed from hits (Figure 3-1) in the silicon microstrip detector (SVX) and the central outer tracker (COT) introduced in Section 2.2.

3.2 Vertex Fits and General Pre-Selection Cuts

To find a particle which decayed into two or more tracks in the detector, we look for two or more tracks intersecting in one point of three-dimensional space with the pro-

Channel	B_CHARM_LOWPT Gain %
$B^0 \to D^-\pi^+\pi^+\pi^-$	$41\% \pm 1.5\%$
$B_s^0 \to D_s^-(\phi\pi^-)\pi^+\pi^+\pi^-$	$40\% \pm 2\%$
$B_s^0 \to D_s^-(K^{*0}K^-)\pi^+\pi^+\pi^-$	$34\% \pm 4\%$
$B_s^0 \to D_s^-(\pi^+\pi^-\pi^-)\pi^+\pi^+\pi^-$	$34\% \pm 4\%$
$B^0 \to D^-D_s^+(\phi\pi^-)$	$33\% \pm 1\%$
$B^0 \to D^-D_s^+(K^{*0}K^-)$	$31\% \pm 2\%$
$B^0 \to D^-D_s^+(\pi^+\pi^-\pi^-)$	$34\% \pm 2\%$
$B_s^0 \to D_s^-D_s^-(\phi\pi^-)$	$40\% \pm 3\%$
$B_s^0 \to D_s^-D_s^-(K^{*0}K^-)$	$42\% \pm 3\%$
$B_s^0 \to D_s^-D_s^-(\pi^+\pi^-\pi^-)$	$42\% \pm 3\%$

Table 3.1: Gain due to the addition of B_CHARM_LOWPT triggers.

cedure called *vertexing* [34]. Complicated decays involving several secondary vertices may require pointing and mass constraints for the secondary products. To ensure the quality of the vertex fit, we only use the tracks satisfying the following conditions:

- At least 3 SVX r-ϕ hits,
- COT parent track with at least 10 hits in axial layers and 10 hits in stereo layers,
- track $p_T \geq 350$ MeV/c.

We refit the default offline tracks with several additions and corrections:

- Tracks are refitted with addition of L00 hits. This feature requires the additional tuning of the Monte Carlo simulation described in Section 4.1.
- Energy loss correction takes into account the material of the detector missing in the default production reconstruction.
- COT covariance matrix scaling takes care of the residual effects of Coulomb scattering inside the COT detector.

No particle ID is explicitly used in this analysis and every track is assumed to be either a pion or a kaon depending on the specific reconstruction hypothesis. The reconstruction of $B^0 \to D^-D_s^+(\phi\pi^+)$ begins with a $\phi \to K^+K^-$, applying a vertex fit to two tracks with opposite charge. $\phi \to K^+K^-$ candidates are used to reconstruct

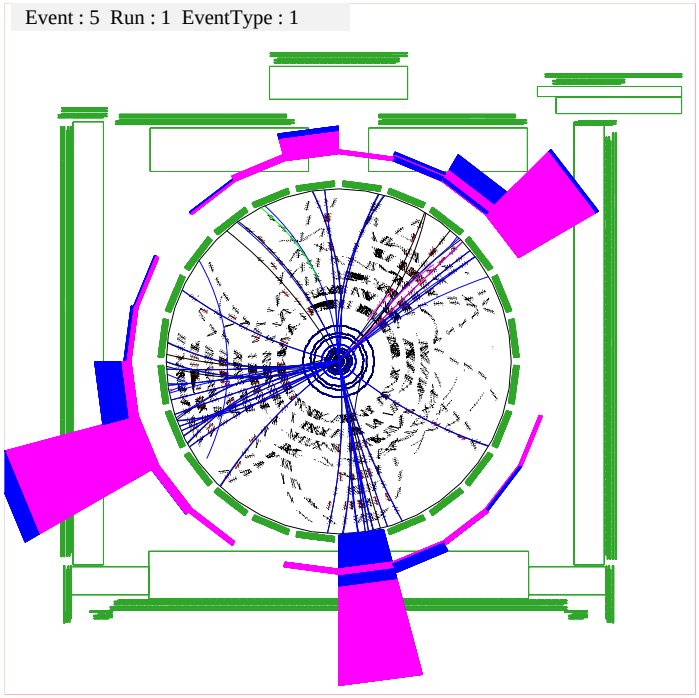

Figure 3-1: Tracks reconstructed from hits in COT and SVX detectors.

$D_s^+ \to \phi\pi^+$ candidates by adding another track and applying a vertex fit to the 3-track vertex. A similar approach is used to reconstruct $D_s^- \to K^{*0}K^-$, $D_s^- \to \pi^+\pi^-\pi^-$, and $D^- \to K^+\pi^-\pi^-$ candidates. Reconstructed D meson candidates are stored in the event collections and used to reconstruct various B meson decay modes. To reconstruct $B^0 \to D^-D_s^+(\phi\pi^+)$ mode, for example, the procedure loops over the $D^- \to K^+\pi^-\pi^-$ and $D_s^- \to \phi\pi^-$ candidate collections, and applies a 6-track vertex fit to the B meson vertex and two D meson secondary vertices using mass constraints for both D mesons. An equivalent procedure is used to reconstruct $B_s^0 \to D_s^-D_s^+$ candidates.

Triple-pion combinations used to reconstruct $B^0 \to D^-\pi^+\pi^+\pi^-$ and $B_s^0 \to D_s^-\pi^+\pi^+\pi^-$ decay modes are formed from all eligible tracks and fitted with a vertex fit to a common origin. Vertex quality requirements are applied on these vertices. To reduce the overwhelming combinatorial background from the rest of the tracks in the event, we require the mass of a triple-pion originating from the B^0 meson in the $B^0 \to D^-\pi^+\pi^+\pi^-$ decay to be smaller than the mass difference of the corresponding B and D mesons $(m(B_{(s)}) - m(D_{(s)}))$. To reconstruct $B^0 \to D^-\pi^+\pi^+\pi^-$ decay mode, the procedure

loops over $D^- \to K^+\pi^-\pi^-$ and $\pi^+\pi^+\pi^-$ collections and applies a 6-track vertex fit to the B meson vertex, which should coincide with the triple-pion vertex, and the D meson secondary vertex using mass constraints for the D meson.

Several selection requirements are applied at intermediate stages of the reconstruction in a sequence, optimized to reduce the computation time and the size of the output. The typical order of the selection requirements is:

- Candidates with the same track content and assignment are removed.
- Candidates with wrong charge combinations are removed. In some cases we store the "*Wrong Charge*" candidates for combinatorial background studies.
- Two on-line trigger tracks are required for B meson candidates. No trigger track requirements for D candidates are applied.
- The raw mass is calculated based on the track momenta and candidates are only accepted within a loose mass window.
- A loose mass window ± 100 MeV/c^2 around world average [1] mass values is applied to D meson candidates. After that, D meson masses are constrained to their world average mass values while fitting the parent B meson candidate.
- A full vertex fit is performed and the resulting χ^2 of the fit in the transverse plane ($\chi^2_{R\phi}$), the fitted mass, and the L_{xy} are used to reject candidates. Selection cuts are only applied at this stage if tighter cuts are applied later in the analysis.

The extra effort is made to reduce self-reflections produced by swapping the candidate tracks with the change of particle assignment (kaon to pion or vice versa), and also swapping the tracks between the vertices of the intermediate decay products. The Monte Carlo study of this effect is discussed in Section 4.1.

3.3 Trigger Confirmation

In this analysis we used data which passed the `B_CHARM` or the `B_CHARM_LOWPT` trigger paths. Each B meson candidate is required to have a *trigger pair* introduced in Section

3. A trigger pair is confirmed for every event and for each B meson candidate in the event. For each event, we confirm the trigger bit information. For each candidate, we perform a SVT matching of the tracks with an matching algorithm [35] based on the `svtsim` [36] package.

To promote a reconstructed offline track to an *on-line trigger track*, we require that the p_T and d_0 of the track comply with $p_T > 2$ GeV/c, and 0.0120 cm $< |d_0| < 0.1$ cm. Then using the known p_T and ϕ_0 of the online trigger tracks, we calculate the χ^2 value of its match to the offline track. We require the candidates from the `B_CHARM` data sample to pass the `B_CHARM` trigger pair confirmation and candidates from the `B_CHARM_LOWPT` data sample to pass the `B_CHARM_LOWPT` trigger pair confirmation.

Chapter 4

Monte Carlo Simulation

Monte Carlo simulations are used to model the systems which are impossible to describe analythically due to unknown or very complicated structure. Monte Carlo statistically reproduces the observed output of the modelled systems, treating its innerworking as a blackbox. In particle physics Monte Carlo simulations are used to reproduce the observed statistical distributions of the elementary particles, and to model the responce of the detectors. Ideally, the output of the good simulations should be indistinguishable from data for the available size of the data sample. In this analysis Monte Carlo simulations are used for several purposes:

- selection cut optimization,
- the construction of templates for signals and reflections,
- analysis efficiency study.

Since we are only interested in reconstructind exclusive signals, we use Monte Carlo simulations producing B mesons without the fragmentation products of the $p\overline{p}$ collisions, a so called *signal Monte Carlo*. There are no selection requirements using the knowledge of the underlying event structure, and there are no systematic uncertainty from the fragmentation tracks. There are several components in the Monte Carlo simulation.

- quark production mechanism

- fragmentation
- b hadron decay
- decay branching fractions

We use the `BGenerator` package [37] to create B mesons. It is based on NLO calculations [38] and the fragmentation is implemented using the Peterson fragmentation function [39]. The `BGenerator` only produces B mesons; no fragmentation products are present. To decay B mesons, we use the `EvtGen` package [40] with the decay tables updated with most recent world averages of branching fractions. The detector geometry and trigger response are simulated with `GEANT` [41] and a software trigger simulation. The output of the Monte Carlo simulations is thoroughly compared with data to make sure that it has the identical run list selection, trigger selection, and the distributions of the reconstructed quantities.

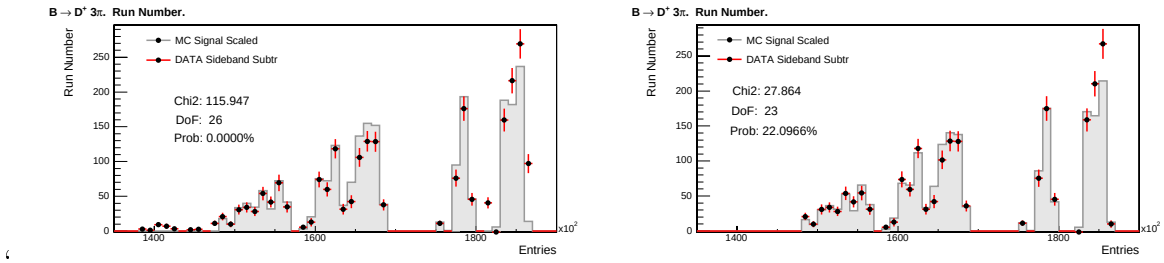

Figure 4-1: Run range comparison for data and Monte Carlo. All data files present (left) and data files removed for runs with missing Monte Carlo simulations (right).

To reflect time dependent changes in the detector conditions and trigger tables, we developed a *realistic* Monte Carlo simulation [42]. The detector conditions do not change within a non-stop data taking period called a *run*. Run-to-run changes may include the parameters of the trigger tables at Level1 and Level2, the silicon detector conditions, and the alignment. The data corresponding to every run could be easily identified in the dataset. We create a Monte Carlo simulation for every run we use in our analysis, with the number of generated events proportional to the run luminosity. Figure 4-1 shows a run-by-run comparison of the number of B meson candidates for data and Monte Carlo simulations. Due to the technical problems realistic Monte Carlo simulations miss a few runs with a total luminosity of about 30pb^{-1} scattered

over three short periods of data taking, easily identifiable on Figure 4-1. We use the data representing these runs in our analysis and discuss the systematic uncertainty due to the effect in Section 8.1.

We treat Monte Carlo simulations following the procedures described in Section 3.3 for data. To confirm the trigger selection in Monte Carlo simulations, we use the trigger confirmation procedure identical to the one, we apply to events and reconstructed B meson candidates from data. To take run dependent trigger prescale into account for Monte Carlo simulations, we extract the number of data events before and after the prescale from the database and find an average (*effective*) prescale value for each trigger path for each run.

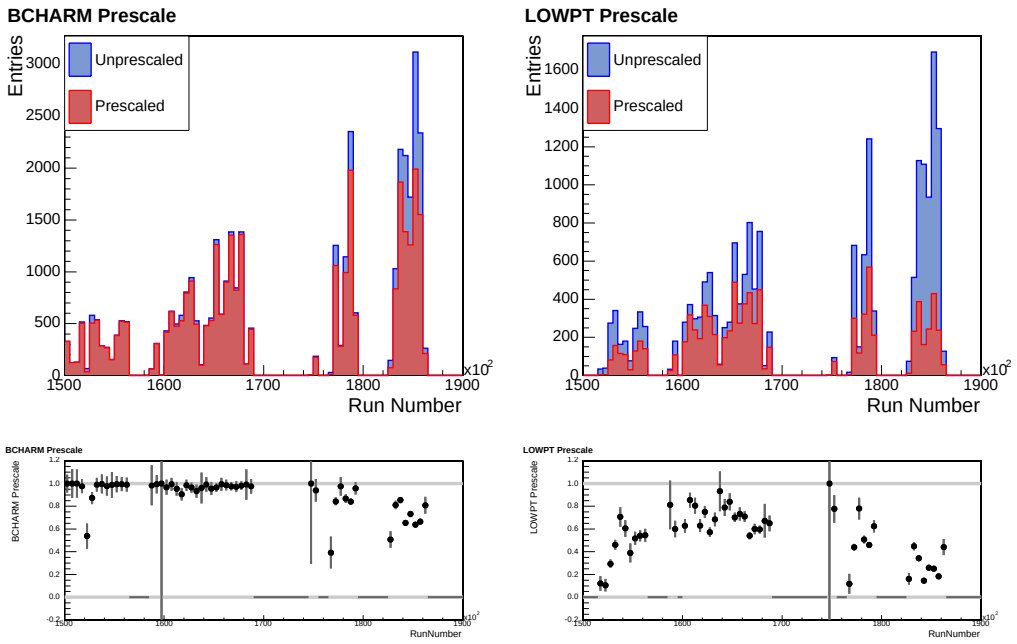

Figure 4-2: The number of prescaled and unprescaled events are shown versus the run number. `B_CHARM` is shown on the left and `B_CHARM_LOWPT` is shown on the right.

The prescale is implemented for the Monte Carlo simulation by adding a filter which accepts the simulated event with the probability proportional to the effective prescale. The run-dependent prescale profiles are shown on Figure 4-2. Treating the prescale run-by-run achieves a good agreement for the relative `B_CHARM` and `B_CHARM_LOWPT` yields between Monte Carlo simulations and data (Table 4.1).

	Data	Monte Carlo
B_CHARM	2169 ± 64	11546 ± 124
B_CHARM and B_CHARM_LOWPT	3079 ± 79	16299 ± 139
Gain %	$42.0 \pm 1.5\%$	$41.2 \pm 0.6\%$

Table 4.1: The gain due to the B_CHARM_LOWPT trigger.

4.1 Data and Monte Carlo Comparison

To make sure that Monte Carlo describes our data well we perform a detailed comparison of the Monte Carlo simulation with data using our largest signal sample: $B^0 \to D^-\pi^+\pi^+\pi^-$. To eliminate the contribution of the background under the signal peak we use a sideband subtraction procedure (Figure 4-3). It relies on the hypothesis that the combinatorial background in the sideband is identical to the combinatorial background under the signal. Knowing the ratio of the signal and the background in the signal window, the properties of the signal could be expracted if we statisticaly subtract the right background proportion using a clean background sample from the sideband. For sideband subtraction, we use the mass interval centered at the fitted mass of the B meson and including 95.45% of the $B^0 \to D^-\pi^+\pi^+\pi^-$ signal, and the right sideband with clean combinatorial background, including the region between 5 and 15 standard deviations from the signal, as shown on Figure 4-3.

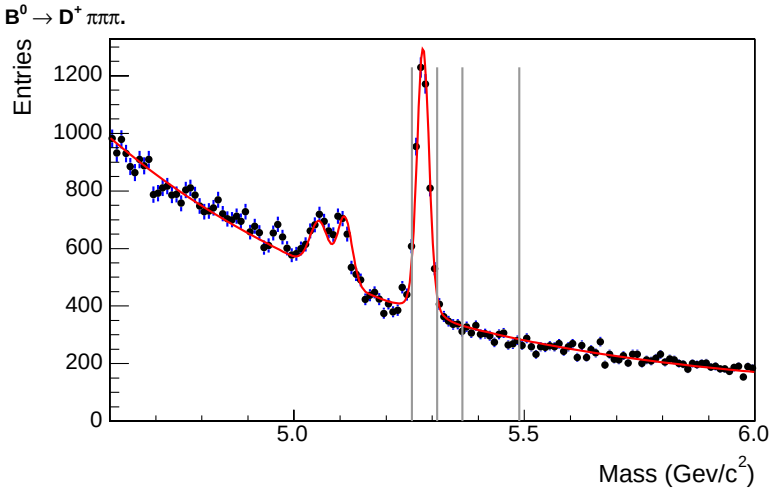

Figure 4-3: Illustration of the signal and the sideband regions for $B^0 \to D^-\pi^+\pi^+\pi^-$ mode.

Before making the comparison, we prepare our data and Monte Carlo simulations. We divide Monte Carlo and data sets into B_CHARM and B_CHARM_LOWPT samples, confirming trigger bits for each event and a trigger pair for each candidate. We apply a run-by-run prescale procedure to Monte Carlo simulations separately for B_CHARM and B_CHARM_LOWPT samples. After prescale is applied we combine the B_CHARM and B_CHARM_LOWPT samples. If there are duplicate events then the event which passed the B_CHARM trigger is taken. To correct hits from L00 for efficiency and resolution we apply *hit smearing* module [27] to Monte Carlo simulations which does the following

- L0 and L00 hits in the Monte Carlo simulation are smeared to match the resolution measured in data.
- A proportion of L00 hits is randomly dropped to correct for over-efficiency of the Monte Carlo simulation.
- All event tracks are refitted with the new L0 and L00 hits.

We start by comparing the track parameters of data and Monte Carlo. We combine histograms for all 6 tracks of the signal decay to improve the statistical power of the study. The transverse momentum p_T and the pseudo-rapidity η distributions are shown on Figure B-2. A zoom into the low momentum region is shown on Figure B-3. A good match of the radial angle of the track (Figure B-3), the impact parameter of the track, and the number of track silicon hits (Figure B-4) insures that tracking and trigger algorithm produce the same results for data and Monte Carlo simulations.

To make comparisons for variables used as a selection criteria, we loosen up the relevant selection cuts to be able to compare the distributions below and above the cut value (Figures B-5, B-6, and B-8). The default value of the selection criteria is marked with a vertical gray line in these plots.

Reproducing the 3π mass distribution in the $B^0 \to D^-\pi^+\pi^+\pi^-$ decay with Monte Carlo simulations proved to be very challenging. The tuned decay table (Table A.9), based on our study discussed in Section 8.3 and a recent BaBar paper [43], does not reproduce the low mass turn-on as shown on Figure 4-4. The spike due to the $D_s^- \to \pi^+\pi^-\pi^-$ mode, clearly visible in data, agrees with the expected amount of

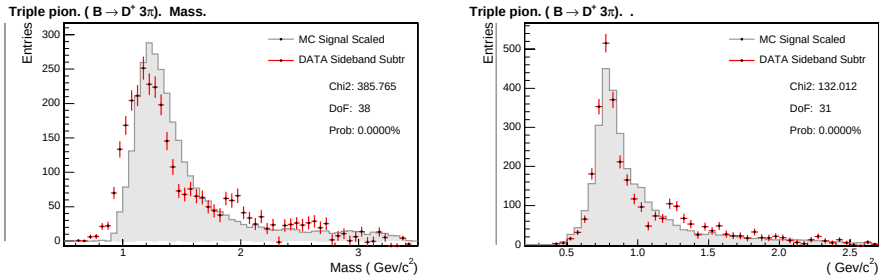

Figure 4-4: Compare $B^0 \to D^-\pi^+\pi^+\pi^-$ Monte Carlo simulations and sideband subtracted data. Mass of the 3π on the left and mass of subset of 2π on the right.

the contribution from $B^0 \to D^- D_s^+(\pi^+\pi^+\pi^-)$ mode estimated from the its measured yield.

We study the structure of the a_1 resonance $a_1^+ \to \rho(\pi^+\pi^-)\pi^+$ by looking at the mass distribution of a 2-pion subset. Out of two possible pion pairs with a total charge zero, we take the pair with the higher mass (Figure 4-4). The distribution shows a ρ^0 meson resonance at 770 MeV/c^2. The small resonance near 1.3 GeV/c^2 could correspond to the $f_2(1270)$ meson. Figure B-9 shows the transverse momentum of the 3π system and its opening angle with respect The study of the systematic uncertainty related to 3π resonant structure is discussed in Section 8.3.

A large fraction of events contain more than one candidate for the B meson decay modes with 6 particles in the final state due to large number of possible track permutations. There are two major sources of multiple candidates. We call them *duplicates* and *self-reflections*.

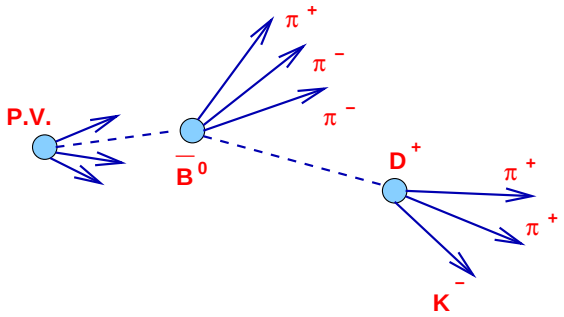

Figure 4-5: Picture representation of $B^0 \to D^-\pi^+\pi^+\pi^-$ decay.

- A *duplicate* is the candidate with the track from the combinatorial background. The decays with many tracks in the final state are particularly vulnerable to this effect due to the high multiplicity of low momentum tracks used for reconstruction. Duplicate candidates have the mass distribution of the combinatorial background. The effect reduces the overall significance of the signal but does not bias the yield measurement.

- A *self-reflection* is the candidate with its tracks swapped. For example, a direct pion from $B^0 \to D^-\pi^+\pi^+\pi^-$ decay could be swapped with one of the pions from D^- decay (Figure 4-5). Self-reflections could become a problem since they often amplify the signal because of the very similar mass distribution.

Channel	No self-refl.	With self-refl.	Change %
$B^0 \to D^-\pi^+\pi^+\pi^-$ (Data)	3316 ± 76	3371 ± 78	$1.7\% \pm 3.0\%$
$B^0 \to D^-\pi^+\pi^+\pi^-$ (MC)	14839 ± 122	15028 ± 123	$1.3\% \pm 1.0\%$
$B_s^0 \to D_s^-(\phi\pi^-)\pi^+\pi^+\pi^-$ (MC)	12061 ± 107	12222 ± 108	$1.3\% \pm 1.0\%$
$B_s^0 \to D_s^-(K^{*0}K^-)\pi^+\pi^+\pi^-$ (MC)	2281 ± 47	2300 ± 47	$0.8\% \pm 2.0\%$
$B_s^0 \to D_s^-(\pi^+\pi^-\pi^-)\pi^+\pi^+\pi^-$ (MC)	1279 ± 35	1279 ± 35	$0.0\% \pm 3.0\%$

Table 4.2: The rate of self-reflections.

In this analysis we only correct for self-reflections and leave all the duplicates in our sample. Duplicates do not affect efficiency and only add to the combinatorial background. The study shows (Table 4.2) that data and Monte Carlo simulations contain the same fraction of self-reflections for a statistically significant $B^0 \to D^-\pi^+\pi^+\pi^-$ decay mode and a negligible fraction for $B_s^0 \to D_s^-\pi^+\pi^+\pi^-$ decay modes. Double-charm B meson decays are not affected by self-reflections due to the mass constraints applied to both D mesons during the fit. The effect is taken into account by searching for the candidates with the same track content. If a self-reflection is found, we keep the B candidate with the higher transverse momentum.

4.2 Analysis Selection Cuts

One of the major challenges of the branching fraction measurement at hadroninc machine is the huge combinatorial background. CDF trigger system does a good job picking interesting events considerably reducing the background level (Section 2.4). During the offline data processing we use the selection cuts applied to the reconstructed candidates to further reduce the background. We choose the selection cuts which have non-trivial separation power between the signal and the background and remove unique backgrounds. Since we use only signal Monte Carlo simulations, we cannot estimate the efficiency of the selection cuts which would use the structure of the underlying event, for example, any kind of isolation cuts.

The final values of the selection cuts are chosen with the help of the optimization procedure. In short: we apply a set of selection cuts, fit the combinatorial background in the data, extrapolate it under the signal, calculate the expected significance, and repeat the sequence with another set of selection cuts. For optimization, we only use background in the sideband above the signal peak to avoid bias from the misreconstructed decays in the left sideband of the signal. Background is fitted with the sum of a constant and an exponential function. To integrate the signals we use the width of the mass interval centered around the fitted B meson mass, and extended symmetrically to include 95.45% of the B meson signal. We define the width of the region equivalent of the two standard deviations of *effective signal width*.

The optimization process is iterative. Each cut is varied within reasonable limits while the others are fixed to default values. In the beginning, the procedure applies default cuts to the reconstructed Monte Carlo signal and scales the Monte Carlo yield to the expected number of signal B meson candidates. The step by step algorithm is described below:

1. Monte Carlo signal is fitted with the default cuts and the yield is scaled to the expected signal yield from data,
2. We vary one selection cut while keeping the others at default values, and apply the new set of cuts to data and Monte Carlo simulations

3. Monte Carlo signal is fitted to get the effective signal width,
4. Data mass distribution is fitted with the background model omitting the blinded data region with a center at B meson mass and the width equal to ± 3.0 standard deviations of effective signal width,
5. the background model is extrapolated into the blinded signal region and data background is integrated in signal region ± 2.0 standard deviation wide,
6. scaled Monte Carlo signal is integrated in the same signal region and the significance of the signal with a given set of cuts is calculated,
7. the next cut value is chosen,
8. if all the values for the current selection cut variable are tested, the cut is set to the default value and the next cut is varied,
9. if all the selection cuts were varied, the results are printed.

This procedure displays a dynamic fit for the visual quality check (Figure B-11). In the end of the optimization for every optimized cut, we get the Monte Carlo efficiency and the signal significance as functions of the cut value. As an example, Figure B-11 shows the optimization results for B meson vertex fit χ^2 selection cut, optimized for $B^0 \to D^-\pi^+\pi^+\pi^-$ mode. The final value of the selection cut is chosen to maximize the significance of the signal. If the significance curve has a plateau, we choose the cut value corresponding to the best efficiency. The procedure takes several iterations to converge to the optimal set of cuts. To optimize the B^0 selection cuts we use a [5.2, 6.0] GeV/c^2 mass window, and to optimize B_s^0 selection cuts we use the [5.3, 6.5] GeV/c^2 mass window.

Modes with high statistics are optimized with respect to Gaussian significance using the number of signal and background events in the signal region

$$S(\mathcal{G}) = \frac{N_{\text{signal}}}{\sqrt{(N_{\text{signal}} + N_{\text{background}})}}. \tag{4.1}$$

In this case in the beginning of the optimization the Monte Carlo signal is scaled to the expected number of events taken from the data fit with the default selection

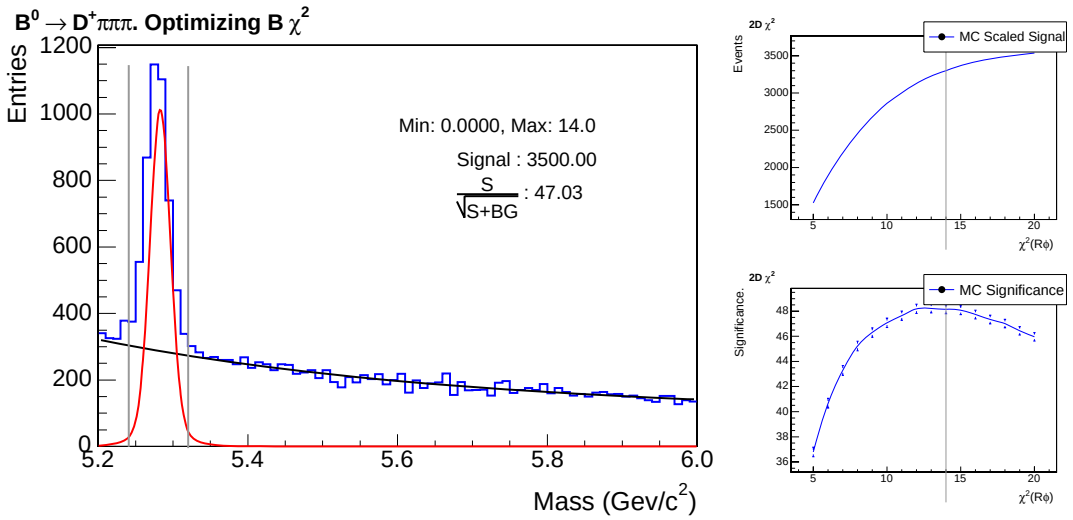

Figure 4-6: A snapshot of the optimization process for χ^2 of the B^0 for $B^0 \to D^-\pi^+\pi^+\pi^-$ mode (left). Grey lines show the region used to calculate the signal significance. The output of the optimization procedure for the same selection cut is on the right with efficiency curve on top and significance curve on the bottom. The gray line shows the default cut value.

cuts applied. The number of expected events only affects the absolute value of the significance in this case. It does not affect the position of the maximum point on the significance curve and does not bias the optimization output. The full set of the optimization plots for $B^0 \to D^-\pi^+\pi^+\pi^-$, $B_s^0 \to D_s^-\pi^+\pi^+\pi^-$, and $B^0 \to D^-D_s^+$ modes is shown on Figures B-12 - B-25.

For $B_s^0 \to D_s^-D_s^+$ modes, we use a parametrized significance for low statistics modes [44]. The prescription effectively adds a constant term to the background to avoid unrealistically high values of significance for an empty background. Optimization plots for the $B_s^0 \to D_s^-D_s^+$ mode are shown on Figures B-26 - B-31.

The $B_s^0 \to D_s^-(K^{*0}K^-)\pi^+\pi^+\pi^-$ mode has a strong reflection from the misreconstructed $B^0 \to D^-\pi^+\pi^+\pi^-$ mode under the signal. The normalization and the shape of this reflection depend on the selection cuts and cannot be fixed to a constant value. We apply a $D^- \to K^+\pi^-\pi^-$ veto, discussed in Section 8.4, which removes more than 97% of the reflection according to Monte Carlo studies. As a first approximation of the selection cuts for $B_s^0 \to D_s^-(K^{*0}K^-)\pi^+\pi^+\pi^-$ mode, we use the average of the corresponding selection cuts used for $B_s^0 \to D_s^-(\phi\pi^-)\pi^+\pi^+\pi^-$

and $B_s^0 \to D_s^-(\pi^+\pi^-\pi^-)\pi^+\pi^+\pi^-$ modes. A similar approach is used for $B_s^0 \to D_s^-(\phi\pi^-)D_s^+(K^{*0}K^+)$ mode, which has a strong $B^0 \to D^-D_s^+(\phi\pi^+)$ reflection under the signal.

The cut optimization for $B^0 \to D^-D_s^+$ modes includes five correlated cuts based on the L_{xy} variable. To show that all five are necessary, we optimize the selection cuts from scratch for $B^0 \to D^-D_s^+$ modes, omitting the requirements on $L_{xy}/\sigma(L_{xy})$ of D mesons. As a result, the remaining selection cuts become tighter (Table 4.3).

$B^0 \to D_s^+D^-$	$D_s^+ \to \phi\pi^+$	$D_s^+ \to K^{*0}K^+$	$D_s^+ \to \pi^+\pi^+\pi^-$
B^0 $L_{xy}/\sigma(L_{xy})$	> 6	> 6	> 4
B^0 d_0	< 0.008 cm	< 0.008 cm	< 0.0075 cm
B^0 $\chi^2_{R\phi}$	< 20	< 17	< 13
D_s^+ $L_{xy}/\sigma(L_{xy})$	> 5	> 5	> 10
D_s^+ $L_{xy}^{\leftarrow B}$	> -0.02 cm	> 0.0 cm	> -0.02 cm
D^- $L_{xy}/\sigma(L_{xy})$	> 6	> 13	> 12
D^- $L_{xy}^{\leftarrow B}$	> -0.02 cm	> 0.0 cm	> -0.02 cm
Track Min p_T	> 0.35 GeV/c	> 0.35 GeV/c	> 0.35 GeV/c
No $D_{(s)}$ $L_{xy}/\sigma(L_{xy})$ cuts			
B^0 $\frac{L_{xy}}{\sigma(L_{xy})}$	> 6	> 6	> 7
B^0 d_0	< 0.01 cm	< 0.007 cm	< 0.006 cm
B^0 $\chi^2_{r\phi}$	< 18	< 14	< 10
D_s^+ $L_{xy}^{\leftarrow B}$	> -0.01 cm	> 0.01 cm	> 0.01 cm
D^- $L_{xy}^{\leftarrow B}$	> -0.01 cm	> 0.01 cm	> 0.01 cm
Track Min p_T	> 0.35GeV/c	> 0.4GeV/c	> 0.4GeV/c

Table 4.3: Optimization results with D meson $L_{xy}/\sigma(L_{xy})$cuts and without them.

The decrease in the yield for $B^0 \to D^-D_s^+(\phi\pi^+)$ mode (Table 4.2) is negligible due to the very selective ϕ mass window requirement. The statistically significant yield drop for the other two modes shows the necessity of using all five L_{xy} based selection cuts. We use the reduced list of selection cuts for $B_s^0 \to D_s^-D_s^+$ modes since all of them have at least one ϕ mass window requirement.

The optimized selection cuts for all the modes are summarized in Tables A.11 - A.14. `B_CHARM` and `B_CHARM_LOWPT` samples have the same analysis cuts, but the implicit trigger cuts are different.

$B^0 \to D^- D_s^+$	$\phi\pi^+$	$K^{*0}K^+$	$\pi^+\pi^+\pi^-$
With $L_{xy}/\sigma(L_{xy})$cuts	183 ± 15	128 ± 13	84 ± 13
Without $L_{xy}/\sigma(L_{xy})$cuts	185 ± 16	103 ± 12	55 ± 10

Table 4.4: Data and Monte Carlo yields without D^- meson $L_{xy}/\sigma(L_{xy})$selection cut.

The background events used in the optimization fit are also used to evaluate the background in the signal window when calculating the significance of the signal. It creates conditions for the background bias which is significant for the $B_s^0 \to D_s^- D_s^+$ modes due to low statistics. This topic is discussed in details in Sections 7 and 8.

4.3 Efficiencies Extracted from Monte Carlo

To measure the efficiency of our analysis selection, we generate signal Monte Carlo for every reconstructed mode and apply detector simulation, trigger response simulation, run-by-run prescale, L00 hit smearing, reconstruction, trigger confirmation, and analysis cuts the way it is described in the previous sections.

The number of generated signal Monte Carlo events, the fitted signal yield after reconstruction, and the measured efficiency for all the modes are listed in Table 4.5. The decay table used for the Monte Carlo simulation of $B^0 \to D^-\pi^+\pi^+\pi^-$ mode is quoted in Table A.1, and discussed in detail in Section 8.3. The decay table for $B_s^0 \to D_s^-(\pi^+\pi^-\pi^-)\pi^+\pi^+\pi^-$ modes with three different D_s^- channels is quoted in Table A.4). The resonant composition of the $D_s^- \to \pi^+\pi^-\pi^-$ mode is discussed in details in Section 8.3. The decay tables for $B^0 \to D^- D_s^+$ and $B^0 \to D^{(*)-} D_s^{(*)+}$ modes with three different D_s^- decay channels are quoted in Table A.6 and Table A.7. The decay table for $B_s^0 \to D_s^- D_s^+$ mode with three different D_s^- decay channels is quoted in Table A.8. The relative branching fractions of three D_s^- decay modes are scaled using the world average values [1] to study the cross talks between different channels discussed in Section 5.2.2.

To extract the reconstructed yield, Monte Carlo mass distributions are fitted with the signal templates described in Section 5.3, and the mass centered at the fitted B

Mode	Gen. ($\times 10^6$)	Yield MC	Eff. ($\times 10^{-3}$)
$B^0 \to D^- \pi^+ \pi^+ \pi^-$	60.0	14839 ± 122	0.247 ± 0.002
$B_s^0 \to D_s^- (\phi\pi^-) \pi^+ \pi^+ \pi^-$	60.0	12061 ± 107	0.201 ± 0.003
$B_s^0 \to D_s^- (K^{*0} K^-) \pi^+ \pi^+ \pi^-$	26.2	2281 ± 47	0.087 ± 0.002
$B_s^0 \to D_s^- (\pi^+ \pi^- \pi^-) \pi^+ \pi^+ \pi^-$	13.1	1279 ± 35	0.098 ± 0.003
$B^0 \to D^- \pi^+ \pi^+ \pi^-$	60.0	15831 ± 132	0.264 ± 0.002
$\Lambda_b \to \Lambda_c 3\pi$	20.0	365 ± 19	0.018 ± 0.001
$B^0 \to D^- K^+ \pi^- \pi^-$	10.4	2839 ± 53	0.273 ± 0.005
$B^0 \to D^- D_s^+ (\phi\pi^+)$	16.49	6617 ± 80	0.401 ± 0.005
$B^0 \to D^- D_s^+ (K^{*0} K^+)$	20.89	5185 ± 70	0.248 ± 0.003
$B^0 \to D^- D_s^+ (\pi^+ \pi^+ \pi^-)$	9.98	3563 ± 58	0.357 ± 0.006
$B^0 \to D^- D_s^+ (\phi\pi^+)$	2.765	1191 ± 34	0.424 ± 0.011
$B^0 \to D^- D_s^{*+}$	4.35	1724 ± 42	0.396 ± 0.010
$B^0 \to D^{*-} D_s$	4.66	526 ± 23	0.113 ± 0.005
$B^0 \to D^{*-} D_s^{*+}$	8.25	938 ± 31	0.114 ± 0.003
$B_s^0 \to D_s^- (\phi\pi^-) D_s^+ (\phi\pi^+)$	4.53	1591 ± 38	0.351 ± 0.008
$B_s^0 \to D_s^- (\phi\pi^-) D_s^+ (K^{*0} K^+)$	11.48	1508 ± 38	0.131 ± 0.003
$B_s^0 \to D_s^- (\phi\pi^-) D_s^+ (\pi^+ \pi^+ \pi^-)$	5.49	1233 ± 35	0.225 ± 0.006

Table 4.5: Efficiencies extracted from Monte Carlo simulations.

meson mass and containing 95.45% of the signal is integrated. The signal template parameters are saved and used later to fit the data.

Chapter 5

Signal and Background Templates

The fitting model affects the quality of the fit and may significantly change the estimated signal. Earlier analysis [20] shows that the fitting model gives rise to the largest systematic uncertainty. The fitting model in our analysis consists of three major terms:

- **Signal** - a sharp resonant peak at the B meson mass with a width defined by the detector and the reconstruction resolution.
- **Physics background** - a background with a lot of features originated from the incomplete or incorrect reconstruction of the modes similar to signal mode in mass, decay content, and topology.
- **Combinatorial background** - a smooth featureless background formed by the accidental combinations of the fragmentation tracks.

The signal terms and the physics background terms of our fitting function are constructed out of several *templates* - the functions with fixed shape and floating or fixed normalization. Identifying all the physics backgrounds and incorporating them into the fitting functions makes this analysis very challenging. A few partially reconstructed decay modes contribute significantly to the fit ranges affecting the signal yields. For these modes, dedicated Monte Carlo samples are generated to create fitting templates. The rest of the physics backgrounds are studied with the help of *"semi-generic"* Monte Carlo simulations, which are neither signal simulations nor

fully generic simulations. For example, to study the physics backgrounds for the $B^0 \to D^-(K^+\pi^-\pi^-)\pi^+\pi^+\pi^-$ mode, we use the $B \to D^-(K^+\pi^-\pi^-)X$ semi-generic Monte Carlo simulation. Here, B stands for the combination of B_d, B_u, B_s, and Λ_b hadrons, weighted by production ratios. All decays are allowed according to the generic decay table with exception of the D^- meson, which is forced to decay to $K^+\pi^-\pi^-$ channel.

5.1 Signal Templates

The reconstructed signals have a Gaussian shape with the width defined by the detector resolution. $B^0 \to D^-\pi^+\pi^+\pi^-$ signal is fitted with a triple Gaussian while less populated $B_s^0 \to D_s^-\pi^+\pi^+\pi^-$, $B^0 \to D^-D_s^+$, and $B_s^0 \to D_s^-D_s^+$ signals are fitted with a double Gaussian

$$f_{Sig} = f_1\mathcal{G}(m|\mu,\sigma_1) + (1-f_1)\mathcal{G}(m|\mu,\sigma_2). \tag{5.1}$$

Here f_1 is a normalization fraction of the smaller Gaussian, μ is the mean, σ_1 and σ_2 are the widths. The Gaussian terms within one signal template are constrained to have a common mean. The ratios of the normalizations and widths of the individual Gaussian terms are determined using Monte Carlo simulations. The signal yield for both, Monte Carlo simulations and data, is integrated using the *effective width* - the mass interval, centered at the fitted mass of the B meson, and containing 95.45% of the signal.

By using the $B^0 \to D^-\pi^+\pi^+\pi^-$ mode with high statistics, we measure the difference of the signal width in data and in Monte Carlo simulation. Following the results of the fit, summarized in Table 5.1, the widths of the signal Gaussian terms for the $B_{(s)} \to D_{(s)}\pi^+\pi^+\pi^-$ modes are corrected by $17 \pm 3\%$ (Table 5.3) and the mass terms of all the corresponding templates are shifted by -4.85 MeV/c^2.

The corresponding study for $B^0 \to D^-D_s^+$ mode shows that the double-charm signal does not exhibit a mass shift because the masses of both D mesons are constrained

Parameter	Value Data	Error Data	Value MC	Error MC	Diff
Signal	3.443e+01	7.993e-01	1.553e+01	1.364e-01	NA
Mass0	5.278e+00	3.857e-04	5.283e+00	2.915e-04	-4.8 ± 0.5 MeV/c^2
Width0	1.062e-02	3.818e-04	9.084e-03	8.599e-04	$17\% \pm 3\%$
Frac1	7.161e-01	fixed	7.185e-01	8.390e-02	fixed
Mass1	5.278e+00	fixed	5.283e+00	fixed	fixed
Width1	1.633e-02	fixed	1.481e-02	6.787e-04	fixed
Frac2	6.775e-02	fixed	6.788e-02	9.775e-03	fixed
Mass2	5.278e+00	fixed	5.283e+00	fixed	fixed
Width2	4.259e-02	fixed	4.102e-02	8.733e-03	fixed

Table 5.1: The comparison of the signal fitted parameters for data and Monte Carlo simulations for $B^0 \to D^-\pi^+\pi^+\pi^-$mode.

Parameter	Value Data	Error Data	Value MC	Error MC	Diff
Signal	9.490e-01	8.050e-02	6.919e+00	8.318e-02	NA
Mass	5.282e+00	9.046e-04	5.281e+00	1.045e-04	1.27 ± 0.9 MeV/c^2
Width	9.078e-03	8.163e-04	7.830e-03	1.307e-04	$16 \pm 2\%$
Frac	6.413e-02	fixed	6.413e-02	1.638e-02	fixed
Mass1	5.282e+00	fixed	5.281e+00	fixed	fixed
Width1	2.124e-02	fixed	1.831e-02	1.407e-03	fixed

Table 5.2: The comparison of the signal fitted parameters for data and Monte Carlo simulations for $B^0 \to D^-D_s^+$ mode.

to their world average values [1] during the fit. The width of the $B^0 \to D^-D_s^+$ signal in data is $16 \pm 2\%$ wider then the width of the reconstructed Monte Carlo signal. The widths of the signal Gaussian terms for $B^0 \to D^-D_s^+$ and $B_s^0 \to D_s^-D_s^+$ modes are corrected by this amount (Table 5.3).

Only normalizations and masses of the signal templates are left floating for $B_s^0 \to D_s^-\pi^+\pi^+\pi^-$ and $B^0 \to D^-D_s^+$ modes to avoid the fluctuation of the fit due to the low statistics. For $B_s^0 \to D_s^-D_s^+$ modes, only the normalization of the signal template is left floating, and the mass is fixed to the world average value [1]. The systematic uncertainty due to the parameters being fixed is estimated in Section 8.5.1.

Mode	Width [MeV/c^2]	Correction [%]
$B^0 \to D^-\pi^+\pi^+\pi^-$	17.1	No[1]
$B_s^0 \to D_s^-(\phi\pi^-)\pi^+\pi^+\pi^-$	15.7	17 ± 3
$B_s^0 \to D_s^-(K^{*0}K^-)\pi^+\pi^+\pi^-$	16.4	17 ± 3
$B_s^0 \to D_s^-(\pi^+\pi^-\pi^-)\pi^+\pi^+\pi^-$	17.1	17 ± 3
$B^0 \to D^-D_s^+(\phi\pi^+)$	8.8	16 ± 2
$B^0 \to D^-D_s^+(K^{*0}K^+)$	9.5	16 ± 2
$B^0 \to D^-D_s^+(\pi^+\pi^+\pi^-)$	8.9	16 ± 2
$B_s^0 \to D_s^-(\phi\pi^-)D_s^+(\phi\pi^+)$	7.5	16 ± 2
$B_s^0 \to D_s^-(\phi\pi^-)D_s^+(K^{*0}K^+)$	7.5	16 ± 2
$B_s^0 \to D_s^-(\phi\pi^-)D_s^+(\pi^+\pi^+\pi^-)$	7.5	16 ± 2

Table 5.3: The effective widths of the Monte Carlo signals and the width corrections applied for the signal templates with fixed width. [1]The width of the $B^0 \to D^-\pi^+\pi^+\pi^-$ mode is floating when fitting data.

5.2 Physics Background Templates

Physics background includes decay modes similar to the signal with the decay products being lost or misreconstructed. Misreconstucted modes are sometimes also called *reflections*. Reflections may occur shifted from their original mass and may have various shapes defined by the detector resolution and kinematics of the reconstruction. Several reflections have a significant contribution to the mass region used to fit the signals.

5.2.1 Physics Background Templates for $B_{(s)} \to D_{(s)}\pi^+\pi^+\pi^-$

Three different sets of templates are created for $B_s^0 \to D_s^-\pi^+\pi^+\pi^-$ modes with three D_s^- decay channels. Several templates are There are several reflections which are common for all the 3-pion modes

- Cabibbo suppressed B meson decay modes with a kaon reconstructed as a pion,
- $B_{(s)} \to D_{(s)}^{*-}\pi^+\pi^+\pi^-$ modes with a non-reconstructed π_0 from a $D_{(s)}^{*-} \to D_{(s)}^-\pi^0$ decay,
- $\Lambda_b^0 \to \Lambda_c^+\pi^+\pi^-\pi^-, \Lambda_c^+ \to pK^-\pi^+$ decay mode with a proton reconstructed as a pion,

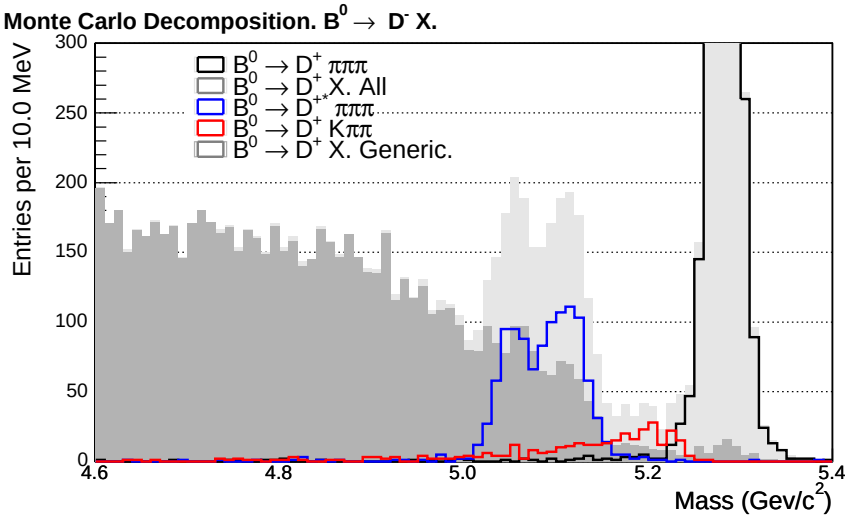

Figure 5-1: The decomposition of the semi-generic $B^0 \to D^-(K^+\pi^-\pi^-)X$ Monte Carlo simulation into $B^0 \to D^-\pi^+\pi^+\pi^-$ signal, $B^0 \to D^-(K^+\pi^-\pi^-)K^-\pi^+\pi^+$ Cabibbo suppressed contribution, $B^0 \to D^{*-}\pi^+\pi^+\pi^-$ reflection, and generic background.

- $B_s^0 \to D_s^-(K^{*0}K^-)\pi^+\pi^+\pi^-$ decay mode with a kaon reconstructed as a pion.

For the $B_s^0 \to D_s^-(K^{*0}K^-)\pi^+\pi^+\pi^-$ decay mode more reflections are relevant and require additional studies:

- $B^0 \to D^-\pi^+\pi^+\pi^-$ mode with a pion reconstructed as a kaons,
- reflection from semi-generic $B^0 \to D^-(K^+\pi^-\pi^-)X$ modes,
- reflection from semi-generic $B^+ \to \overline{D^0}(K^-\pi^+)X$ modes.

For some of the most significant physics backgrounds we generate dedicated Monte Carlo samples. The rest of the backgrounds are studied using the $B^0 \to D^-X$ semi-generic Monte Carlo simulations, where D^- is forced to decay to $K^+\pi^-\pi^-$ and also three independent semi-generic simulations for $B_s^0 \to D_s^-X$, where D_s^- is forced to decay to $\phi\pi^-$, $K^{*0}K^-$, and $\pi^+\pi^-\pi^-$ respectively. Figure B-32 shows the decomposition of the semi-generic $B^0 \to D^-(K^+\pi^-\pi^-)X$ simulation into statistically significant parts. Figures B-37, B-38, and B-39 show similar decompositions for $D_s^- \to \phi\pi^-$, $D_s^- \to K^{*0}K^-$, and $D_s^- \to \pi^+\pi^-\pi^-$ semi-generic simulations, respectively. Below, all the reflections and the templates constructed for them are discussed in detail.

Analysis [20] used the templates for Cabibbo suppressed $B^0 \to D^- K^+$ mode in $B^0 \to D^- \pi^+$ reconstruction. We expect to see the Cabibbo suppressed modes in the reconstruction of $B^0_{(s)} \to D^-_{(s)} \pi^+ \pi^+ \pi^-$ modes, but the present knowledge about the resonant structure of the Cabibbo suppressed decays for these modes is very limited. To create the Monte Carlo decay table for $B^0_{(s)} \to D^-_{(s)} \pi^+ \pi^+ \pi^-$ Cabibbo suppressed modes, we substitute one of the d quarks in the 3π subresonance part of $B^0_{(s)} \to D^-_{(s)} \pi^+ \pi^+ \pi^-$ signal mode with an s quark. This substitution dictates $K^+ \pi^+ \pi^-$, ρK^+, and K_1^+ decay modes instead of $\pi^+ \pi^+ \pi^-$, $\rho \pi^+$,and a_1^+, correspondingly (Table A.2).

The shape of the reconstructed mass distribution does not significantly differ between the three Cabibbo suppressed components. The templates for the Cabibbo suppressed B^0 meson decays are shown on Figure B-36 and for B_s^0 meson on Figures B-40 - B-42. Templates are fitted with a Breit-Wigner distribution smeared with a Gaussian and multiplied by a plateau consisting of two Error functions

$$f_{Cab} = (\mathcal{G}(m|\mu_1\sigma_1) \otimes \mathcal{B}(m|\mu_1\Gamma)) \cdot \mathrm{erf}(m|\mu_2\sigma_2) \cdot \mathrm{erf}(m|\mu_3\sigma_3). \tag{5.2}$$

Here μ_1, σ_1 are the mass and the width of the signal Gaussian, Γ is the width of the Breit-Wigner function, μ_2, μ_3, σ_2, and $\sigma_3$are the masses and the widths of the Error function turn-ons.

To calculate the relative contribution of the Cabibbo suppressed mode to the signal, we use the current measurement of $\mathcal{B}(B^0 \to D^- \pi^+)$ and $\mathcal{B}(B^0 \to D^- K^+)$ [1] quoted in Table 5.4 and assume that

$$\frac{\mathcal{B}(B^0 \to D^- K^+)}{\mathcal{B}(B^0 \to D^- \pi^+)} = \frac{\mathcal{B}(B^0_{(s)} \to D^-_{(s)} K^+ \pi^+ \pi^-)}{\mathcal{B}(B^0_{(s)} \to D^-_{(s)} \pi^+ \pi^+ \pi^-)}. \tag{5.3}$$

Knowing the ratio of the reconstruction efficiencies for the signal and for the Cabibbo suppressed mode (Table 4.5), we may estimate that the normalization of the Cabibbo template is about $(6.9 \pm 2)\%$ of the signal yield. The mass and shape of the template indicates that most of its contribution lies away from the B meson signal window. We use this estimate to fix the normalization of the templates of Cabibbo suppressed modes when fitting $B^0_{(s)} \to D^-_{(s)} \pi^+ \pi^+ \pi^-$ modes.

D^- Decays	Branching
$\Gamma(K^+\pi^-\pi^-)/\Gamma_{total}$	0.092 ± 0.006
D_s^- Decays	
$\Gamma(\phi\pi^-, \phi \to K^+K^-)/\Gamma(K^+K^-\pi^-)$	0.42 ± 0.05
$\Gamma(K^{*0}K^-, K^*(892)^0 \to K^+\pi^-)/\Gamma(K^+K^-\pi^-)$	0.478 ± 0.061
$\Gamma(\pi^+\pi^-\pi^-)/\Gamma(K^+K^-\pi^-)$	0.235 ± 0.035
$\Gamma(f_0(980)\pi^+, f^0 \to K^+K^-)/\Gamma(K^+K^-\pi^-)$	0.11 ± 0.044
$\Gamma(K^{*0}K^-, K^*(892)^0 \to K^+\pi^-)/\Gamma(\phi\pi^-, \phi \to K^+K^-)$	1.25 ± 0.12
$\Gamma(\pi^+\pi^-\pi^-)/\Gamma(\phi\pi^-, \phi \to K^+K^-)$	0.565 ± 0.071
$\Gamma(K^+K^-\pi^-)/\Gamma_{total}$	0.052 ± 0.009
$\Gamma(\phi\pi^-, \phi \to K^+K^-)/\Gamma_{total}$	0.0216 ± 0.0028
$\Gamma(K^{*0}K^-, K^*(892)^0 \to K^+\pi^-)/\Gamma_{total}$	0.025 ± 0.005
$\Gamma(\pi^+\pi^-\pi^-)/\Gamma_{total}$	0.0101 ± 0.003
$\Gamma(K^+K^-\pi^-NR)/\Gamma_{total}$	0.009 ± 0.004
$\Gamma(f_0(980)\pi^+, f^0 \to K^+K^-)/\Gamma_{total}$	0.0057 ± 0.0025

Table 5.4: The world averages for branching fractions and ratios of branching fractions with uncertainties [1].

The double peak structure about 200 MeV/c^2 below the signal is well described by the hypothesis of $B^0_{(s)} \to D^{*-}_{(s)}\pi^+\pi^+\pi^-$ decay followed by $D^{*-}_{(s)} \to D^-_{(s)}\pi^0$, in which the π_0 from the $D^{*-}_{(s)} \to D^-_{(s)}\pi^0$ decay is not reconstructed. The polarization of the $D^{*-}_{(s)}$ in this type of B decay requires the neutral pion to be aligned either in the direction of $D^{*-}_{(s)}$ momentum, or in the opposite direction, while the $D^-_{(s)}$ trajectory tends to be collinear with the $D^{*-}_{(s)}$ trajectory. Depending on whether the pion was emitted forward or backward with respect to the D^{*-} momentum, the mass of the partially reconstructed B^0 meson falls into one of the two peaks. This feature is less visible in the $B^0_s \to D^{*-}_s\pi^+\pi^+\pi^-$ reconstruction due to the $D^{*-}_s \to D^-_s\gamma$ decay, dominating with branching fraction about 95%.

Tables A.2 and A.5 show the Monte Carlo decay files used to simulate $B^0_{(s)} \to D^{*-}_{(s)}\pi^+\pi^+\pi^-$ decay modes. We introduced $B^0 \to D^{*-}a_1^+$ and $B^0 \to D^{*-}\rho\pi^+$ subresonances because the reflections of these two decay modes are noticeable in our data sample. The template of each $B^0 \to D^-\pi^+\pi^+\pi^-$ component is described with the sum of four Gaussian functions (Figure B-34) with only overall normalizations left free in the data fit. Figures B-40 - B-42 show the $B^0_s \to D^{*-}_s\pi^+\pi^+\pi^-$ templates for

tree D_s^- decay channels, fitted with the function from Eq. 5.2.

The decay mode $\Lambda_b^0 \to \Lambda_c^+\pi^+\pi^-\pi^-, \Lambda_c^+ \to pK^-\pi^+$ with a proton misreconstructed as a pion contributes to the signal mass interval. The template for this mode is fitted with Eq.5.2. To calculate the normalization of the template, we use the measurement of $f_\Lambda/f_d \cdot \mathcal{B}(\Lambda_b \to \Lambda_c\pi)/\mathcal{B}(B^0 \to D^-\pi^+)$ [45], assuming:

$$\frac{\mathcal{B}(\Lambda_b^0 \to \Lambda_c^+\pi^-)}{\mathcal{B}(B^0 \to D^-\pi^+)} = \frac{\mathcal{B}(\Lambda_b^0 \to \Lambda_c^+\pi^+\pi^-\pi^-)}{\mathcal{B}(B^0 \to D^-\pi^+\pi^+\pi^-)} \tag{5.4}$$

We use the measured efficiency of the Λ_b reconstruction from Monte Carlo simulations (Table 4.5), and the branching fractions quoted in Table 5.4.

To create the templates for the rest of the physics background, we use a semi-generic $B \to D_{(s)}^- X$ Monte Carlo simulations with removed $B_{(s)}^0 \to D_{(s)}^-\pi^+\pi^+\pi^-$ signal, $B_{(s)}^0 \to D_{(s)}^- K^-\pi + \pi^+$ Cabibbo suppressed modes, and $B_{(s)}^0 \to D_{(s)}^{*-}\pi^+\pi^+\pi^-$ modes which are already taken into account by individual templates. The remaining mass distributions for B^0 are fitted with the sum of a linear function and a reverse exponential function

$$f_{\rm SG} = N_{\rm SG}((\mu_{01} - f_{01}m) + (\mu_{02} - f_{02}m)(1 - \exp(m|\mu_1\tau_1)) \tag{5.5}$$

The semi-generic templates for B_s^0 modes are fitted with the sum of a linear function and *two* reverse exponential functions

$$\begin{aligned} f_{\rm SG} = N_{\rm SG}((\mu_{01} - f_{01}m) + (\mu_{02} - f_{02}m)(1 - \exp(m|\mu_1\tau_1)) \\ +(\mu_{03} - f_{03}m)(1 - \exp(m|\mu_2\tau_2)) \end{aligned} \tag{5.6}$$

In both equations $N_{\rm SG}$ is the total normalization of the semi-generic template, f_{0x} are the relative normalizations of the terms, μ_{0x} are the turn-on masses for linear and reverse exponential terms.

The turn-ons at approximately 150 MeV/c^2 and 300 MeV/c^2 below the signal peak correspond to the B meson decay modes with one or two pions not reconstructed. The fit for B^0 template is shown on Figure B-33) and the fits for B_s^0 templates are

shown on Figure B-37.

In addition to the physics background common for all the $B^0_{(s)} \to D^-_{(s)}\pi^+\pi^+\pi^-$ modes, we had to create templates for several individual backgrounds. $B^0_s \to D^-_s\pi^+\pi^+\pi^-$ mode with a kaon from $D^-_s \to K^+K^-\pi^-$ misreconstructed as a pion forms a narrow peak under the $B^0 \to D^-\pi^+\pi^+\pi^-$ signal. To model it, we use a semi-generic $B \to D^-_s X$ Monte Carlo simulation with $D^-_s \to \phi\pi^-(K^{*0}K^-)$. We scale the Monte Carlo yield with respect to data by using the data yields of the fully reconstructed modes: $B^0_s \to D^-_s(K^{*0}K^-)\pi^+\pi^+\pi^-$ and $B^0_s \to D^-_s(\phi\pi^-)\pi^+\pi^+\pi^-$. The reconstructed reflection is dominated by the $D^-_s \to K^{*0}K^-$ channel (Fig B-33). It is fitted with a function described by Eq.5.6. Several Gaussian functions are introduced as well to account for spikes.

Sharing the same final state, $B^0 \to D^-D^+_s(\pi^+\pi^+\pi^-)$ decay follows $b \to c\bar{c}s$ quark transition, while $B^0 \to D^-\pi^+\pi^+\pi^-$ decay follows $b \to c\bar{u}d$ quark transition. To account for $B^0 \to D^-D^+_s(\pi^+\pi^+\pi^-)$ mode, we create a template, fitted with a Gaussian function (Figure B-33). To calculate the normalization of the template, we use the fully reconstructed $B^0 \to D^-D^+_s(\pi^+\pi^+\pi^-)$ mode yield from the data.

$B^0_s \to D^-_s(\phi\pi^-)\pi^+\pi^+\pi^-$ mode has a contribution from $B^0_s \to D^-_s(f_0\pi^-, f^0 \to K^+K^-)\pi^+\pi^+\pi^-$ mode with a branching fraction measured in Reference [46] based on a Dalitz analysis of 701 D^-_s decays. To create a template for this mode, we use Monte Carlo simulation with the most recent branching fractions for $D^-_s \to \phi\pi^-, \phi \to K^+K^-$ and $D^-_s \to f_0\pi^-, f^0 \to K^+K^-$ decays (Table 5.4).

We use measured signal yield for $B^0_s \to D^-_s(\phi\pi^-)\pi^+\pi^+\pi^-$ to calculate the scale factor for our Monte Carlo simulation (Figure 5-3). We determine the contribution of the template to be $(3.5 \pm 2)\%$ of the $B^0_s \to D^-_s(\phi\pi^-)\pi^+\pi^+\pi^-$ signal yield. The large uncertainty is due to the $\mathcal{B}(D^-_s \to f_0\pi^+, f^0 \to K^+K^-)$ uncertainty.

$B^0_s \to D^-_s(K^{*0}K^-)\pi^+\pi^+\pi^-$ mode has a large contribution from $B^0 \to D^-\pi^+\pi^+\pi^-$ mode with one pion reconstructed as a kaon. This contribution is negligible for $B^0_s \to D^-_s(\phi\pi^-)\pi^+\pi^+\pi^-$ reconstruction due to the narrow ϕ mass window, but should be considered for $B^0_s \to D^-_s(K^{*0}K^-)\pi^+\pi^+\pi^-$ reconstruction. The reflection is fitted with four Gaussian functions (Figure B-44).

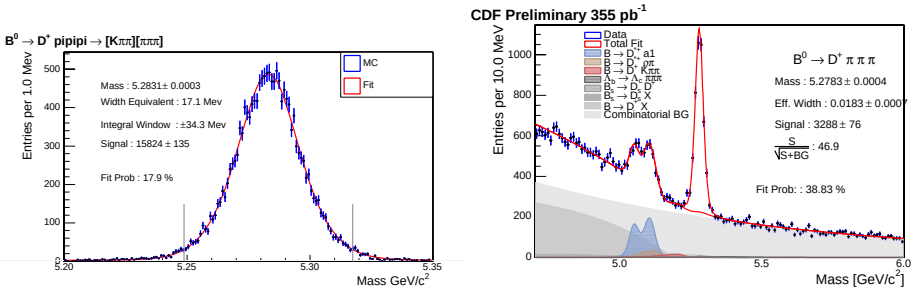

Figure 5-2: $B^0 \to D^-\pi^+\pi^+\pi^-$ Monte Carlo and data signal used to scale the reflection templates.

To calculate the normalization of the reflection, we calculate Monte Carlo scale factor (4.513) by dividing the signal Monte Carlo yield 14839 ± 122 by the observed signal yield 3288 ± 76 (Figure 5-2). The template shown on Figure B-44 is scaled down to the corresponding data luminosity by multiplying the overall normalization of the template by 1/4.513. The normalization of the template is fixed when fitting the data.

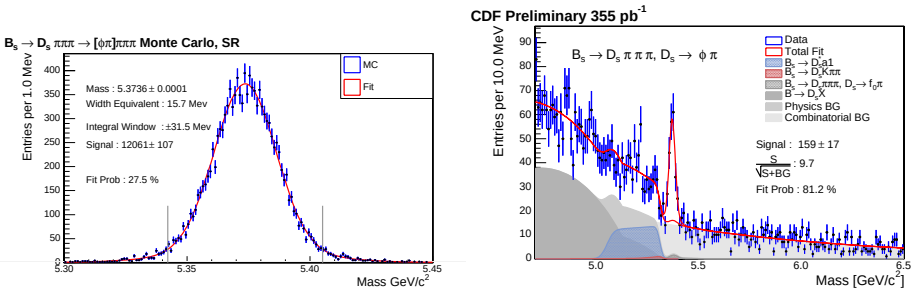

Figure 5-3: $B_s^0 \to D_s^-\pi^+\pi^+\pi^-$ Monte Carlo and data signal used to scale the reflection templates.

The reconstruction of the $B_s^0 \to D_s^-(K^{*0}K^-)\pi^+\pi^+\pi^-$ mode has a contribution from similar B meson decays into a non-resonant $D_s^- \to K^+K^-\pi^-$ channel. The reconstruction of $B_s^0 \to D_s^-(\phi\pi^-)\pi^+\pi^+\pi^-$ mode is much less affected by this reflection because of the narrow ϕ mass window. Despite the identical particle content of the reflecting mode, we have to isolate its contribution in order to use measured $D_s^- \to K^{*0}K^-$ branching fraction in our calculations. Branching fractions for $D_s^- \to \phi\pi^-, \phi \to K^+K^-$, and non-resonant $D_s^- \to K^+K^-\pi^-$ modes, used for

Monte Carlo simulation are listed in Table 5.4. We use the measured signal yield of $B_s^0 \to D_s^-(\phi\pi^-)\pi^+\pi^+\pi^-$ to calculate the scale factor for our Monte Carlo simulation (Figure 5-3). We determine the contribution of the template to be $(9 \pm 4)\%$ of the $B_s^0 \to D_s^-(K^{*0}K^-)\pi^+\pi^+\pi^-$ signal yield. The large uncertainty is due to the uncertainty of the branching fraction $\mathcal{B}(D_s^- \to K^+K^-\pi^-)$.

The $B_s^0 \to D_s^-(K^{*0}K^-)\pi^+\pi^+\pi^-$ reconstruction window has contributions from B meson decays going through $D^- \to K^+\pi^-\pi^-$ and $\overline{D^0} \to K^-\pi^+$ channels (Figure B-43). This reflection is fitted with the function described by Eq. 5.5. To calculate the normalization of the template, we use the data yield of $B^+ \to \overline{D^0}\pi^+, \overline{D^0} \to K^-\pi^+$ mode from reference [47] The large uncertainty on the normalization of the reflection is due to the limited knowledge of the content of the semi-generic Monte-Carlo simulation.

Reflection	Normalization
$B^0 \to D^{*-}a_1^+$	floating
$B^0 \to D^{*-}\rho\pi^+$	floating
Cabibbo suppressed	$6.9\% \pm 2\%$
$\Lambda_b^0 \to \Lambda_c^+\pi^+\pi^-\pi^-, \Lambda_c^+ \to pK^-\pi^+$	$3.0\% \pm 1\%$
$B_s^0 \to D_s^-(K^{*0}K^-)\pi^+\pi^+\pi^-$	$2.8\% \pm 0.3\%$
$B^0 \to D^-(K^+\pi^-\pi^-)X$	floating

Table 5.5: Normalizations of physics background templates for $B^0 \to D^-\pi^+\pi^+\pi^-$.

Reflection	$D_s^- \to \phi\pi^-$	$D_s^- \to K^{*0}K^-$	$D_s^- \to \pi^+\pi^-\pi^-$
$B_s^0 \to D_s^{*-}a_1^+$	floating	floating	floating
Cabibbo suppressed	$6.9\% \pm 2\%$	$6.9\% \pm 2\%$	$6.9\% \pm 2\%$
$\Lambda_b^0 \to \Lambda_c^+\pi^+\pi^-\pi^-, \Lambda_c^+ \to pK^-\pi^+$	-	20 ± 9	-
$B^0 \to D^-\pi^+\pi^+\pi^-$	-	155 ± 6	-
$B^+ \to D^0(K^-\pi^+)X$	-	80 ± 40	-
$B^0 \to D^-(K^+\pi^-\pi^-)X$	-	250 ± 50	-
$B_s^0 \to D_s^-X$	floating	floating	floating

Table 5.6: Normalizations of physics background templates for $B_s^0 \to D_s^-\pi^+\pi^+\pi^-$.

When the fit for the data is performed, all template parameters except for the normalizations are fixed. The full account of the normalizations of the physics background templates for $B_{(s)}^0 \to D_{(s)}^-\pi^+\pi^+\pi^-$ decay modes is given in Tables 5.5 and

5.6. The entries *"floating"* in the table mean that the normalization of the template is allowed to float in the fit for the data. The entries given in [%] provide the template contribution with respect to corresponding $B^0_{(s)} \to D^-_{(s)}\pi^+\pi^+\pi^-$ signal yield. All other entries provide the number of events. All mass parameters of the templates are corrected by -4.85 MeV/c^2, and the Gaussian widths of the templates are corrected by $17 \pm 3\%$ following the results of our study in Section 5.3.

5.2.2 Physics Background Templates for $B^0 \to D^- D_s^+$

Three different sets of templates are created for $B^0 \to D^- D_s^+$ modes with three D_s^- decay channels. Several templates are common for all three modes:

- $B^0 \to D^- D_s^{*+}$ modes with non-reconstructed $\gamma(\pi_0)$ from $D_s^{*+} \to D_s^+\gamma(\pi^0)$,
- $B^0 \to D^{*-} D_s^+$ modes with non-reconstructed π_0 from $D^{*-} \to D^-\pi^0$,
- $B^0 \to D^{*-} D_s^{*+}$ modes with π^0 and γ or two π^0 not reconstructed,
- Reflection from semi-generic $B^0 \to D^-(K^+\pi^-\pi^-)X$ modes.

The reconstruction of the $B^0 \to D^- D_s^+(K^{*0}K^+)$ decay mode has a reflection from $D^- \to K^+\pi^-\pi^-$ decay with one pion reconstructed as a kaon in the reconstruction window.

For every mode, we construct three separate templates describing reflections from $B^0 \to D^- D_s^{*+}$, $B^0 \to D^{*-} D_s^+$ and $B^0 \to D^{*-} D_s^{*+}$ modes. Only the overall normalizations of these templates are allowed to float in the data fit. A study of $B^0 \to D^{*-} D_s^{*+}$ reflections is done with the perspective to implement it for the reconstruction of the corresponding $B_s^0 \to D_s^{(*+)} D_s^{(*-)}$ modes which will improve our sensitivity to $\Delta\Gamma_s^{\rm CP}/\Gamma_s$. The templates for $D_s^- \to \phi\pi^-$, $D_s^- \to K^{*0}K^-$, and $D_s^- \to \pi^+\pi^-\pi^-$ are shown on Figures B-45, B-46, and B-47, respectively.

The reconstruction of $B^0 \to D^- D_s^{*+}$ modes with non-reconstructed $\gamma(\pi_0)$ from the $D_s^{*+} \to D_s^+\gamma(\pi^0)$ decay creates a reflection about 140 MeV/c^2 below the signal. We fit it with three Gaussians relying on the large statistics of generated Monte Carlo simulations. The featureless $D_s^{*+} \to D_s^+\gamma$ mode has a dominant $(94.2 \pm 2.5\%)$ contribution to the template. The small double peak structure, due to the admixture

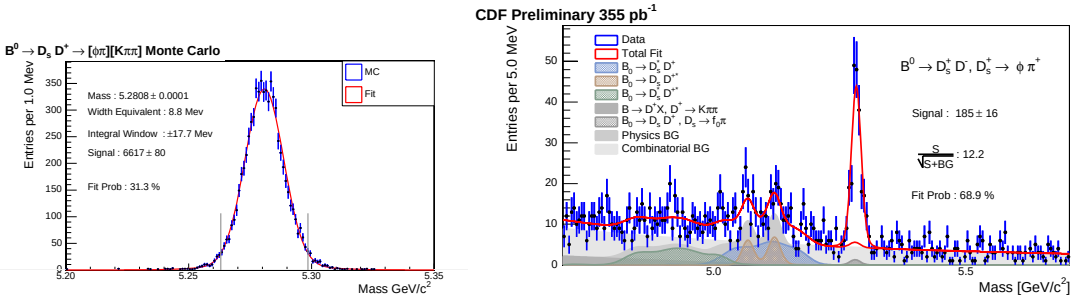

Figure 5-4: $B^0 \to D^- D_s^+ (\phi\pi^+)$ Monte Carlo and data signal used to scale the reflection templates.

of the $D_s^{*+} \to D_s^+ \pi^0$ mode, is negligible with our statistics, considering that the two modes have the same reconstruction efficiency. The systematic uncertainty of the fit due to the uncertainty of the D_s^{*+} branching fractions is discussed in Section 8.5.3.

$B^0 \to D^{*-} D_s^+$ modes with a non-reconstructed π_0 from the $D^{*-} \to D^- \pi^0$ decay create a double peak structure near 5.1 GeV/c^2. It is well described by a hypothesis of $B^0 \to D^{*-} D_s^+$ decay followed by $D^{*-} \to D^- \pi^0$ decay, in which the π_0 from $D^{*-} \to D^- \pi^0$ is not reconstructed. The polarization of the D^{*-} in this type of B decay requires the neutral pion to be aligned either in the direction of D^{*-} momentum or in the opposite direction, while the D^- trajectory tends to be collinear with the D^{*-} trajectory. Depending on whether the pion is emitted forward or backward with respect to the D^{*-} momentum, the mass of the partially reconstructed B^0 meson falls into one of the two peaks. The shape is fitted with three Gaussians.

$B^0 \to D_s^{*+} D^{*-}$ modes with lost π^0 mesons and γ from the decays of the excited D-mesons create a wide bump about 300 MeV/c^2 below the signal. The reflection is fitted with three Gaussians.

When the $B^0 \to D^- D_s^+$ signals and the reflections discussed above are removed from the semi-generic $B^0 \to D^-(K^+\pi^-\pi^-)X$ Monte Carlo simulation, the rest of the background is concentrated in the low mass region and is approximated with a straight line.

The reconstruction of the $B^0 \to D^- D_s^+ (K^{*0} K^+)$ mode has a contribution from the $B^0 \to D^- \pi^+ \pi^+ \pi^-$ mode with two pions reconstructed as kaons. The reflection

$B^0 \to D^-(K^+\pi^-\pi^-)D_s^+$	$D_s^- \to \phi\pi^-$	$D_s^- \to K^{*0}K^-$	$D_s^- \to \pi^+\pi^-\pi^-$
$B^0 \to D^- D_s^{*+}$	floating	floating	floating
$B^0 \to D^{*-} D_s^+$	floating	floating	floating
$B^0 \to D^{*-} D_s^{*+}$	floating	floating	floating
$B^0 \to D^- D_s^+(f_0\pi^+)$	$3.5 \pm 2\%$	-	-
$B^0 \to D^- D_s^+(K^+K^-\pi^+)$	-	$(10 \pm 5)\%$	-
$B^0 \to D^-\pi^+\pi^+\pi^-$	-	30 ± 3	30 ± 3
$B^0 \to D^-(K^+\pi^-\pi^-)X$	floating	floating	floating

Table 5.7: Normalizations of physics background templates for $B^0 \to D^- D_s^+$.

is very wide and located well above the signal. We use the measured signal yield of $B^0 \to D^-\pi^+\pi^+\pi^-$ mode and Monte Carlo simulation (Figure 5-2) to calculate the scale factor for this template (Figure B-49).

The reconstruction of the $B^0 \to D^- D_s^+(\pi^+\pi^+\pi^-)$ mode has a contribution from the $B^0 \to D^-\pi^+\pi^+\pi^-$ mode under the signal. We use the signal yield from data for the $B^0 \to D^-\pi^+\pi^+\pi^-$ mode and Monte Carlo simulation (Figure 5-2) to calculate the scale factor for this template (Figure B-49).

Some of the $B^0 \to D^- D_s^+$ decay modes are very similar and contribute to each other, i.e. *crosstalk*. To evaluate the contribution of the crosstalks, we create a Monte Carlo simulation with the most recent information about D_s^- decay branching fractions in our decay tables (Table A.6). We introduce crosstalk templates and estimate their normalizations relative to the signal by artificially removing the signal mode contribution from Monte Carlo simulations (Figure B-50). The accuracy of this estimate is limited by the current knowledge of D_s^- meson branching fractions. The contribution under the $B^0 \to D^- D_s^+(\phi\pi^+)$ signal peak is mostly due to the $D_s^- \to f_0\pi^-$ with $f^0 \to K^+K^-$ decay mode. The contribution under the $B^0 \to D^- D_s^+(K^{*0}K^+)$ signal peak is mostly due to the non-resonant $D_s^- \to K^+K^-\pi^-$ decay mode. The contribution under the $B^0 \to D^- D_s^+(\pi^+\pi^+\pi^-)$ signal peak is negligible.

The full account of the normalization of the physics background templates is given in Table 5.7. The entries *"floating"* mean that the normalization of the template is allowed to float in data fit. The entries given in [%] provide the template contribution with respect to the corresponding $B^0 \to D^- D_s^+$ signal yield. The widths of the

Gaussian templates for $B^0 \to D^- D_s^+$ are corrected by $16 \pm 2\%$ following the results of our study in Section 5.3.

5.2.3 Physics Background Templates for $B_s^0 \to D_s^- D_s^+$

Mass distributions of $B_s^0 \to D_s^- D_s^+$ modes are fitted in the $[5.3, 6.1]$ GeV/c^2 interval. $B_s^0 \to D_s^-(\phi\pi^-)D_s^+(\phi\pi^+)$ mode is also fitted in $[4.7, 6.5]$ GeV/c^2 mass range with additional templates for reflections from the misrecontructed $B_s^0 \to D_s^{*+} D_s^{(*)-}$ modes. There are several reflecting modes which require the construction of the templates.

- $B_s^0 \to D_s^-(\phi\pi^-)D_s^+(K^{*0}K^+)$ mode has a strong reflection from $B^0 \to D^- D_s^+(\phi\pi^+)$,
- $B_s^0 \to D_s^-(\phi\pi^-)D_s^+(\pi^+\pi^+\pi^-)$ mode has a reflection from $B_s^0 \to D_s^-\pi^+\pi^+\pi^-$,
- The contribution from $B_s^0 \to D_s^{*+} D_s^-$ and $B_s^0 \to D_s^{*+} D_s^{*-}$ have to be taken into account when fitting a wider mass window.

The reconstruction of $B_s^0 \to D_s^-(\phi\pi^-)D_s^+(K^{*0}K^+)$ mode has a strong reflection from $B^0 \to D^- D_s^+(\phi\pi^+)$ mode under the signal. This reflection is significantly reduced by applying $D^- \to K^+\pi^-\pi^-$ veto, discussed in Section 8.4. We use our $B^0 \to D^- D_s^+$ signal Monte Carlo simulation to create the template for the residual reflection (Figure B-52). We use the measured signal yield of $B^0 \to D^- D_s^+(\phi\pi^+)$ and Monte Carlo simulation (Figure 5-4) to calculate the scale factor for the template.

The reconstruction of $B_s^0 \to D_s^-(\phi\pi^-)D_s^+(\pi^+\pi^+\pi^-)$ mode has a reflection from $B_s^0 \to D_s^-(\phi\pi^-)\pi^+\pi^+\pi^-$ mode under the signal. We use our signal Monte Carlo for $B_s^0 \to D_s^-(\phi\pi^-)\pi^+\pi^+\pi^-$ mode to create the template (Figure B-52). The normalization is determined by we use the measured signal yield of $B_s^0 \to D_s^-(\phi\pi^-)\pi^+\pi^+\pi^-$ and Monte Carlo simulation (Figure 5-3).

To fit $B_s^0 \to D_s^-(\phi\pi^-)D_s^+(\phi\pi^+)$ in a wider mass range (Figure B-54), we create templates for $B_s^0 \to D_s^{*+} D_s^-$ and $B_s^0 \to D_s^{*+} D_s^{*-}$ reflections (Figure B-51) fitted with triple Gaussian functions, the same way it is done with $B^0 \to D^{(*)-} D_s^{(*)+}$ templates used to fit the reconstructed mass distribution of $B^0 \to D^- D_s^+$ modes. A study of $B_s^0 \to D_s^{*-} D_s^{*+}$ reflections is done with the idea to extract $B_s^0 \to D_s^{(*+)} D_s^{(*-)}$ signal yields for better measurement of $\Delta\Gamma_s^{\rm CP}/\Gamma_s$ lower bound.

For each D_s^- decay channel, the $B_s^0 \to D_s^- D_s^+$ signal regions contain the crosstalks from the other D_s^- channels with the same final states. We estimate the crosstalk contribution with respect to the signal by using Monte Carlo simulation with the decay table implementing the latest knowledge of D_s^- branching fractions listed in Table A.8 [1]. The contribution under the $B_s^0 \to D_s^-(\phi\pi^-)D_s^+(\phi\pi^+)$ signal peak is dominated by the $B_s^0 \to D_s^+(\phi\pi^+)D_s^-(f_0\pi^-)$ mode, with $f^0 \to K^+K^-$. The contribution under the $B_s^0 \to D_s^-(\phi\pi^-)D_s^+(K^{*0}K^+)$ signal peak is dominated by the $B_s^0 \to D_s^+(\phi\pi^+)D_s^-(K^+K^-\pi^-)$ mode. The contribution under the $B_s^0 \to D_s^-(\phi\pi^-)D_s^+(\pi^+\pi^+\pi^-)$ signal peak is dominated by the $B_s^0 \to D_s^+(f_0\pi^+)D_s^-(\pi^+\pi^-\pi^-)$ mode, with $f^0 \to K^+K^-$. The large systematic uncertainty of the cross-talk normalization is due to the uncertainty of the $\mathcal{B}(D_s^- \to K^+K^-\pi^-)$.

Reflection	$D_s^- \to \phi\pi^-$	$D_s^- \to K^{*0}K^-$	$D_s^- \to \pi^+\pi^-\pi^-$
$B^0 \to D^- D_s^+(\phi\pi^+)$	-	fixed	-
$B_s^0 \to D_s^-(\pi^+\pi^-\pi^-)\pi^+\pi^+\pi^-$	-	-	fixed
$B_s^0 \to D_s^+(\phi\pi^+)D_s^-(K^+K^-\pi^-)$	fixed	fixed	fixed
$B_s^0 \to D_s^{*+} D_s^-$	floating	-	-
$B_s^0 \to D_s^{*+} D_s^{*-}$	floating	-	-
$B_s^0 \to D_s^-(\phi\pi^-)X$	floating	-	-

Table 5.8: Normalizations of physics background templates for $B_s^0 \to D_s^- D_s^+$.

The full account of the normalization of the physics background templates for $B_s^0 \to D_s^- D_s^+$ modes is given in Table 5.8. The entries *"floating"* mean that the normalization of the template is allowed to float in data fit. The entries given in [%] provide the template contribution with respect to corresponding $B_s^0 \to D_s^- D_s^+$ signal yield. All other entries provide the number of events. The masses of the B_s^0 meson signal templates are fixed to world average [1] B_s^0 mass values. The widths of the Gaussian templates for $B_s^0 \to D_s^- D_s^+$ modes are corrected by $16 \pm 2\%$ following the results of our study in Section 5.3.

5.3 Combinatorial Background

All the data mass distributions have a similar combinatorial background. For modes with large statistics, the combinatorial background is fitted with the sum of a constant and an exponent function (Eq. 5.7).

$$f_{\text{comb}} = f_1 \exp(m|\mu\tau) + f_2 \tag{5.7}$$

Normalization and the slope of the exponent along with normalization of the constant are allowed to float, leaving three free parameters.

Chapter 6

Extraction of Branching Fractions

Knowing the signal yield of $B^0_{(s)} \to D^-_{(s)}\pi^+\pi^+\pi^-$ and $B^0_{(s)} \to D^-_{(s)}D^+_s$, the efficiency of reconstruction, measured with Monte Carlo simulations, and the branching fractions of the relevant D meson decays we may calculate the ratios of branching fractions (Eq. 1.13 - 1.16). We fit the reconstructed mass distributions with binned likelihood fits using the functions described in Section 5. The data fit for $B^0 \to D^-\pi^+\pi^+\pi^-$ mode is shown in Figure 6-1. The data fits for $B^0_s \to D^-_s\pi^+\pi^+\pi^-$, $B^0 \to D^-D^+_s$, and $B^0_s \to D^-_s D^+_s$ modes are shown in Figures 6-3, 6-4, and 6-5 respectively. Unless otherwise specified, we fit the reconstructed mass distributions in mass interval $[4.6, 6.5]$ GeV/c^2, and obtain fit probabilities by calculating binned χ^2, combining low statistics bins, if needed, to accumulate at least 20 events. Signal yields with their statistical uncertainties are summarized in Table 6.1. To find the yields for $B^0_{(s)} \to D^-_{(s)}\pi^+\pi^+\pi^-$, $B^0 \to D^-D^+_s$, and $B^0_s \to D^-_s D^+_s$ modes, the signal templates are integrated using effective width. The yields for $B^0 \to D^{(*)-}D^{(*)+}_s$ modes are integrated to include 100% of the signal.

The known branching fractions, which we use for our calculations, are summarized in Table 5.4. The ratios of D^-_s branching fractions are measured better than their absolute values. For these ratios we use the inclusive $\mathcal{B}(D^-_s \to \phi\pi^-)$ as a common denominator because its fraction is well measured and it enters directly into the formula for the cleanest B meson decay channel with $D^-_s \to \phi\pi^-$. To calculate

Mode	Yield
$B^0 \to D^-\pi^+\pi^+\pi^-$	3288 ± 76
$B_s^0 \to D_s^-(\phi\pi^-)\pi^+\pi^+\pi^-$	160 ± 17
$B_s^0 \to D_s^-(K^{*0}K^-)\pi^+\pi^+\pi^-$	90 ± 17
$B_s^0 \to D_s^-(\pi^+\pi^-\pi^-)\pi^+\pi^+\pi^-$	49 ± 11
$B^0 \to D^-D_s^+(\phi\pi^+)$	183 ± 15
$B^0 \to D^-D_s^+(K^{*0}K^+)$	128 ± 13
$B^0 \to D^-D_s^+(\pi^+\pi^+\pi^-)$	84 ± 13
$B^0 \to D^-D_s^{*+}$	158 ± 34
$B^0 \to D^{*-}D_s^+$	75 ± 22
$B^0 \to D^{*-}D_s^{*+}$	133 ± 25
$B_s^0 \to D_s^-(\phi\pi^-)D_s^+(\phi\pi^+)$	$9.2^{+3.5}_{-2.9}$
$B_s^0 \to D_s^-(\phi\pi^-)D_s^+(K^{*0}K^+)$	$6.0^{+3.4}_{-2.7}$
$B_s^0 \to D_s^-(\phi\pi^-)D_s^+(\pi^+\pi^+\pi^-)$	$8.3^{+3.5}_{-2.8}$

Table 6.1: Yields extracted from data.

$\mathcal{B}(B_s^0 \to D_s^-\pi^+\pi^+\pi^-)/\mathcal{B}(B^0 \to D^-\pi^+\pi^+\pi^-)$ we use formulas:

$$\frac{\mathcal{B}(B_s^0 \to D_s^-(\phi\pi^-)\pi^+\pi^+\pi^-)}{\mathcal{B}(B^0 \to D^-\pi^+\pi^+\pi^-)} = \frac{N(D_s 3\pi)}{N(D3\pi)} \cdot \frac{\epsilon(D3\pi)}{\epsilon(D_s 3\pi)} \cdot \frac{D^- \to K^+\pi^-\pi^-}{\mathcal{B}(D_s^- \to \phi(K^+K^-)\pi^-)},$$

$$\frac{\mathcal{B}(B^0 \to D_s^-(K^{*0}K^-)\pi^+\pi^+\pi^-)}{\mathcal{B}(B^0 \to D^-\pi^+\pi^+\pi^-)} = \frac{N(D_s 3\pi)}{N(D3\pi)} \cdot \frac{\epsilon(D3\pi)}{\epsilon(D_s 3\pi)} \cdot \frac{D^- \to K^+\pi^-\pi^-}{r_2 \cdot \mathcal{B}(D_s^- \to \phi(K^+K^-)\pi^-)},$$

where

$$r_2 = \frac{\mathcal{B}(D_s^- \to K^{*0}(K^-\pi^+)K^-)}{\mathcal{B}(D_s^- \to \phi(K^+K^-)\pi^-)},$$

$$\frac{\mathcal{B}(B^0 \to D_s^-(\pi^+\pi^-\pi^-)\pi^+\pi^+\pi^-)}{\mathcal{B}(B^0 \to D^-\pi^+\pi^+\pi^-)} = \frac{N(D_s 3\pi)}{N(D3\pi)} \cdot \frac{\epsilon(D3\pi)}{\epsilon(D_s 3\pi)} \cdot \frac{D^- \to K^+\pi^-\pi^-}{r_3 \cdot \mathcal{B}(D_s^- \to \phi(K^+K^-)\pi^-)},$$

where

$$r_3 = \frac{\mathcal{B}(D_s^- \to \pi^+\pi^-\pi^-)}{\mathcal{B}(D_s^- \to \phi(K^+K^-)\pi^-)}.$$

$\Gamma(K^{*0}K^-)/\Gamma(\phi\pi^-)$ ratio quoted in Table 5.4 is taken from [48]. Using efficiency values

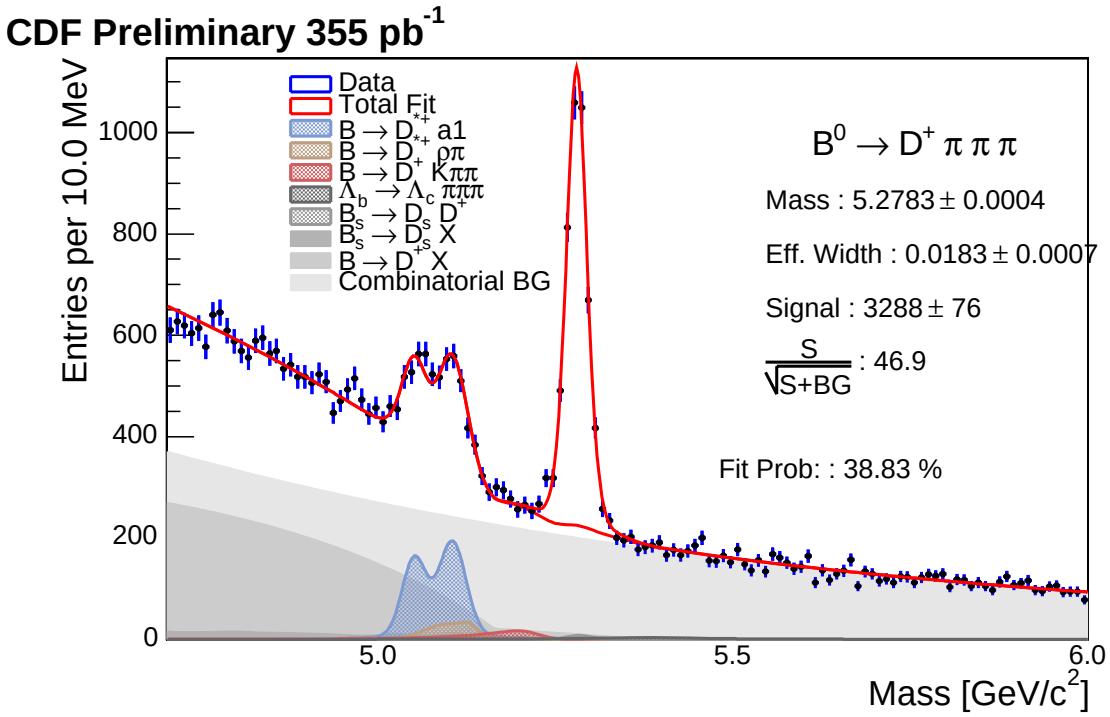

Figure 6-1: Reconstructed $B^0 \to D^-\pi^+\pi^+\pi^-$ mass distribution.

from Table 4.5 and yields from Table 6.1, for three D_s^- decay channels separately, we obtain:

$$\frac{f_s}{f_d} \cdot \frac{\mathcal{B}(B_s^0 \to D_s^-(\phi\pi^-)\pi^+\pi^+\pi^-)}{\mathcal{B}(B^0 \to D^-\pi^+\pi^+\pi^-)} = 0.263 \pm 0.029 \pm 0.035(\mathcal{B}),$$

$$\frac{f_s}{f_d} \cdot \frac{\mathcal{B}(B_s^0 \to D_s^-(K^{*0}K^-)\pi^+\pi^+\pi^-)}{\mathcal{B}(B^0 \to D^-\pi^+\pi^+\pi^-)} = 0.274 \pm 0.053 \pm 0.045(\mathcal{B}),$$

$$\frac{f_s}{f_d} \cdot \frac{\mathcal{B}(B_s^0 \to D_s^-(\pi^+\pi^-\pi^-)\pi^+\pi^+\pi^-)}{\mathcal{B}(B^0 \to D^-\pi^+\pi^+\pi^-)} = 0.293 \pm 0.067 \pm 0.054(\mathcal{B}),$$

where $(\mathcal{B})$ is the uncertainty due to the $\mathcal{B}(D^- \to K^+\pi^-\pi^-)/\mathcal{B}(D_s^- \to \phi\pi^-)$. Using the latest world average value $f_s/f_d = 0.259 \pm 0.038$ [1], we calculate the ratio of

branching fractions. For our dataset we obtain

$$\frac{\mathcal{B}(B_s^0 \to D_s^-(\phi\pi^-)\pi^+\pi^+\pi^-)}{\mathcal{B}(B^0 \to D^-\pi^+\pi^+\pi^-)} = 1.02 \pm 0.11 \pm 0.15(f_s/f_d) \pm 0.14(\mathcal{B}),$$

$$\frac{\mathcal{B}(B_s^0 \to D_s^-(K^{*0}K^-)\pi^+\pi^+\pi^-)}{\mathcal{B}(B^0 \to D^-\pi^+\pi^+\pi^-)} = 1.06 \pm 0.20 \pm 0.16(f_s/f_d) \pm 0.17(\mathcal{B}),$$

$$\frac{\mathcal{B}(B_s^0 \to D_s^-(\pi^+\pi^-\pi^-)\pi^+\pi^+\pi^-)}{\mathcal{B}(B^0 \to D^-\pi^+\pi^+\pi^-)} = 1.13 \pm 0.26 \pm 0.17(f_s/f_d) \pm 0.21(\mathcal{B}).$$

To calculate $\mathcal{B}(B^0 \to D^- D_s^+(\phi\pi^+))/\mathcal{B}(B^0 \to D^-\pi^+\pi^+\pi^-)$, we use formulas:

$$\frac{\mathcal{B}(B^0 \to D^- D_s^+(\phi\pi^+))}{\mathcal{B}(B^0 \to D^-\pi^+\pi^+\pi^-)} = \frac{N(D_sD)}{N(D3\pi)} \cdot \frac{\epsilon(D3\pi)}{\epsilon(D_sD)} \cdot \frac{1}{\mathcal{B}(D_s^- \to \phi(K^+K^-)\pi^-)},$$

$$\frac{\mathcal{B}(B^0 \to D^- D_s^+(K^{*0}K^+))}{\mathcal{B}(B^0 \to D^-\pi^+\pi^+\pi^-)} = \frac{N(D_sD)}{N(D3\pi)} \cdot \frac{\epsilon(D3\pi)}{\epsilon(D_sD)} \cdot \frac{1}{r_2 \cdot \mathcal{B}(D_s^- \to \phi(K^+K^-)\pi^-)},$$

where

$$r_2 = \frac{\mathcal{B}(D_s^- \to K^{*0}(K^-\pi^+)K^-)}{\mathcal{B}(D_s^- \to \phi(K^+K^-)\pi^-)},$$

$$\frac{\mathcal{B}(B^0 \to D^- D_s^+(\pi^+\pi^+\pi^-))}{\mathcal{B}(B^0 \to D^-\pi^+\pi^+\pi^-)} = \frac{N(D_sD)}{N(D3\pi)} \cdot \frac{\epsilon(D3\pi)}{\epsilon(D_sD)} \cdot \frac{1}{r_3 \cdot \mathcal{B}(D_s^- \to \phi(K^+K^-)\pi^-)},$$

where

$$r_3 = \frac{\mathcal{B}(D_s^- \to \pi^+\pi^-\pi^-)}{\mathcal{B}(D_s^- \to \phi(K^+K^-)\pi^-)}.$$

Using efficiency values from Table 4.5 and yields from Table 6.1, for three D_s^- decay

channels separately, we obtain

$$\frac{\mathcal{B}(B^0 \to D^- D_s^+(\phi\pi^+))}{\mathcal{B}(B^0 \to D^-\pi^+\pi^+\pi^-)} = 1.59 \pm 0.14 \pm 0.21(\mathcal{B}),$$

$$\frac{\mathcal{B}(B^0 \to D^- D_s^+(K^{*0}K^+))}{\mathcal{B}(B^0 \to D^-\pi^+\pi^+\pi^-)} = 1.44 \pm 0.15 \pm 0.23(\mathcal{B}),$$

$$\frac{\mathcal{B}(B^0 \to D^- D_s^+(\pi^+\pi^+\pi^-))}{\mathcal{B}(B^0 \to D^-\pi^+\pi^+\pi^-)} = 1.45 \pm 0.23 \pm 0.26(\mathcal{B}).$$

The uncertainty due to the branching fractions ($\mathcal{B}$) has the common part introduced by $\mathcal{B}(D_s^- \to \phi\pi^-)$, and the individual parts introduced by ratios r_2 and r_3. The uncertainties are discussed further in the next section.

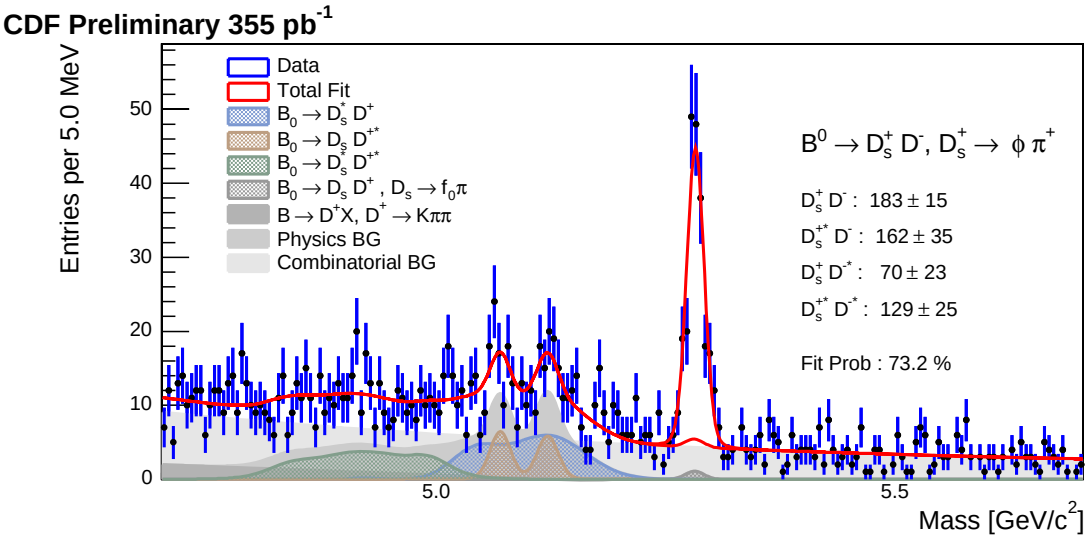

Figure 6-2: Reconstructed $B^0 \to D^- D_s^+(\phi\pi^+)$ mass distribution. The yields for $B^0 \to D^{(*)-} D_s^{(*)+}$ modes are printed with errors.

The reconstruction of $B^0 \to D^- D_s^+(\phi\pi^+)$ has low combinatorial background and allows us to estimate the branching fractions of the $B_s^0 \to D^{(*)-} D_s^{(*)+}$ decay modes (Figure 6-2). The $B^0 \to D^- D_s^+(K^{*0}K^+)$ and $B^0 \to D^- D_s^+(\pi^+\pi^+\pi^-)$ decay modes are are not used for this study because they have a large combinatorial background

and large systematic uncertainties, arising from the limited knowledge of the physics background composition. We calculate the ratios of branching fractions using the formulas:

$$\frac{\mathcal{B}(B^0 \to D^- D_s^{*+})}{\mathcal{B}(B^0 \to D^- D_s^+)} = \frac{N(D^- D_s^{*+})}{N(D^- D_s^+)} \cdot \frac{\epsilon(D^- D_s^+)}{\epsilon(D^- D_s^{*+})},$$

$$\frac{\mathcal{B}(B^0 \to D_s^- D^{*+})}{\mathcal{B}(B^0 \to D^- D_s^+)} = \frac{N(D^{*-} D_s^+)}{N(D^- D_s^+)} \cdot \frac{\epsilon(D^- D_s^+)}{\epsilon(D^{*-} D_s^+)},$$

$$\frac{\mathcal{B}(B^0 \to D_s^* D^{*+})}{\mathcal{B}(B^0 \to D^- D_s^+)} = \frac{N(D^{*-} D_s^{*+})}{N(D^- D_s^+)} \cdot \frac{\epsilon(D^- D_s^+)}{\epsilon(D^{*-} D_s^{*+})}.$$

Employing the efficiencies from Table 4.5 and yields from Table 6.1, we calculate the ratios of branching fractions for three different $B^0 \to D^{(*)-} D_s^{(*)+}$ modes

$$\frac{\mathcal{B}(B^0 \to D^- D_s^{*+})}{\mathcal{B}(B^0 \to D^- D_s^+)} = 0.89 \pm 0.20,$$

$$\frac{\mathcal{B}(B^0 \to D^{*-} D_s^+)}{\mathcal{B}(B^0 \to D^- D_s^+)} = 1.47 \pm 0.45,$$

$$\frac{\mathcal{B}(B^0 \to D^{*-} D_s^{*+})}{\mathcal{B}(B^0 \to D^- D_s^+)} = 2.59 \pm 0.51.$$

The results do not contain any branching fraction uncertainty because the D meson branching fractions cancel out in the ratios. The systematic uncertainties are further discussed in the next section.

We fit $B_s^0 \to D_s^- D_s^+$ data in mass interval $[5.3, 6.0]$ GeV/c^2. Signal yields for the $B^0 \to D^- D_s^+$ $B_s^0 \to D_s^- D_s^+$ modes are summarized in Table 6.1 together with their uncertainties. In all $B_s^0 \to D_s^- D_s^+$ decay modes at least one of the D_s^+ mesons decays into $\phi\pi^+$ and the other D_s^- meson decays into $\phi\pi^-$, $K^{*0}K^-$, or $\pi^+\pi^-\pi^-$. In the

$B^0 \to D^- D_s^+$ decay mode, the D_s^+ meson decays into $\phi\pi^+$, $K^{*0}K^+$, or $\pi^+\pi^+\pi^-$. We form $\mathcal{B}(B_s^0 \to D_s^- D_s^+)/\mathcal{B}(B^0 \to D^- D_s^+)$ ratios for three different D_s^- modes so that only $\mathcal{B}(D_s^- \to \phi\pi^-)$ appears in the final answer, and the other D_s^- branching fractions cancel in the ratio

$$\frac{\mathcal{B}(B_s^0 \to D_s^-(\phi\pi^-)D_s^+(\phi\pi^+))}{\mathcal{B}(B^0 \to D^- D_s^+(\phi\pi^+))},$$

$$\frac{\mathcal{B}(B_s^0 \to D_s^-(\phi\pi^-)D_s^+(K^{*0}K^+))}{\mathcal{B}(B^0 \to D^- D_s^+(K^{*0}K^+))},$$

$$\frac{\mathcal{B}(B_s^0 \to D_s^-(\phi\pi^-)D_s^+(\pi^+\pi^+\pi^-))}{\mathcal{B}(B^0 \to D^- D_s^+(\pi^+\pi^+\pi^-))}.$$

Due to this setup, the $\mathcal{B}(B_s^0 \to D_s^- D_s^+)\mathcal{B}(B^0 \to D^- D_s^+)$ only depends on the ratio of the branching fractions $\mathcal{B}(D^- \to K^+\pi^-\pi^-)/\mathcal{B}(D_s^- \to \phi\pi^-)$. To calculate the branching fraction for the three D_s^- channels separately, we use the formula

$$\frac{f_s}{f_d}\frac{\mathcal{B}(B_s^0 \to D_s^- D_s^+)}{\mathcal{B}(B^0 \to D^- D_s^+)} = \frac{N(D_s^+ D_s^-)}{N(D^- D_s^-)} \cdot \frac{\epsilon(D^- D_s^-)}{\epsilon(D_s^+ D_s^-)} \cdot \frac{\mathcal{B}(D^- \to K^+\pi^-\pi^-)}{\mathcal{B}(D_s^+ \to \phi(K^+K^-)\pi^+)}.$$

We substitute the $N(D_s^+ D_s^-)$, $N(D^- D_s^-)$ with the yields from Table 6.1 and $\epsilon(D^- D_s^-)$, $\epsilon(D_s^+ D_s^-)$ with the efficiencies from Table 4.5. For our dataset we obtain

$$\frac{f_s}{f_d} \cdot \frac{\mathcal{B}(B_s^0 \to D_s^-(\phi\pi^-)D_s^+(\phi\pi^+))}{\mathcal{B}(B^0 \to D^- D_s^+(\phi\pi^+))} = 0.25^{+0.10}_{-0.08} \pm 0.03(\mathcal{B}),$$

$$\frac{f_s}{f_d} \cdot \frac{\mathcal{B}(B_s^0 \to D_s^-(\phi\pi^-)D_s^+(K^{*0}K^+))}{\mathcal{B}(B^0 \to D^- D_s^+(K^{*0}K^+))} = 0.39^{+0.23}_{-0.18} \pm 0.05(\mathcal{B}),$$

$$\frac{f_s}{f_d} \cdot \frac{\mathcal{B}(B_s^0 \to D_s^-(\phi\pi^-)D_s^+(\pi^+\pi^+\pi^-))}{\mathcal{B}(B^0 \to D^-D_s^+(\pi^+\pi^+\pi^-))} = 0.69^{+0.31}_{-0.26} \pm 0.09(\mathcal{B}).$$

where $(\mathcal{B})$ includes the uncertainty on the ratio of branching fractions $\mathcal{B}(D^- \to K^+\pi^-\pi^-)/\mathcal{B}(D_s^- \to \phi\pi^-)$. Using $f_s/f_d = 0.259 \pm 0.038$ [1], we calculate the ratio of branching fractions for the three different D_s^- decay channels separately:

$$\frac{\mathcal{B}(B_s^0 \to D_s^-(\phi\pi^-)D_s^+(\phi\pi^+))}{\mathcal{B}(B^0 \to D^-D_s^+(\phi\pi^+))} = 0.98^{+0.38}_{-0.32} \pm 0.14(f_s/f_d) \pm 0.13(\mathcal{B}),$$

$$\frac{\mathcal{B}(B_s^0 \to D_s^-(\phi\pi^-)D_s^+(K^{*0}K^+))}{\mathcal{B}(B^0 \to D^-D_s^+(K^{*0}K^+))} = 1.51^{+0.87}_{-0.70} \pm 0.22(f_s/f_d) \pm 0.20(\mathcal{B}),$$

$$\frac{\mathcal{B}(B_s^0 \to D_s^-(\phi\pi^-)D_s^+(\pi^+\pi^+\pi^-))}{\mathcal{B}(B^0 \to D^-D_s^+(\pi^+\pi^+\pi^-))} = 2.67^{+1.20}_{-0.99} \pm 0.39(f_s/f_d) \pm 0.36(\mathcal{B}).$$

The systematic uncertainties are discussed further in the next section.

In $B_s^0 \to D_s^-\pi^+\pi^+\pi^-$ decay mode, the D_s^- meson decays into $\phi\pi^-$, $K^{*0}K^-$ or $\pi^+\pi^-\pi^-$. We form $\mathcal{B}(B_s^0 \to D_s^-D_s^+)/\mathcal{B}(B_s^0 \to D_s^-\pi^+\pi^+\pi^-)$ ratios for the three different D_s^- modes so that only $\mathcal{B}(D_s^- \to \phi\pi^-)$ appears in the final answer and the other D_s^- branching fractions cancel in the ratio

$$\frac{\mathcal{B}(B_s^0 \to D_s^-(\phi\pi^-)D_s^+(\phi\pi^+))}{\mathcal{B}(B_s^0 \to D_s^-(\phi\pi^-)\pi^+\pi^+\pi^-)},$$

$$\frac{\mathcal{B}(B_s^0 \to D_s^-(\phi\pi^-)D_s^+(K^{*0}K^+))}{\mathcal{B}(B_s^0 \to D_s^-(K^{*0}K^-)\pi^+\pi^+\pi^-)},$$

$$\frac{\mathcal{B}(B_s^0 \to D_s^-(\phi\pi^-)D_s^+(\pi^+\pi^+\pi^-))}{\mathcal{B}(B_s^0 \to D_s^-(\pi^+\pi^-\pi^-)\pi^+\pi^+\pi^-)}.$$

Due to this setup the systematic uncertainty only depends on the uncertainty of the decay $D_s^- \to \phi\pi^-$. To calculate the branching fraction for the three D_s^- channels

separately, we use the formula

$$\frac{f_s}{f_d}\frac{\mathcal{B}(B_s^0 \to D_s^- D_s^+)}{\mathcal{B}(B_s^0 \to D_s^- \pi^+\pi^+\pi^-)} = \frac{N(D_s^+ D_s^-)}{N(D_s^- 3\pi)} \cdot \frac{\epsilon(D_s^- 3\pi)}{\epsilon(D_s^+ D_s^-)} \cdot \frac{1}{\mathcal{B}(D_s^+ \to \phi(K^+K^-)\pi^+)}.$$

We substitute the $N(D_s^+ D_s^-)$, $N(D_s^- 3\pi)$ with the yields from Table 6.1 and $\epsilon(D_s^- 3\pi)$, $\epsilon(D_s^+ D_s^-)$ with the efficiencies from Table 4.5. For our dataset we obtain:

$$\frac{\mathcal{B}(B_s^0 \to D_s^- D_s^+)}{\mathcal{B}(B_s^0 \to D_s^- \pi^+\pi^+\pi^-)} = 1.52^{+0.60\ +0.14}_{-0.51\ -0.14} \pm 0.20(\mathcal{B}),$$

$$\frac{\mathcal{B}(B_s^0 \to D_s^- D_s^+)}{\mathcal{B}(B_s^0 \to D_s^- \pi^+\pi^+\pi^-)} = 2.05^{+1.23\ +0.29}_{-1.00\ -0.35} \pm 0.27(\mathcal{B}),$$

$$\frac{\mathcal{B}(B_s^0 \to D_s^- D_s^+)}{\mathcal{B}(B_s^0 \to D_s^- \pi^+\pi^+\pi^-)} = 3.42^{+1.64\ +0.32}_{-1.39\ -0.38} \pm 0.44(\mathcal{B}).$$

The systematic uncertainties are discussed further in the next section.

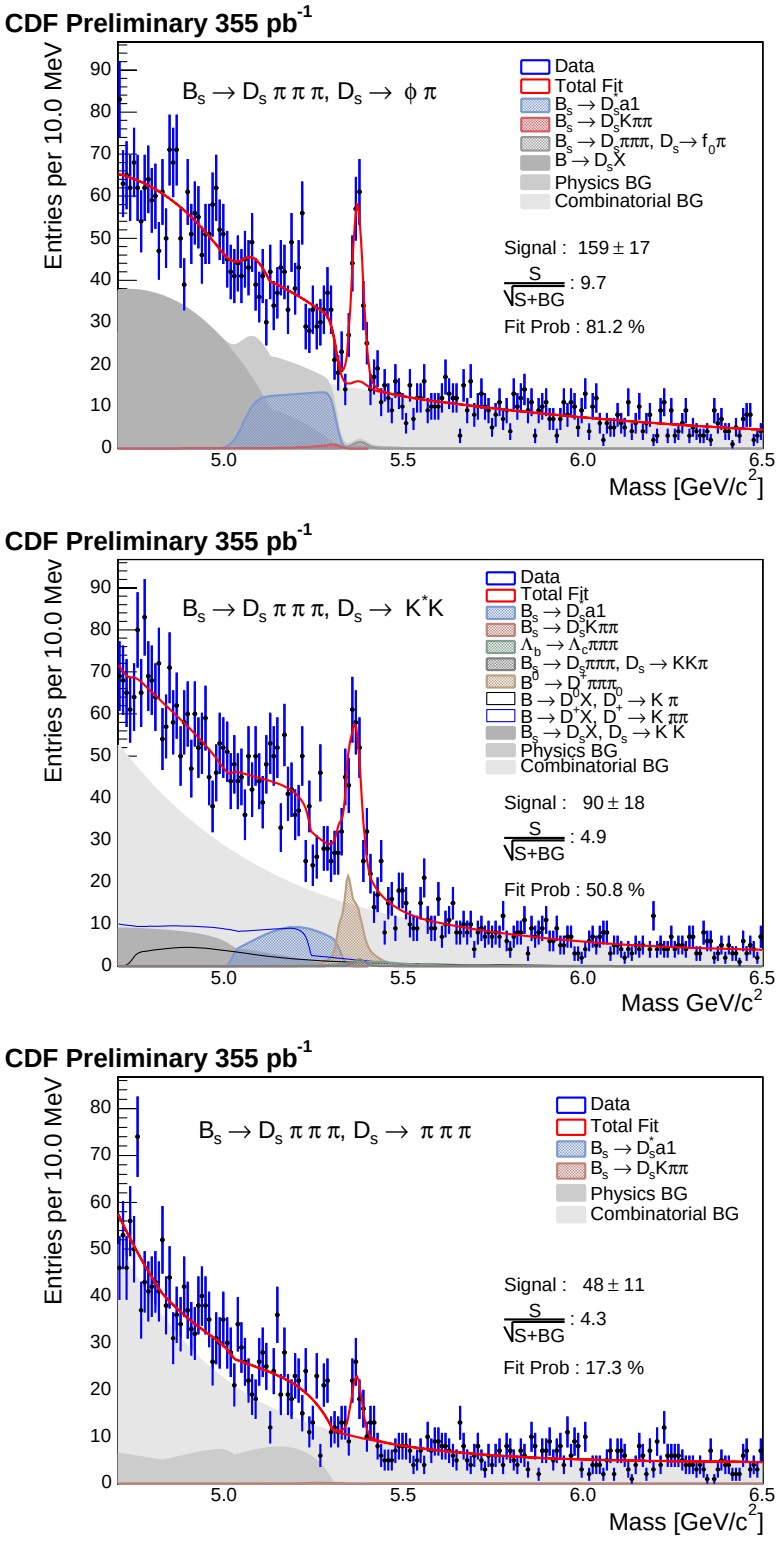

Figure 6-3: Reconstructed $B_s^0 \to D_s^- \pi^+ \pi^+ \pi^-$ mass distributions.

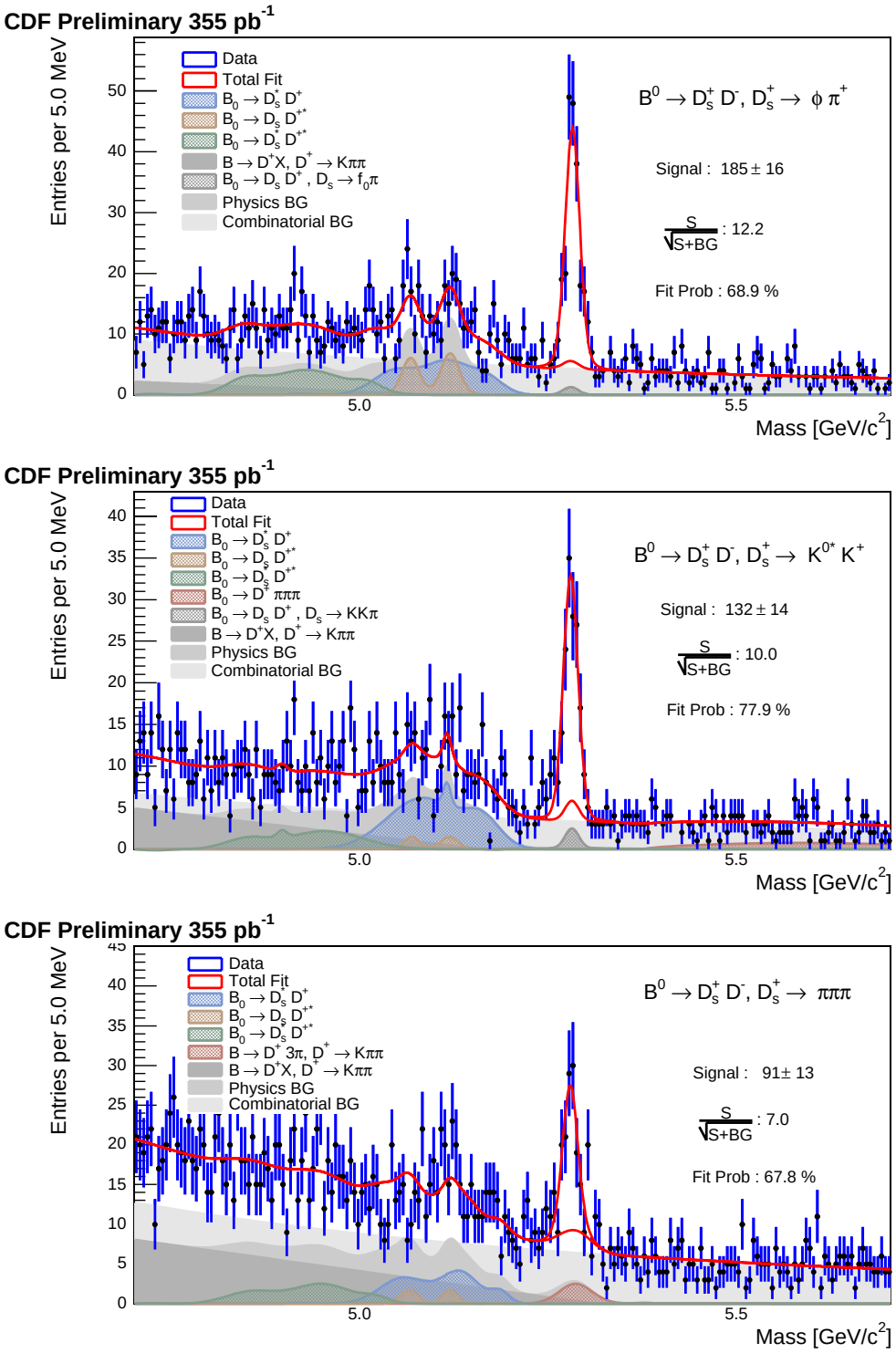

Figure 6-4: Reconstructed $B^0 \to D^- D_s^+$ mass distributions.

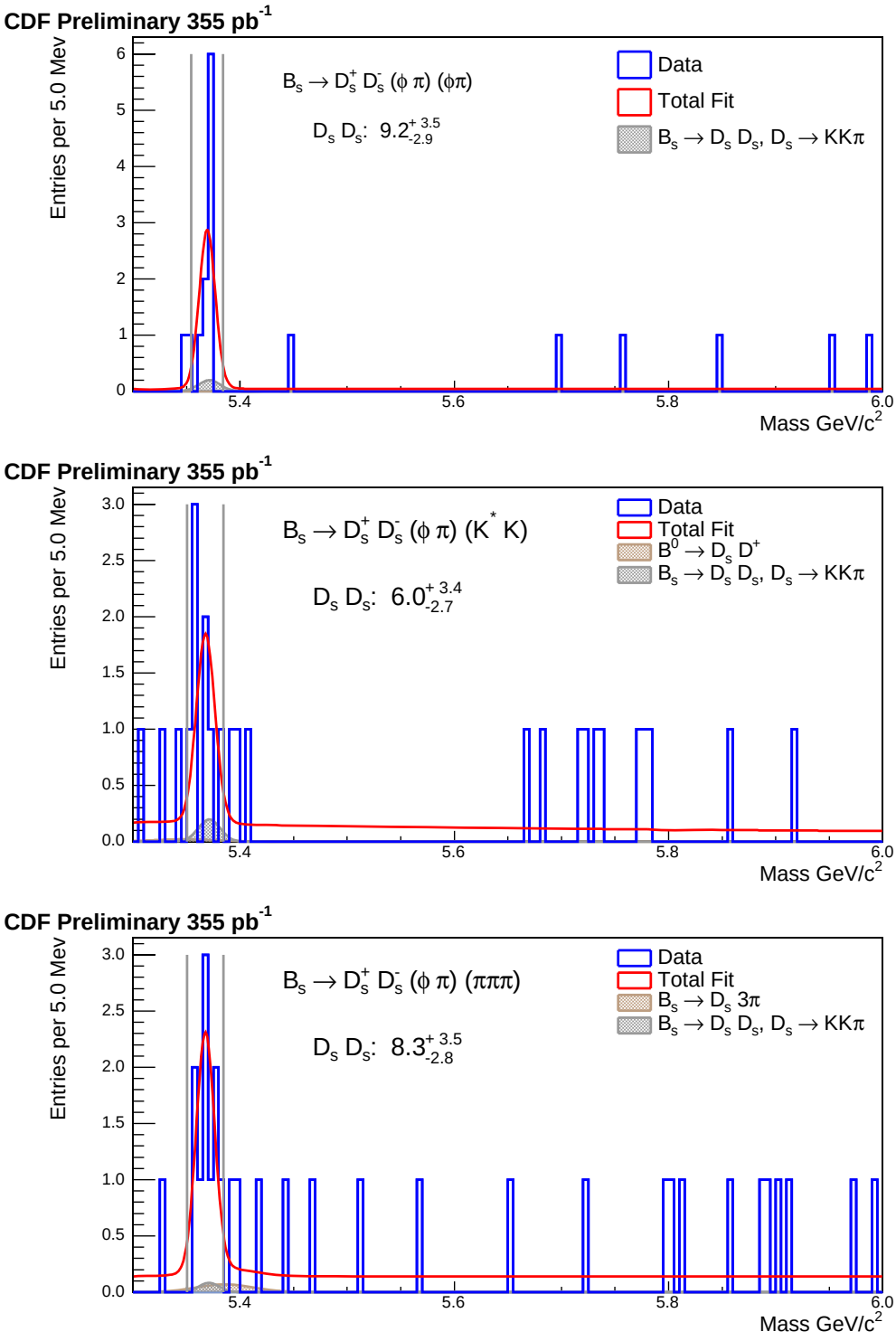

Figure 6-5: Reconstructed $B_s^0 \to D_s^- D_s^+$ mass distributions.

Chapter 7

Significance of $B_s^0 \to D_s^- D_s^+$ Mode Discovery

The significance of the observation of the $B_s^0 \to D_s^- D_s^+$ decay is obtained from the ratio of the likelihood fit to the data including signal and background model and the likelihood achieved by fitting the same data mass distribution with a background only model. Background is described with a constant function with one floating parameter. Signal is described with double Gaussian template with a common mean and only one normalization parameter floating. Using the likelihoods of the normalized fitting functions in mass interval $[5.3, 6.0]$ GeV/c^2 we introduce likelihood ratio

$$\Delta L = -2(ln(L_1) - ln(L_2)), \tag{7.1}$$

where:

L_1 - is the likelihood sum for the fit with the signal and the background model,

L_2 - is the likelihood sum for the fit with the background model only,

ΔL - is the likelihood ratio.

Likelihood ratio follows a χ^2 distribution with the number of degrees of freedom equal to the number of free parameters difference between the two fitting models. In our case, the model with the signal Gaussians has one additional free parameter: the floating normalization of the signal. If the most simple case for $B_s^0 \to$

$D_s^-(\phi\pi^-)D_s^+(\phi\pi^+)$ decay mode with no optimization bias taken into account, we find $\Delta L = 44.5$, which corresponds to 6.7σ standard deviation for a χ^2 distribution with one degree of freedom.

During the cut optimization we use the background from data to calculate the significance of the signal. Our choice of analysis cuts may bias background level toward lower values. To estimate the effect, we consider that choosing a value for one cut will on average lower the background by no more than one standard deviation of the background statistics in the fitting window. We count the number of background events in the mass interval $[5.4, 6.0]$ GeV/c^2 used by optimization procedure and evaluate the hypothetical unbiased number of background events by using the formula

$$N_{\text{biased}} = N_{\text{unbiased}} - \sqrt{6 \cdot N_{\text{unbiased}}}, \tag{7.2}$$

where

N_{biased} - number of background events in $[5.4, 6.0]$ GeV/c^2 interval with the bias introduced by optimization of 6 independent cuts. This is the actual number of the background events in the reconstructed mass distribution.

N_{unbiased} - number of background events in $[5.4, 6.0]$ GeV/c^2 interval without the bias. This is hypothetical number of background events in case when there is no optimization bias.

The biases due to the different cuts are considered independent and normal statistics is implied for the background events. Solving the above equation we get

$$N_{\text{unbiased}} = N_{\text{biased}} + 3 + \sqrt{6 \cdot N_{\text{biased}} + 9}. \tag{7.3}$$

There are 6 background events in $[5.4, 6.0]$ GeV/c^2 interval for $B_s^0 \to D_s^-(\phi\pi^-)D_s^+(\phi\pi^+)$ mode reconstructed mass distribution (Figure 6-5). From Eq. 7.3, we estimate the unbiased number of background events for the same mass interval to be smaller than 15.7 (Table 7.1). Implying a constant background hypothesis we estimate 18.3 events for wider $[5.3, 6.0]$ GeV/c^2 mass interval . We generate 200 pseudo-experiments based

on $B_s^0 \to D_s^-(\phi\pi^-)D_s^+(\phi\pi^+)$ mass distribution by randomly adding events following the constant mass distribution, requiring the total number of background events in $[5.3, 6.0]$ GeV/c^2 interval to have Poissonian distribution with the predetermined average of 18.3. We fit every histogram and integrate the signal yield exactly the same way we do it for the reconstructed data mass distribution.

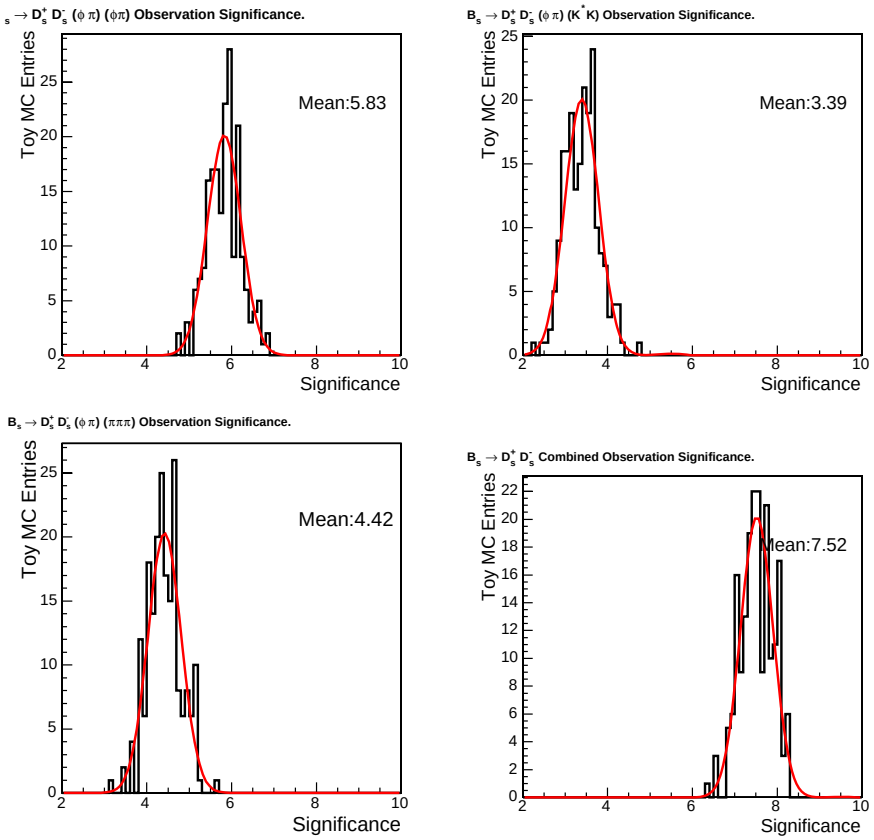

Figure 7-1: The outcome of the likelihood ratio method for 200 pseudo-experiments with boosted background: $B_s^0 \to D_s^-(\phi\pi^-)D_s^+(\phi\pi^+)$ - top left, $B_s^0 \to D_s^-(\phi\pi^-)D_s^+(K^{*0}K^+)$ -top right, $B_s^0 \to D_s^-(\phi\pi^-)D_s^+(\pi^+\pi^+\pi^-)$ bottom left, combined - bottom right.

We generate 200 pseudo experiments with inflated background and calculate the significance of the signal using the likelihood ratio method described above. The distribution of significances for $B_s^0 \to D_s^-(\phi\pi^-)D_s^+(\phi\pi^+)$ 200 pseudo-experiments, shown on Figure 7-1, has a mean of 5.8 standard deviations as opposed to 6.7 standard deviations from our previous estimate neglecting the bias. The results of the likelihood

ratio method applied to the mass distributions of the $B_s^0 \to D_s^-(\phi\pi^-)D_s^+(K^{*0}K^+)$ and the $B_s^0 \to D_s^-(\phi\pi^-)D_s^+(\pi^+\pi^+\pi^-)$ modes are shown on Figure 7-1 and summarized in Table 7.1.

To find the significance of the measurement for the three channels combined, we form a ratio of the product of three individual likelihoods for three mass distributions fitted with the background models, and the product of three likelihoods for the same mass distributions fitted with models including the background and the signal. The ratio of the likelihood products should follow the χ^2 distribution with three degrees of freedom corresponding to three floating signal normalizations in the three individual fits. For the likelihood ratio calculated for each of the 200 pseudo-experiments, we determine the corresponding probability based on a χ^2 distribution with three degrees of freedom, and convert it to the measure of standard deviations. The distribution of calculated significances for 200 pseudo-experiments is shown on Figure 7-1. The mean of the Gaussian fit (7.5 standard deviations) is used as a significance of the combined measurements.

To estimate the systematic bias due to the optimization, we use the same set of 200 pseudo-experiments for each mode. We fit every mass distribution and integrate the signal yield exactly the same way we do it for data mass distributions.

$B_s^0 \to D_s^- D_s^+$	$(\phi\pi^+)(\phi\pi^-)$	$(\phi\pi^+)(K^{*0}K^-)$	$(\phi\pi^+)(\pi^+\pi^-\pi^-)$
N_{biased} in $[5.4, 6.0]$ GeV	6	13	18
N_{unbiased}	15.7	25.3	31.8
Signal	9.2	6.0	8.3
Significance (σ)	5.8	3.4	4.4
Optimization Bias [%]	-5%	-13%	-4%

Table 7.1: The significance of the discovery of $B_s^0 \to D_s^- D_s^+$ mode and the bias due to the optimization procedure.

We introduce the optimization bias for every mode as a difference between the average of the signal yields for 200 pseudo-experiments and the actual signal yield from data. The difference between an "unbiased" signal yield constructed this way and the real signal yield is negative for all three modes. We normalize the bias to the signal yield and add it to the systematic uncertainties described in the next chapter.

Chapter 8

Systematic Uncertainties

In this analysis we measure the ratios of branching fractions. Most of the theoretical and instrumental systematic uncertainties are canceled in the ratio. The remaining sources of systematic uncertainties are studied to make sure that they are negligible compared to the statistical uncertainty. There are several major sources of systematic uncertainty

- Incomplete or incorrect simulation of the detector and trigger response,
- the limited knowledge of the decay models and branching fractions,
- incomplete or incorrect fit model.

8.1 Trigger Systematics

There are several sources of systematic uncertainties related to the CDF trigger features poorly reproduced by Monte Carlo simulations. The largest contributions are described below:

XFT efficiency for kaons relative to pions. XFT system has different efficiency for tracks generated by kaons and pions. A detailed study of the XFT efficiency [49] showed that different XFT efficiency of pions and kaons due to the different ionization patterns in the COT is not reproduced by Monte Carlo simulation. A study of this

effect in data using a sample of $D^- \to K^+\pi^-\pi^-$ decays shows a 6% inefficiency of kaons relative to pions. A 6% inefficiency for every kaon track to make a trigger track introduced into the $B^0 \to D^-\pi^+\pi^+\pi^-$ and $B_s^0 \to D_s^-\pi^+\pi^+\pi^-$ Monte Carlo simulation changes the ratio of efficiencies by 0.2%. No systematic unctertainty is assigned to the effect.

Trigger efficiency dependence on run number. The trigger setup changes with time and leads to the change in the reconstruction efficiency. To study the effect we calculate the ratio of Monte Carlo efficiencies for $B^0 \to D^-\pi^+\pi^+\pi^-$ and $B_s^0 \to D_s^-\pi^+\pi^+\pi^-$ modes for `B_CHARM` and `B_CHARM_LOWPT` datasets separately in four representative run ranges

1. 138809 - 164304 from the beginning of the data set to the beginning of SVT 4/5 configuration,
2. 164305 - 168889 from the beginning of SVT 4/5 configuration to the 2003 shutdown,
3. 168889 - 179056 runs up to bad COT period,
4. 184208 - 186598 post COT recovery up to the end of the dataset.

We measure the ratio of Monte Carlo reconstruction efficiencies for $B^0 \to D^-\pi^+\pi^+\pi^-$ and $B_s^0 \to D_s^-\pi^+\pi^+\pi^-$ samples in 4 run ranges separately for `B_CHARM` and `B_CHARM_LOWPT` trigger data (Figure 8-1). The ratio of efficiencies for the last run range is two standard deviations lower than the average. We estimate the potential systematic uncertainty by reweighting this point to the average value as shown in Figure 8-1 and measuring the change in the efficiency ratio for the total sample. A systematic uncertainty of $\pm 1.0\%$ is assigned for this effect.

SVT $\chi^2_{R\phi}$ Cut. When we confirm the online trigger pair by matching offline track to SVT tracks, we require $\chi^2_{R\phi} < 25$ for the goodness of the SVT two-track vertex fit. The cut has been tightened to $\chi^2_{R\phi} < 15$ for a significant fraction of the dataset (Table 8.1).

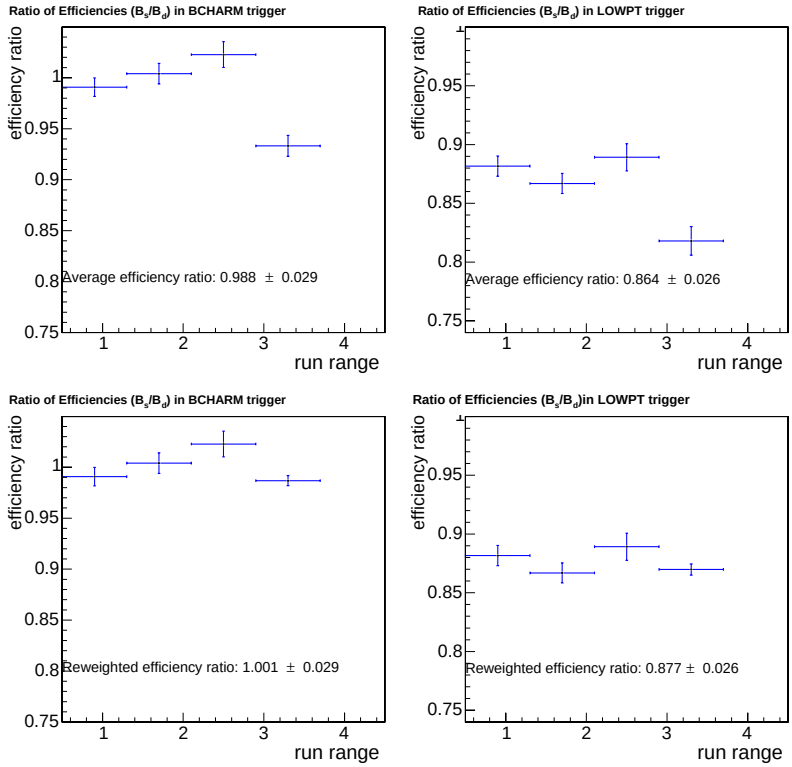

Figure 8-1: Ratio of efficiencies of $B^0 \to D^-\pi^+\pi^+\pi^-$ and $B_s^0 \to D_s^-\pi^+\pi^+\pi^-$ for four representative run ranges `B_CHARM` (left) and `B_CHARM_LOWPT` (right) raw (top) and rescaled (bottom).

Run Range	$\chi^2_{R\phi}$ Cut Value	Luminosity
138809 - 178757	$\chi^2_{R\phi} < 25$	228 pb^{-1}
178844 - 186598	$\chi^2_{R\phi} < 15$	127 pb^{-1}

Table 8.1: $\chi^2_{R\phi}$ cut on SVT two-track vertex fit for different run ranges.

To estimate the uncertainty due to the effect for $B^0 \to D^-\pi^+\pi^+\pi^-$ and $B^0_s \to D^-_s(\pi^+\pi^-\pi^-)\pi^+\pi^+\pi^-$ modes, we generate two sets of Monte Carlo simulations with different trigger level cuts on $\chi^2_{R\phi}$. We measure the difference in ratio of efficiencies for these two samples to be less than 1% and assign the systematic uncertainty of 1.0% due to this effect for all the modes.

8.2 B Meson Kinematics

We use the world average measurements [50] of the B meson lifetimes for Monte Carlo simulations. Incorrect lifetime may change trigger and reconstruction efficiency, as the two-track trigger and several selection requirements are based on track and secondary vertex displacement.

Meson	Lifetime	uncertainty
B^0_s	1.466 ± 0.059 ps	$\pm 2.0\%$
B^0	1.530 ± 0.009 ps	$\pm 0.4\%$

Table 8.2: B meson lifetimes [1] and estimated systematic uncertainties.

We estimate the effect by generating two Monte Carlo samples with B meson lifetimes varied the uncertainties of the world average measurement, as listed in Table 8.2. We assign the systematic uncertainty of $\pm 2.0\%$ measuring the change in the ratio of efficiencies for two Monte Carlo samples.

The Monte Carlo B meson p_T spectrum based on NLO calculations does not agree with the one, measured in inclusive J/ψ channel [51]. To estimate the systematic uncertainty due to the discrepancy, we study the change in signal efficiency produced by changes in Monte Carlo simulations

- B meson p_T spectrum measured by Reference [51] is introduced,
- selection requirement $\eta < 1.3$ of the generated b-quarks is added,
- peterson fragmentation is turned off.

Observing the change in efficiency, we assign a $\pm 3.0\%$ systematic uncertainty due to the uncertainties of the B_s^0 meson p_T spectrum.

8.3 The Resonant Structure of the 3π

Due to the limited knowledge of the 3π resonant structure, Monte Carlo simulations do not reproduce the 3π mass distribution. In our analysis we reduce the disagreement by correcting the resonant composition of the 3π in Monte Carlo decay table for $B^0_{(s)} \to D^-_{(s)}\pi^+\pi^+\pi^-$ modes. The rest of the disagreement is taken into account as systematic uncertainty.

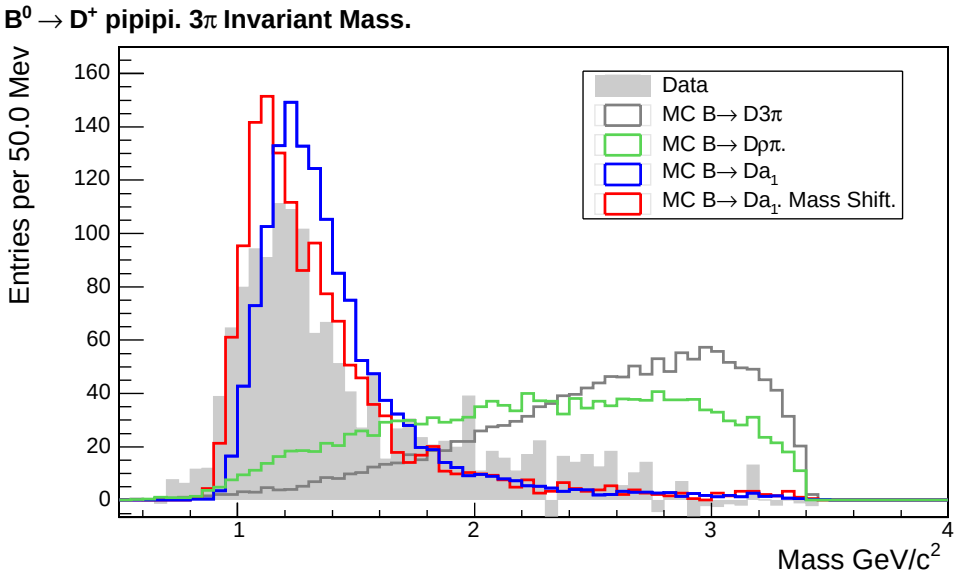

Figure 8-2: Comparing Monte Carlo 3π invariant mass spectrum for different signal components with data.

The $B^0 \to D^-\pi^+\pi^+\pi^-$ final state consists of three main components with distinguishable 3π mass spectra

- $B^0 \to D^- a_1^+$, with $a_1^+ \to \pi^+\pi^+\pi^-$,
- $B^0 \to D^- \rho^0 \pi^+$, with $\rho^0 \to \pi^+\pi^-$,
- $B^0 \to D^- \pi^+\pi^+\pi^-$ non-resonant.

Figure 8-2 shows the comparison of the 3π mass spectra of the three components compared to the sideband subtracted spectrum from data. To make the comparison, we correct the mass of the sideband candidates to compensate for the mass difference between the signal and the sideband.

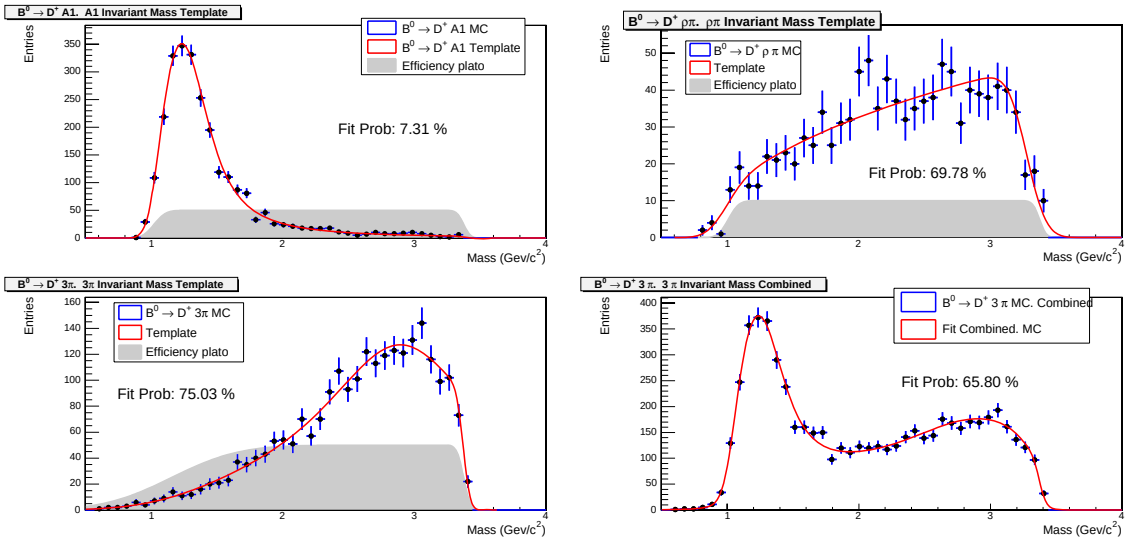

Figure 8-3: 3π mass templates. $B^0 \to D^- a_1^+$ and $B^0 \to D^- \pi^+\pi^+\pi^-$ (left), $B^0 \to D^- \rho^0 \pi^+$, and tree channels mixed together by a default Monte Carlo decay table (right).

We create the templates by fitting the 3π mass spectra for each of the three component separately. Figure 8-3 shows $B^0 \to D^- a_1^+$, $B^0 \to D^- \rho^0 \pi^+$, and $B^0 \to D^- \pi^+\pi^+\pi^-$ templates, fitted with a Breit-Wigner function smeared with a Gaussian, and multiplied by a plateau formed by two error function (Eq.5.2), describing the kinematic cutoffs at high and low masses.

We fit the Monte Carlo 3π mass distribution with three templates with floating normalization, to ensure that the fit reproduces the ratios of the resonant components from Monte Carlo simulations (Figure 8-4 on the left). The corresponding fit for our data (Figure 8-4 on the right), with floating mass and width of the a_1^+ template, shows

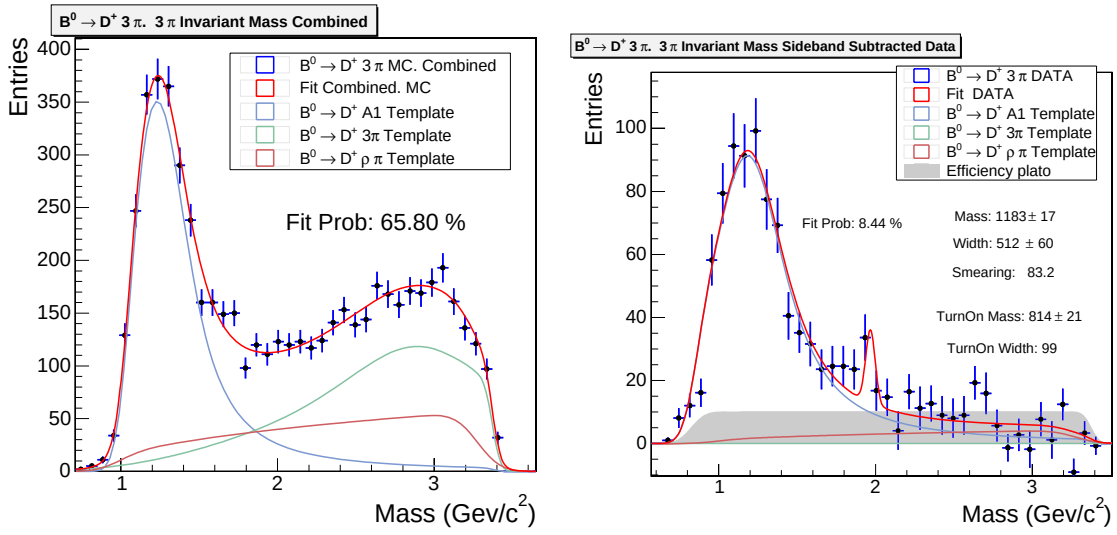

Figure 8-4: Fit for Monte Carlo $B^0 \to D^-\pi^+\pi^+\pi^-$ 3π mass spectrum with subresonant templates (left) and the same fit for data (right).

that the 3π spectrum in data is dominated by the a_1^+ resonance in agreement with recent measurements [43]. Following the results of our data fit, we achieve better agreement of data and Monte Carlo (Figure 8-5) by reducing the relative contribution of $\rho^0\pi^+$ and $\pi^+\pi^+\pi^-$ with respect to a^+ in the decay table used for Monte Carlo simulations (Table A.9). The remaining 3π spectrum disagreement between data and Monte Carlo simulations is taken into account as a systematic uncertainty.

Decay	MC yield.	Efficiency
$B^0 \to D^- a_1^+$	11274 ± 138	0.262 ± 0.003
$B^0 \to D^- \rho^0 \pi$	11932 ± 142	0.277 ± 0.003
$B^0 \to D^- 3\pi$	13181 ± 148	0.307 ± 0.003
Admixture	11570 ± 138	0.269 ± 0.003
Admixture/$(D^- a_1^+)$		1.026 ± 0.015

Table 8.3: Efficiency study for resonances in the 3π mass spectrum. Admixture of the resonances is specified by the tuned decay table (Table A.9).

The position and the shape of a_1^+ mass peak is not reproduced well by Monte Carlo simulations. To estimate the systematic uncertainty due to this effect, we generate Monte Carlo sample with a_1^+ mass shifted by 80 MeV/c^2 toward better agreement with data (Figure 8-2). We observe no significant change in efficiency. To study the

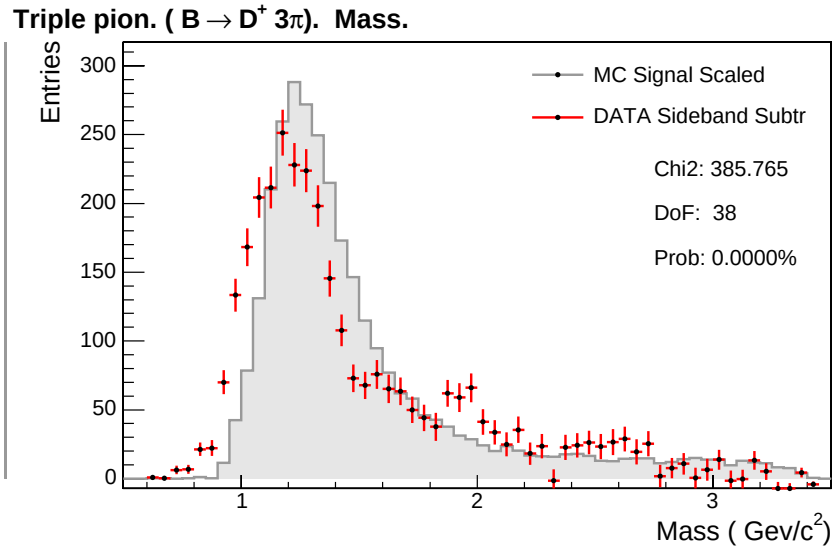

Figure 8-5: Comparison of the 3π mass spectrum between Monte Carlo simulation and data.

effect of the a_1^+ decay model, we generate a Monte Carlo sample with the a_1^+ decaying according to the phase space three body decay kinematic model, and a similar sample with the a_1^+ decaying according a p-wave model. The latter is dominating, according to the most recent measurements [1]. We observe no significant change in efficiency. As a cross-check, we compare the data 3π mass spectra between the decays $B^0 \to D^-\pi^+\pi^+\pi^-$ and $B_s^0 \to D_s^-\pi^+\pi^+\pi^-$ (Figure 8-6). The two distributions agree within the statistics.

When fitting the 3π mass spectrum with a_1^+, $\rho^0\pi^+$, and non-resonant $\pi^+\pi^+\pi^-$ templates we find that we do not have sufficient data to observe the $\rho^0\pi^+$ and $\pi^+\pi^+\pi^-$ contributions. The analysis efficiencies for three separate components and the admixture, specified by tuned decay table (Table A.9) are summarized in Table 8.3. We find the ratio of the efficiencies of pure $B^0 \to D^-a_1^+$ mode, and the admixture to be 1.026 ± 0.015 (Table A.9). Based on this ratio, we assign a $\pm 2.5\%$ systematic uncertainty due to the 3π resonant structure.

Similarly, the subresonant structure of the $D_s^- \to \pi^+\pi^-\pi^-$ decay is not well known. We estimate the systematic uncertainty due to the effect by comparing the efficiencies

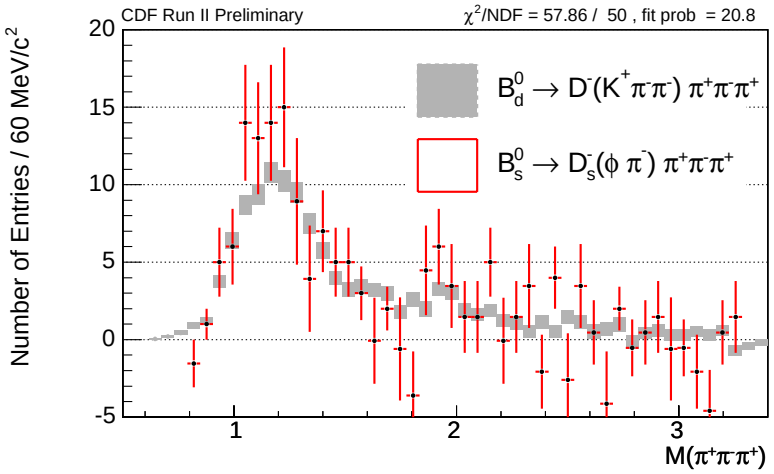

Figure 8-6: 3π mass of $B^0 \to D^-\pi^+\pi^+\pi^-$ and $B^0_s \to D^-_s\pi^+\pi^+\pi^-$.

of two Monte Carlo samples: one, implementing the simple phase space three body decay kinematic model, and the other, using the admixture of the resonances according to the best knowledge of the $D^-_s \to \pi^+\pi^-\pi^-$ decay structure [1]. The relevant fragments of the decay files are listed in the Table A.10.

Decay	Generated	MC yield.	Efficiency
$B^0 \to D^-D^+_s(\pi^+\pi^+\pi^-)$	8.6	3217 ± 58	0.374 ± 0.007
$B^0 \to D^-D^+_s$(admixture)	43.1	16515 ± 168	0.383 ± 0.004
admixture/$(\pi^+\pi^+\pi^-)$			1.024 ± 0.02

Table 8.4: Efficiency study for different D^-_s decay models. Phase space three body decay kinematic model and model using the best knowledge of the $D^-_s \to \pi^+\pi^-\pi^-$ decay structure [1].

Using the results of the comparison listed in the table 8.4, we assign a 2.5% systematic uncertainty due to the resonannt structure of the $D^-_s \to \pi^+\pi^-\pi^-$ decay. The uncertainty is assigned to the B meson decay modes involving $D^-_s \to \pi^+\pi^-\pi^-$ decay: $B^0_s \to D^-_s(\pi^+\pi^-\pi^-)\pi^+\pi^+\pi^-$, $B^0 \to D^-D^+_s(\pi^+\pi^+\pi^-)$, and $B^0_s \to D^-_s(\phi\pi^-)D^+_s(\pi^+\pi^+\pi^-)$.

8.4 D^- Veto Study

The reconstructed mass distribution of the $B_s^0 \to D_s^-(K^{*0}K^-)\pi^+\pi^+\pi^-$ decay mode has a large contribution from misreconstructed $B^0 \to D^-\pi^+\pi^+\pi^-$ mode under the signal peak. A similar feature is also present in the reconstruction of the $B_s^0 \to D_s^-(\phi\pi^-)D_s^+(K^{*0}K^+)$decay mode, with misreconstructed $B^0 \to D^-D_s^+(\phi\pi^+)$ reflecting under the signal peak. In both cases, one of the pions from $D^- \to K^+\pi^-\pi^-$ decay is assigned a kaon mass and as a result the B^0 candidates are shifted to the right in the B_s^0 mass region. To get rid of the unwanted reflection we apply D^- veto to our $B_s^0 \to D_s^-(K^{*0}K^-)\pi^+\pi^+\pi^-$ reconstruction.

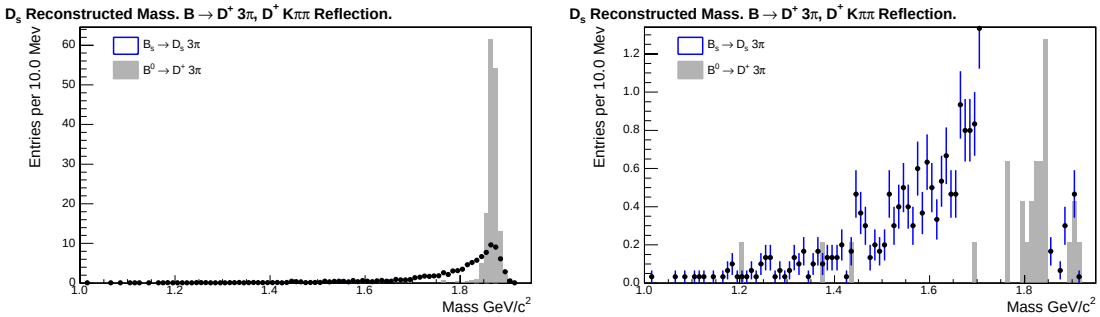

Figure 8-7: Reconstructed mass of the $D^- \to K^+\pi^-\pi^-$ decay for $B^0 \to D^-\pi^+\pi^+\pi^-$ and $B_s^0 \to D_s^-(K^{*0}K^-)\pi^+\pi^+\pi^-$ Monte Carlo simulations, scaled to the size of the data sample. Without D^- veto (left) and with veto applied (right). Note the scale difference.

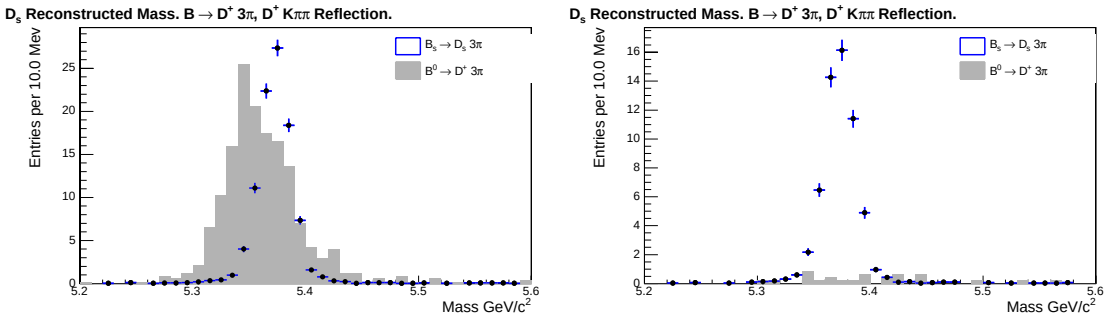

Figure 8-8: Reconstructed mass of the B meson for $B^0 \to D^-\pi^+\pi^+\pi^-$ and $B_s^0 \to D_s^-(K^{*0}K^-)\pi^+\pi^+\pi^-$ Monte Carlo simulations, scaled to the size of the data sample. Without D^- veto (left) and with veto applied (right).

Veto procedure calculates the mass of the reconstructed $D_s^- \to K^{*0}K^-$ candidate, substituting one kaon with a pion. It rejects candidates in the ± 24 MeV/c^2 region around the D^- meson world average mass [1]. The effect of the veto on the D^- meson reconstructed mass distribution for $B_s^0 \to D_s^-(K^{*0}K^-)\pi^+\pi^+\pi^-$ and $B^0 \to D^-\pi^+\pi^+\pi^-$ modes is shown on Figure 8-7. The effect of the veto on the B_s^0 meson reconstructed mass distribution for the same modes is shown on Figure 8-8. The Monte Caro studies show that the veto eliminates more than 95% of the misreconstructed $B^0 \to D^-\pi^+\pi^+\pi^-$ with a loss of approximately 40% of B_s^0 signal. Similar results are observed in data (Table 8.5).

	no D^- Veto	with D^- veto	loss
$B_s^0 \to D_s^-(K^{*0}K^-)\pi^+\pi^+\pi^-$ data	91 ± 17	50 ± 11	$-44\% \pm 20\%$
$B_s^0 \to D_s^-(K^{*0}K^-)\pi^+\pi^+\pi^-$ MC	2708 ± 55	1653 ± 40	$-39\% \pm 3\%$

Table 8.5: $B_s^0 \to D_s^-(K^{*0}K^-)\pi^+\pi^+\pi^-$ signal yield loss due to D^- veto.

The fits of reconstructed data distributions for $B_s^0 \to D_s^-(K^{*0}K^-)\pi^+\pi^+\pi^-$ with and without D^- veto are shown on Figure 8-9. The fit with D^- veto uses an individually constructed set of templates not described here. D^- veto is not used for $B_s^0 \to D_s^-(K^{*0}K^-)\pi^+\pi^+\pi^-$ mode because it does not improve the significance of the signal with high combinatorial background. The D^- veto is used for $B_s^0 \to D_s^-(\phi\pi^-)D_s^+(K^{*0}K^+)$ mode with smaller statistics and lower combinatorial background.

8.5 Systematic Uncertainty from the Fit Model

The major source of fit systematic uncertainty is incomplete or incorrect fitting model. The quality of the fitting model is limited by the knowledge of the branching fractions and the quality of the Monte Carlo simulations. There are also minor sources of fit systematic uncertainty related to technical aspects of the fit. For example, every fit of data mass distribution contains a number of fixed parameters affecting the measured yield. Some of the common fixed features also include the binning of the histogram,

the width of the fitted mass interval, the fixed parameters of the templates, etc. For every mode, we investigate the potential sources of the fit systematic uncertainty by varying the parameters or normalization of the fixed features and observing the change in the signal yield. For example, when fitting $B_s^0 \to D_s^-(\pi^+\pi^-\pi^-)\pi^+\pi^+\pi^-$, $B^0 \to D^- D_s^+$, and $B_s^0 \to D_s^- D_s^+$ modes, we fix the width of the signal template to the value obtained from Monte Carlo simulation and apply the width correction described in Section 5.3. We estimate the fit systematic uncertainty by varying the fixed signal width within one standard deviation of the measured uncertainty of width correction.

One of the possible sources of the systematic uncertainty is that the signals of $B_{(s)}^0 \to D_{(s)}^-\pi^+\pi^+\pi^-$ decay modes have longer tails compared to the signals of double-charm modes. The effect is taken into account by integrating the yield in the mass interval containing 95.45% of the signal or two standard deviations of the *effective width*. No systematic uncertainty is assigned to the effect.

8.5.1 $B_{(s)}^0 \to D_{(s)}^-\pi^+\pi^+\pi^-$ Fit Systematic Uncertainty

Although the continuum physics background does not contribute directly to the signal region, the shape of the template, depending on branching fractions of various B decays, indirectly affect the signal yields. To estimate the systematic uncertainty due to the semi-generic background template for $B^0 \to D^-\pi^+\pi^+\pi^-$ mode reconstruction, we change the normalization of the template within one standard deviation of the fitted value.

The branching fractions for most of the B_s^0 decays have not been measured, but have rather been extrapolated from the corresponding B^0 branching fractions which are relatively well known. To estimate the systematic uncertainty due to the limited knowledge of the the B_s^0 branching fractions, we measure the effect of the different components of B_s^0 semi-generic physics background. We divide the semi-generic template into three components: $B_s^0 \to D_s^- X$, with signal modes being subtracted, $B_s^0 \to D_s^{*-} X$, with $B_{(s)}^0 \to D_{(s)}^{*+}$ modes being subtracted, and the rest of the B hadron decays.

We fit the $B_s^0 \to D_s^-(\phi\pi^-)\pi^+\pi^+\pi^-$ mass distribution, dropping one of the three

Varied Parameter	Width	Cabibbo	$B^0 \to D^- X$	$B_s^0 \to D_s^- X$
$B^0 \to D^- \pi^+ \pi^+ \pi^-$		0.5%	0.6%	0.3%
$B_s^0 \to D_s^- (\phi\pi^-)\pi^+\pi^+\pi^-$	$\pm$1.3%	0.9%		$\pm$3.0% $\pm$1.9%[1]
$B_s^0 \to D_s^- (K^{*0}K^-)\pi^+\pi^+\pi^-$	$\pm$2.2%		$\pm$3.3% $\pm$7.8%[2]	$\pm$3.0%
$B_s^0 \to D_s^- (\pi^+\pi^-\pi^-)\pi^+\pi^+\pi^-$	$\pm$2.0%			$\pm$3.0%

Table 8.6: Fit systematic uncertainties for $B_s^0 \to D_s^- \pi^+\pi^+\pi^-$decay modes. Systematic uncertainty [1] is due to the $D_s^- \to f^0\pi^-$, with $f^0 \to K^+K^-$, and [2] is due to the normalization of the $B^0 \to D^-\pi^+\pi^+\pi^-$ reflection.

components using the variation of the signal yield to estimate the systematic uncertainty due to the effect. We assign the same $\pm$3% systematic uncertainty to three $B_s^0 \to D_s^-(\pi^+\pi^-\pi^-)\pi^+\pi^+\pi^-$ modes because the statistics for $B_s^0 \to D_s^-(K^{*0}K^-)\pi^+\pi^+\pi^-$ and $B_s^0 \to D_s^-(\pi^+\pi^-\pi^-)\pi^+\pi^+\pi^-$ decay modes is limited to make a significant study.

For small physics backgrounds with fixed normalizations such as the B meson Cabibbo suppressed decays, Λ_b decays, we change the normalization of the templates in question by $\pm$50%. The systematic uncertainties due to the fit model for the $B_{(s)}^0 \to D_{(s)}^- \pi^+\pi^+\pi^-$ modes, are summarized in Table 8.6.

8.5.2 $B_{(s)}^0 \to D_{(s)}^- D_s^+$ Fit Systematic Uncertainty

The fitting functions of the double charm modes contain many reflection templates with fixed normalization. The branching fractions of the decay modes, corresponding to these templates are not well known and are considered as a source of systematic uncertainty. To estimate the effect, we measure the change in the signal yield while varying the template normalization by one standard deviation from calculated value. The estimated systematic uncertainties due to the normalizations of the templates are summarized in Table 8.7 and the sources of the uncertainties are discussed below.

The $B^0 \to D^- D_s^+(\phi\pi^+)$ mode has a (3.5$\pm$2)% contribution from $D_s^- \to f_0\pi^-$, with $f^0 \to K^+K^-$ under the signal, where the uncertainty is coming from the branching fraction [1]. The width of the f_0 resonance is estimated to be within a mass interval of $[40, 100]$ MeV/c^2 [1]. To estimate the uncertainty due to the effect, we generate

Mode	$D_s^- \to f_0\pi$	$D_s^- \to K^+K^-\pi^-$	$B^0 \to D^-\pi^+\pi^+\pi^-$
$B^0 \to D_s^- D^-(\phi\pi^-)$	$\pm 1.6\%$	$\pm 0.4\%$	
$B^0 \to D_s^- D^-(K^{*0}K^-)$		$\pm 3.9\%$	
$B^0 \to D_s^- D^-(\pi^+\pi^-\pi^-)$		$\pm 0.1\%$	$\pm 8.3\%$
$D_s^- D_s^-(\phi\pi^-)$		$\pm 4.3\%$	
$D_s^- D_s^-(K^{*0}K^-)$		$\pm 6.7\%$	
$D_s^- D_s^-(\pi^+\pi^-\pi^-)$		$\pm 1.2\%$	$\pm 2.4\%$

Table 8.7: Fit systematic uncertainties for $B_s^0 \to D_s^- D_s^+$ decay modes.

two Monte Carlo samples with f_0 width 50 MeV/c^2 and 100 MeV/c^2. We find the change in signal yield to be negligible compared to the $\pm 1.6\%$ uncertainty due to the branching fraction $\mathcal{B}(D_s^- \to f_0\pi^-)$.

The $B^0 \to D^- D_s^+(K^{*0}K^+)$ mode has a $(10 \pm 5)\%$ contribution from the non-resonant $D_s^- \to K^+K^-\pi^-$ under the signal. We find a systematic uncertainty, originating from the branching fraction $\mathcal{B}(D_s^- \to K^+K^-\pi^-)$ [1] to be $\pm 4\%$.

The $B^0 \to D^- D_s^+(\pi^+\pi^+\pi^-)$ mode has a strong $B^0 \to D^-\pi^+\pi^+\pi^-$ reflection under the signal. The size of the reflection is fixed by using the observed $B^0 \to D^-\pi^+\pi^+\pi^-$ yield. The unknown subresonance content of the 3π system, discussed in Section 8.3, is the source of uncertainty due to the different reconstruction efficiencies for a_1^+ and $\rho^0\pi^+$ components. By using Monte Carlo simulation, we measure the difference in the reconstruction efficiency for a clean $B^0 \to D^- a_1^+$ sample and for the weighted admixture of a_1^+, $\rho^0\pi^+$, and $\pi^+\pi^+\pi^-$ to be less than 20%. We estimate the systematic uncertainty due to the effect by varying the normalization of the $B^0 \to D^-\pi^+\pi^+\pi^-$ reflection by $\pm 20\%$. Based on the observed change in $B^0 \to D^- D_s^+(\pi^+\pi^+\pi^-)$ yield we assign a systematic uncertainty of $\pm 8.3\%$.

The $B_s^0 \to D_s^-(\phi\pi^-)D_s^+(K^{*0}K^+)$ mode has a contribution from the misreconstructed $B^0 \to D^- D_s^+(\phi\pi^+)$ mode under the signal. The $D^- \to K^+\pi^-\pi^-$ veto, discussed in Section 8.4, reduces the reflection by 95%. The normalization of the $B^0 \to D^- D_s^+(\phi\pi^+)$ reflection template is calculated based on the observed yield of the reflecting mode, as described in Section 5.2.3. The systematic uncertainty from the template normalization ($\pm 1\%$) is due to the statistical uncertainty of the fit of

the data (Figure 5-4).

The $B_s^0 \to D_s^-(\phi\pi^-)D_s^+(\pi^+\pi^+\pi^-)$ mode has a contribution from the misreconstructed $B_s^0 \to D_s^-(\pi^+\pi^-\pi^-)\pi^+\pi^+\pi^-$ mode under the signal. The normalization of the $B_s^0 \to D_s^-(\pi^+\pi^-\pi^-)\pi^+\pi^+\pi^-$ reflection template is calculated based on the observed yield of reflecting mode, as described in Section 5.2.3. The systematic uncertainty from the template normalization ($\pm 2.4\%$) is due to the statistical uncertainty of the fit of the data (Figure 5-3).

All $B_s^0 \to D_s^- D_s^+$ modes have contributions from the non-resonant $D_s^- \to K^+K^-\pi^-$ mode under the signal. The systematic uncertainty of the normalization of the $B_s^0 \to D_s^-(K^+K^-\pi^-)D_s^+$ template is due to the uncertainty of the $\mathcal{B}(D_s^- \to K^+K^-\pi^-)$ branching fraction. For $D_s^- \to \phi\pi^-$, $D_s^- \to K^{*0}K^-$, and $D_s^- \to \pi^+\pi^-\pi^-$, we estimate the uncertainty due to the effect as $\pm 4.3\%$, $\pm 6.7\%$, and $\pm 1.2\%$, correspondingly.

For double charm modes we fix the widths of the signals to the values, obtained from the Monte Carlo simulations and apply the width correction described in Section 5.3. We estimate the fit systematic uncertainty by varying the fixed signal width within one standard deviation of the measured uncertainty of width correction.

The fitted mass value of the $B^0 \to D^- D_s^+$ mode is located 2.7 ± 1.0 MeV/c^2 away from the world average value (Table 5.2). The masses of the $B_s^0 \to D_s^- D_s^+$ signal templates are fixed to the B_s^0 world average mass 5367.5 ± 1.8 [1]. To estimate the systematic uncertainty due to the mass of the signal, we fit $B_{(s)}^0 \to D_{(s)}^- D_s^+$ data distributions with the mass of the signal template varied within ± 3 MeV/c^2. The systematic uncertainties due to the mass and width parameters of the signal templates for $B_{(s)}^0 \to D_{(s)}^- D_s^+$ modes are summarized in Table 8.5.2.

The systematic uncertainties due to the fit model for the $B_{(s)}^0 \to D_{(s)}^- D_s^+$, modes, are summarized in Table 8.7.

8.5.3 $B^0 \to D_s^{(*)+} D^{(*)-}$ Fit Systematic Uncertainty

The B meson decay modes with excited D mesons are more sensitive to the fit systematic uncertainty due to the wider $B^0 \to D^{(*)-} D_s^{(*)+}$ signals and the higher combinatorial and physics background in the lower mass region. The fit systematic uncertainties

Mode	Mass Parameter	Width Parameter
$B^0 \to D^- D_s^+ (\phi\pi^+)$	$< 0.5\%$	$\pm 1.6\%$
$B^0 \to D^- D_s^+ (K^{*0} K^+)$	$< 0.5\%$	$\pm 1.5\%$
$B^0 \to D^- D_s^+ (\pi^+\pi^+\pi^-)$	$< 0.5\%$	$\pm 1.2\%$
$B_s^0 \to D_s^- (\phi\pi^-) D_s^+ (\phi\pi^+)$	$\pm 1.1\%$	$\pm 0.0\%$
$B_s^0 \to D_s^- (\phi\pi^-) D_s^+ (\phi\pi^+)$	$\pm 3.3\%$	$\pm 3.3\%$
$B_s^0 \to D_s^- (\phi\pi^-) D_s^+ (\phi\pi^+)$	$\pm 3.6\%$	$\pm 1.2\%$

Table 8.8: Systematic uncertainties due to the signal mass and width parameters for $B^0_{(s)} \to D^-_{(s)} D_s^+$ modes.

for $B^0 \to D^{(*)-} D_s^{(*)+}$ modes are summarized in Table 8.9. They are very similar to the systematic uncertainties for the other double charm modes as described below.

Varied Parameter	$B^0 \to D_s^* D^-$	$B^0 \to D_s^- D^{*+}$	$B^0 \to D_s^* D^{*+}$
$B^0 \to D_s^- D^{*+}$ Width	$\pm 1.\%$	$\pm 2.0\%$	$\pm 1.0\%$
$B^0 \to D^+ X$ Normalization	$\pm 8.\%$	$\pm 2.0\%$	$\pm 4.0\%$

Table 8.9: Fit systematic uncertainties for $B^0 \to D_s^{(*)} D^{(*)+}$ decay modes.

The width of the narrow double peak structure for $B^0 \to D_s^+ D^{*-}$ mode is corrected by $16 \pm 2\%$ inline with our estimate described in Section 5.3. To estimate the systematic uncertainty due to the width correction, we vary the width within one standard deviation the same way it is done for the width of the other B meson signals. The other two B meson decay modes with excited D mesons are less affected by the width correction (Table 8.9).

To estimate the systematic uncertainty due to the semi-generic background template, derived by using $B \to D^- (K^+\pi^-\pi^-) X$ semi-generic Monte Carlo, we vary the norm of the template by one standard deviation of the fitted value (Table 8.9).

The fractions of the D_s^{*+} decays are defined within $\pm 2.5\%$ uncertainty [1]. We check that the reconstruction efficiencies for the two D_s^{*+} decay modes are the same. To be conservative, we assign $\pm 2.5\%$ uncertainty to the effect, because different template shapes for the $D_s^{*+} \to D_s^+ \gamma$ and $D_s^{*+} \to D_s^+ \pi^0$ decays could in theory change the yield of the signal. The uncertainty is only applied to the B meson decay modes with D_s^{*+} meson among the decay products (Table 8.12).

8.6 Summary of Systematic Effects

The summary of the systematic uncertainties is listed in Table 8.11 with the addition of the optimization bias described in Section 7. The systematic uncertainties due to B meson p_T spectrum, B meson lifetime, and trigger effects are common for all the modes (Table 8.10). The 3π system resonant composition systematic uncertainty only affects the ratios of branching fractions containing $B^0_{(s)} \to D^-_{(s)}\pi^+\pi^+\pi^-$ modes. The $D^-_s \to \pi^+\pi^-\pi^-$ sample composition systematic uncertainty only affects the ratios including modes containing $D^-_s \to \pi^+\pi^-\pi^-$ decay. The systematic uncertainties for $B^0 \to D^{(*)-}D_s^{(*)+}$ modes are summarized in Table 8.12.

Effect	Syst. Uncertainty [%]
BP_T spectrum	$\pm 3.0\%$
B^0_s lifetime	$\pm 2.0\%$
Trigger	$\pm 1.5\%$

Table 8.10: Systematic uncertainties which are common for all the decay modes.

Mode	3π	$D^-_s \to \pi^+\pi^-\pi^-$	Fit	Bias
$B^0 \to D^-\pi^+\pi^+\pi^-$	$\pm 2.5\%$		$\pm 1.3\%$	
$B^0_s \to D^-_s(\phi\pi^-)\pi^+\pi^+\pi^-$	$\pm 2.5\%$		$\pm 3.9\%$	
$B^0_s \to D^-_s(K^{*0}K^-)\pi^+\pi^+\pi^-$	$\pm 2.5\%$		$\pm 9.3\%$	
$B^0_s \to D^-_s(\pi^+\pi^-\pi^-)\pi^+\pi^+\pi^-$	$\pm 2.5\%$	$\pm 3.0\%$	$\pm 4.7\%$	
$B^0 \to D^-_s(\phi\pi^-)D^-$			$\pm 2.3\%$	
$B^0 \to D^-_s(K^{*0}K^-)D^-$			$\pm 4.2\%$	
$B^0 \to D^-_s(\pi^+\pi^-\pi^-)D^-$		$\pm 3.0\%$	$\pm 8.4\%$	
$B^0_s \to D^+_s D^-_s(\phi\pi^-)$			$\pm 4.4\%$	-5.0%
$B^0_s \to D^+_s D^-_s(K^{*0}K^-)$			$\pm 8.2\%$	-13.0%
$B^0_s \to D^+_s D^-_s(\pi^+\pi^-\pi^-)$		$\pm 3.0\%$	$\pm 4.6\%$	-4.0%

Table 8.11: Systematic uncertainties for individual channels. The uncertainty due to the 3π system resonance structure is accounted once for $\mathcal{B}(B^0_s \to D^-_s\pi^+\pi^+\pi^-)/\mathcal{B}(B^0 \to D^-\pi^+\pi^+\pi^-)$ ratios of branching fractions.

Varied Parameter	$B^0 \to D_s^* D^-$	$B^0 \to D_s^- D^{*+}$	$B^0 \to D_s^* D^{*+}$
Fit Syst	$\pm 8.0\%$	$\pm 3.0\%$	$\pm 4.0\%$
D_s^* Composition	$\pm 2.5\%$		$\pm 2.5\%$

Table 8.12: Systematic uncertainties for $B^0 \to D^{(*)-} D_s^{(*)+}$ modes.

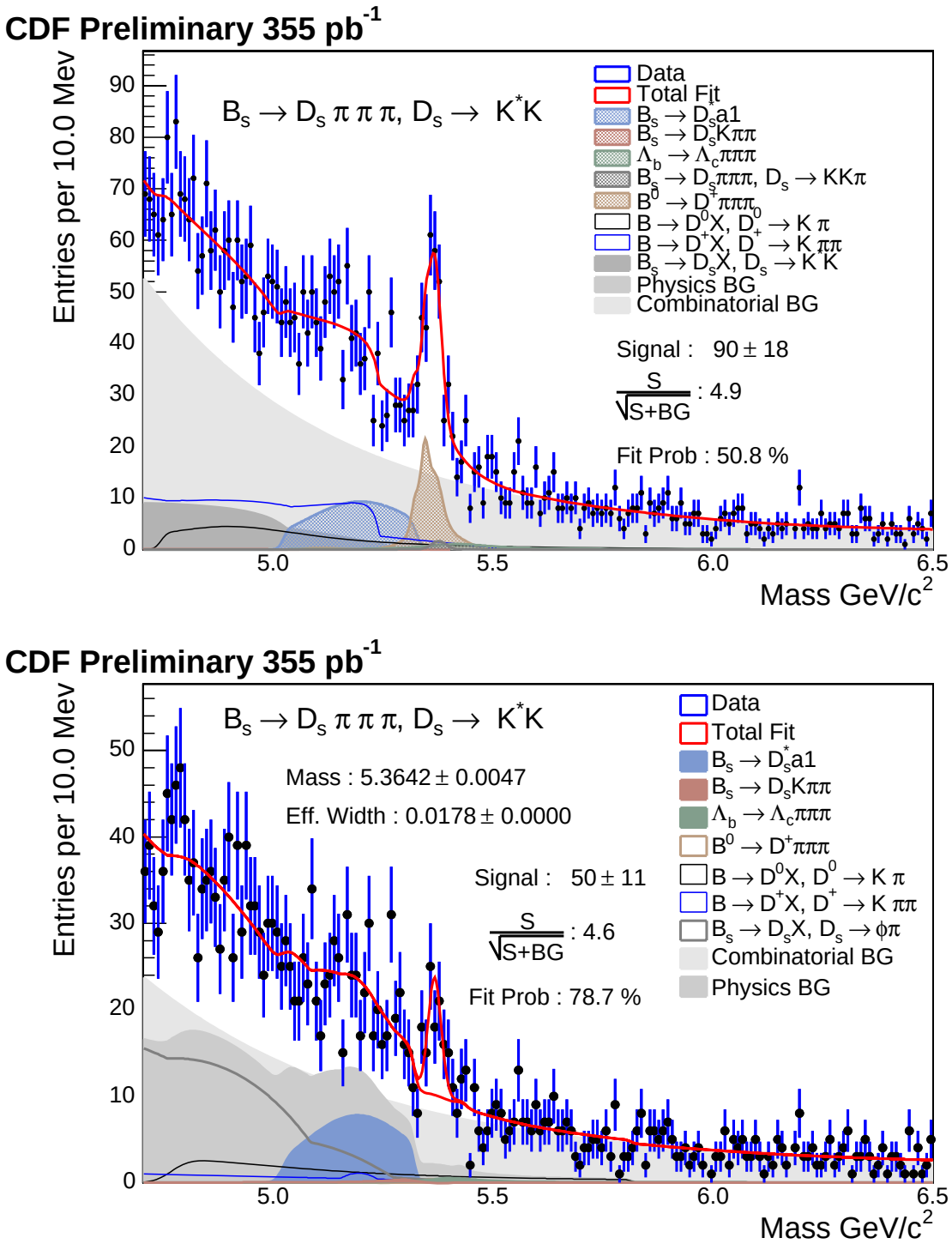

Figure 8-9: Reconstructed $B_s^0 \to D_s^-(K^{*0}K^-)\pi^+\pi^+\pi^-$ mass distribution. $D^- \to K^+\pi^-\pi^-$ veto is not applied (top), the veto is applied (bottom).

Chapter 9

Results

To improve statistics we measure the ratios of brnching fractions for $D_s^- \to \phi\pi^-$, $D_s^- \to K^{*0}K^-$, and $D_s^- \to \pi^+\pi^-\pi^-$ decay modes. We combine the results and uncertainties for three modes taking into account the event yield. Table 9.1 shows the results and the combined uncertainties for individual channels for the ratios of branching fractions multiplied by the relative production rate f_s/f_d.

Ratio	Result	Stat	Syst	$\mathcal{B}(D_s^- \to \phi\pi^-)$
$\frac{f_s}{f_d} \cdot \frac{\mathcal{B}(B_s^0 \to D_s^- \pi^+\pi^+\pi^-)}{\mathcal{B}(B^0 \to D^- \pi^+\pi^+\pi^-)}$				
$D_s^- \to \phi\pi^-$	0.263	± 0.029	± 0.021	± 0.035
$D_s^- \to K^{*0}K^-$	0.274	± 0.053	± 0.032	± 0.045
$D_s^- \to \pi^+\pi^-\pi^-$	0.293	± 0.067	± 0.025	± 0.054
$\frac{f_s}{f_d} \cdot \frac{\mathcal{B}(B_s^0 \to D_s^- D_s^+)}{\mathcal{B}(B^0 \to D^- D_s^+)}$				
$D_s^- \to \phi\pi^-$	0.25	$^{+0.10}_{-0.08}$	$^{+0.02}_{-0.02}$	± 0.03
$D_s^- \to K^{*0}K^-$	0.39	$^{+0.23}_{-0.19}$	$^{+0.03}_{-0.04}$	± 0.05
$D_s^- \to \pi^+\pi^-\pi^-$	0.69	$^{+0.31}_{-0.26}$	$^{+0.03}_{-0.03}$	± 0.09

Table 9.1: The individual results for ratios of branching fractions multiplied by f_s/f_d with statistical uncertainty, combined systematic uncertainty and the uncertainty due to the branching fraction.

Using the most recent value $f_s/f_d = 0.259 \pm 0.038$ [1], we calculate the ratios of branching fractions summarized in Table 9.2. The uncertainty from branching fractions has the common component due to $\mathcal{B}(D_s^- \to \phi\pi^-)$, and individual components due to various ratios of branching fractions.

Ratio	Result	Stat	Syst	f_s/f_d	$\mathcal{B}(D_s^- \to \phi\pi^-)$	$\mathcal{B}$
$\frac{\mathcal{B}(B_s^0 \to D_s^- \pi^+\pi^+\pi^-)}{\mathcal{B}(B^0 \to D^- \pi^+\pi^+\pi^-)}$						
$D_s^- \to \phi\pi^-$	1.02	± 0.11	± 0.08	± 0.15	± 0.14	
$D_s^- \to K^{*0}K^-$	1.06	± 0.20	± 0.12	± 0.16	± 0.17	
$D_s^- \to \pi^+\pi^-\pi^-$	1.13	± 0.26	± 0.10	± 0.17	± 0.21	
$\frac{\mathcal{B}(B^0 \to D^- D_s^+)}{\mathcal{B}(B^0 \to D^- \pi^+\pi^+\pi^-)}$						
$D_s^- \to \phi\pi^-$	1.59	± 0.14	± 0.12		± 0.21	
$D_s^- \to K^{*0}K^-$	1.44	± 0.15	± 0.12		± 0.23	
$D_s^- \to \pi^+\pi^-\pi^-$	1.45	± 0.23	± 0.16		± 0.26	
$\frac{\mathcal{B}(B^0 \to D_s^{*+} D^-)}{\mathcal{B}(B^0 \to D^- D_s^+)}$	0.89	± 0.20	± 0.08			
$\frac{\mathcal{B}(B^0 \to D_s D^{*-})}{\mathcal{B}(B^0 \to D^- D_s^+)}$	1.47	± 0.45	± 0.07			
$\frac{\mathcal{B}(B^0 \to D_s^{*+} D^{*-})}{\mathcal{B}(B^0 \to D^- D_s^+)}$	2.59	± 0.51	± 0.16			
$\frac{\mathcal{B}(B_s^0 \to D_s^- D_s^+)}{\mathcal{B}(B^0 \to D^- D_s^+)}$						
$D_s^- \to \phi\pi^-$	0.98	$^{+0.38}_{-0.32}$	$^{+0.08}_{-0.09}$	± 0.14	± 0.13	
$D_s^- \to K^{*0}K^-$	1.51	$^{+0.87}_{-0.70}$	$^{+0.17}_{-0.23}$	± 0.22	± 0.20	
$D_s^- \to \pi^+\pi^-\pi^-$	2.67	$^{+1.20}_{-0.99}$	$^{+0.30}_{-0.34}$	± 0.39	± 0.36	
$\frac{\mathcal{B}(B_s^0 \to D_s^- D_s^+)}{\mathcal{B}(B_s^0 \to D_s^- \pi^+\pi^+\pi^-)}$						
$D_s^- \to \phi\pi^-$	1.52	$^{+0.60}_{-0.51}$	$^{+0.14}_{-0.16}$		± 0.20	
$D_s^- \to K^{*0}K^-$	2.05	$^{+1.23}_{-1.00}$	$^{+0.29}_{-0.39}$		± 0.27	
$D_s^- \to \pi^+\pi^-\pi^-$	3.42	$^{+1.64}_{-1.39}$	$^{+0.32}_{-0.35}$		± 0.44	

Table 9.2: The individual results for ratios of branching fractions multiplied by f_s/f_d with statistical uncertainty, combined systematic uncertainty, and the uncertainties due to the production ratio f_s/f_d, $\mathcal{B}(D_s^- \to \phi\pi^-)$, and the rest of the branching fractions.

9.1 Combining Results

The B meson decay modes reconstructed using the $D_s^- \to \phi\pi^-$ decay channel make up the largest fractions of the total samples. The addition of the modes reconstructed using the $D_s^- \to K^{*0}K^-$ and $D_s^- \to \pi^+\pi^-\pi^-$ decay channels lowers the statistical uncertainty and increases the significance of the measurement. For each ratio of branching fractions, we combine the results for three D_s^- meson decay channels, weighting them by efficiencies measured using Monte Carlo simulations. For $\mathcal{B}(B_s^0 \to D_s^- \pi^+\pi^+\pi^-)/\mathcal{B}(B^0 \to D^- \pi^+\pi^+\pi^-)$, we use the formula

$$\frac{\mathcal{B}(B_s^0 \to D_s^- \pi^+\pi^+\pi^-)}{\mathcal{B}(B^0 \to D^- \pi^+\pi^+\pi^-)} = \frac{N_1+N_2+N_3}{N} \cdot \frac{\epsilon_0}{\epsilon_1 + r_2\epsilon_2 + r_3\epsilon_3} \cdot \frac{\mathcal{B}(D^- \to K^+\pi^-\pi^-)}{\mathcal{B}(D_s^- \to \phi\pi^-)}.$$

For $\mathcal{B}(B^0 \to D^- D_s^+)/\mathcal{B}(B^0 \to D^-\pi^+\pi^+\pi^-)$, we combine results using a similar formula

$$\frac{\mathcal{B}(B^0 \to D^- D_s^+)}{\mathcal{B}(B^0 \to D^- \pi^+\pi^+\pi^-)} = \frac{N_1+N_2+N_3}{N} \cdot \frac{\epsilon_0}{\epsilon_1 + r_2\epsilon_2 + r_3\epsilon_3} \cdot \frac{1}{\mathcal{B}(D_s^- \to \phi\pi^-)},$$

where

$r_2 = \frac{\Gamma(K^+\bar{K}^*(892)^0, \bar{K}_0^* \to K^-\pi^+)}{\Gamma(\phi\pi^-)}$,

$r_3 = \frac{\Gamma(\pi^+\pi^-\pi^-)}{\Gamma(\phi\pi^-)}$,

ϵ_i - Monte Carlo efficiency.

N is the number of $B^0 \to D^-\pi^+\pi^+\pi^-$ events and N_i, where $i = 1, 2, 3$, are the yields for $B_s^0 \to D_s^-\pi^+\pi^+\pi^-$ and $B^0 \to D^- D_s^+$ modes, reconstructed using $D_s^- \to \phi\pi^-$, $D_s^- \to K^{*0}K^-$, and $D_s^- \to \pi^+\pi^-\pi^-$ channels, correspondingly. The combined statistical uncertainty is introduced by the first term of the equation with the ratio of the data yields. The ratio of Monte Carlo efficiencies introduces the uncertainties due to the ratios of branching fractions r_2 and r_3. The last term of the equation introduces the uncertainty due to the branching fractions, which is common for all three channels and is dominated by the $\mathcal{B}(D_s^- \to \phi\pi^-)$ uncertainty.

The systematic uncertainty introduced by the $B^0 \to D^-\pi^+\pi^+\pi^-$reconstruction, together with the systematic uncertainties due to the B meson p_T spectrum, B meson lifetime, and trigger effects, are common for all three D_s^- channels. The systematic uncertainties specific to the different D_s^- channels are combined taking into account the correspondent $B_s^0 \to D_s^-\pi^+\pi^+\pi^-$ and $B^0 \to D^- D_s^+$ measured yield. For our dataset, we find

$$\frac{f_s}{f_d} \cdot \frac{\mathcal{B}(B_s^0 \to D_s^-\pi^+\pi^+\pi^-)}{\mathcal{B}(B^0 \to D^-\pi^+\pi^+\pi^-)} = 0.271 \pm 0.025 \pm 0.021 \pm 0.037(\mathcal{B}(D_s^- \to \phi\pi^-)).$$

Using the latest value $\frac{f_s}{f_d} = 0.259 \pm 0.038$ [1], we determine

$$\frac{\mathcal{B}(B_s^0 \to D_s^- \pi^+ \pi^+ \pi^-)}{\mathcal{B}(B^0 \to D^- \pi^+ \pi^+ \pi^-)} = 1.05 \pm 0.10 \pm 0.08 \pm 0.15(f_s/f_d) \pm 0.14(\mathcal{B}(D_s^- \to \phi\pi^-)).$$

Similarly for $B^0 \to D^- D_s^+$ mode we find

$$\frac{\mathcal{B}(B^0 \to D^- D_s^+)}{\mathcal{B}(B^0 \to D^- \pi^+ \pi^+ \pi^-)} == 1.51 \pm 0.10 \pm 0.11 \pm 0.20(\mathcal{B}(D_s^- \to \phi\pi^-)).$$

We measure $B^0 \to D^{(*)-} D_s^{(*)+}$ branching fractions for the modes reconstructed using, $D_s^- \to \phi\pi^-$ decay channel. We do not use $D_s^- \to K^{*0} K^-$ and $D_s^- \to \pi^+\pi^-\pi^-$ channels for thess measurements due to the low statistics and high systematic uncertainty. Adding the systematic uncertainty to the result we find:

$$\frac{\mathcal{B}(B^0 \to D_s^{*+} D^-)}{\mathcal{B}(B^0 \to D^- D_s^+)} = 0.89 \pm 0.20 \pm 0.08,$$

$$\frac{\mathcal{B}(B^0 \to D_s D^{*-})}{\mathcal{B}(B^0 \to D^- D_s^+)} = 1.47 \pm 0.45 \pm 0.07,$$

$$\frac{\mathcal{B}(B^0 \to D_s^{*+} D^{*-})}{\mathcal{B}(B^0 \to D^- D_s^+)} = 2.59 \pm 0.51 \pm 0.16.$$

There is no branching fraction uncertainty in these measurements because both $\mathcal{B}(D_s^- \to \phi\pi^-)$ and $\mathcal{B}(D^- \to K^+\pi^-\pi^-)$ are canceled in the ratios.

We combine the results for $\mathcal{B}(B_s^0 \to D_s^- D_s^+)/\mathcal{B}(B^0 \to D^- D_s^+)$ by using the formula

$$\frac{\mathcal{B}(B_s^0 \to D_s^- D_s^+)}{\mathcal{B}(B^0 \to D^- D_s^+)} = \frac{N_{1,1} + N_{1,2} + N_{1,3}}{N_{0,1} + N_{0,2} + N_{0,3}} \cdot \frac{\epsilon_{0,1} + r_2\epsilon_{0,2} + r_3\epsilon_{0,3}}{\epsilon_{1,1} + r_2\epsilon_{1,2} + r_3\epsilon_{1,3}} \cdot \frac{\mathcal{B}(D^- \to K^+\pi^-\pi^-)}{\mathcal{B}(D_s^- \to \phi\pi^-)}$$

Here the first index 0 is used for $B^0 \to D^- D_s^+$ modes, and the first index 1 is used for $B_s^0 \to D_s^- D_s^+$ modes. The second index 1,2,3 is used for decays reconstructed using the $D_s^- \to \phi\pi^-$, $D_s^- \to K^{*0} K^-$, and $D_s^- \to \pi^+\pi^-\pi^-$ channels, respectively. For our dataset, we find

$$\frac{f_s}{f_d} \cdot \frac{\mathcal{B}(B_s^0 \to D_s^- D_s^+)}{\mathcal{B}(B^0 \to D^- D_s^+)} = 0.37^{+0.10\ +0.03}_{-0.08\ -0.04} \pm 0.01(\mathcal{B}) \pm 0.05(\mathcal{B}(D_s^- \to \phi\pi^-)),$$

Using the latest value $\frac{f_s}{f_d} = 0.259 \pm 0.038$ [1], we determine

$$\frac{\mathcal{B}(B_s^0 \to D_s^- D_s^+)}{\mathcal{B}(B^0 \to D^- D_s^+)} = 1.44^{+0.38\ +0.11}_{-0.31\ -0.14} \pm 0.21(f_s/f_d) \pm 0.02(\mathcal{B}) \pm 0.20(\mathcal{B}(D_s^- \to \phi\pi^-)).$$

We combine results for $\mathcal{B}(B_s^0 \to D_s^- D_s^+)/\mathcal{B}(B_s^0 \to D_s^- \pi^+\pi^+\pi^-)$ by using the formula

$$\frac{\mathcal{B}(B_s^0 \to D_s^- D_s^+)}{\mathcal{B}(B_s^0 \to D_s^- \pi^+\pi^+\pi^-)} = \frac{N_{1,1} + N_{1,2} + N_{1,3}}{N_{0,1} + N_{0,2} + N_{0,3}} \cdot \frac{\epsilon_{0,1} + r_2\epsilon_{0,2} + r_3\epsilon_{0,3}}{\epsilon_{1,1} + r_2\epsilon_{1,2} + r_3\epsilon_{1,3}} \cdot \frac{1}{\mathcal{B}(D_s^- \to \phi\pi^-)}.$$

The first index 0 is used for $B_s^0 \to D_s^- \pi^+\pi^+\pi^-$ mode and the first index 1 is used for $B_s^0 \to D_s^- D_s^+$ mode. The second index 1,2,3 is used for decays reconstructed using the $D_s^- \to \phi\pi^-$, $D_s^- \to K^{*0}K^-$, and $D_s^- \to \pi^+\pi^-\pi^-$ channels, correspondingly. For our dataset, we find

$$\frac{\mathcal{B}(B_s^0 \to D_s^- D_s^+)}{\mathcal{B}(B_s^0 \to D_s^- \pi^+\pi^+\pi^-)} = 2.07^{+0.56\ +0.17}_{-0.46\ -0.22} \pm 0.04(\mathcal{B}) \pm 0.27(\mathcal{B}(D_s^- \to \phi\pi^-)).$$

To estimate the lower bound for $\Delta\Gamma_s^{\mathrm{CP}}/\Gamma_s$, we need to estimate the lower bound for $\mathcal{B}(B_s^0 \to D_s^- D_s^+)$. For this, we generate the outcomes of 2000 pseudo-experiments using Poissonian distribution for pseudo-yields with the average equal to the measured yields of three $B_s^0 \to D_s^- D_s^+$ decay modes. We calculate the combined result for $\mathcal{B}(B_s^0 \to D_s^- D_s^+)$ the same way we do it in our analysis. Then we smear it systematic uncertainty of the measurement combined with production ratio (f_s/f_d) uncertainty, and $\mathcal{B}(D_s^- \to \phi\pi^-)$ uncertainty using Normal distribution. We set a 95% confidence lower limit by finding a value of branching fraction with 5% of outcomes of pseudo-experiments below it (Figure 9-1).

$$\mathcal{B}(B_s^0 \to D_s^- D_s^+) > 5.8 \times 10^{-3} \text{ at } 95\% \text{ C.L.} \tag{9.1}$$

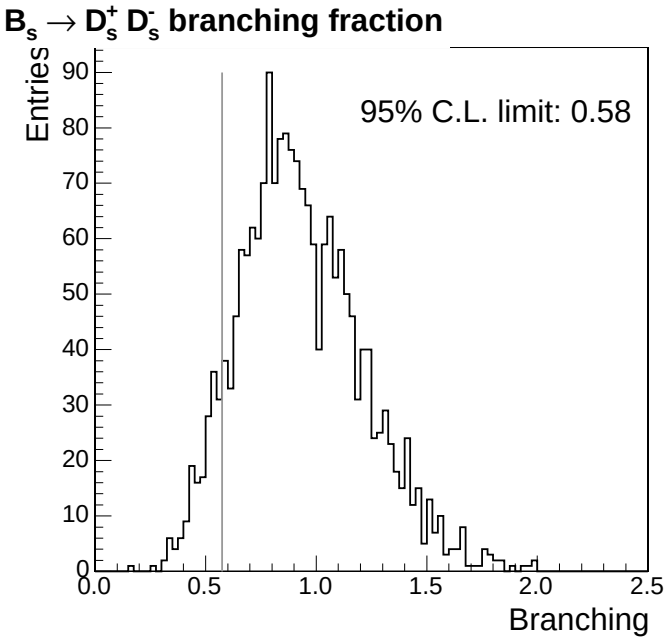

Figure 9-1: $\mathcal{B}(B_s^0 \to D_s^- D_s^+)$ measured in 2000 pseudo-experiments.

Using the lower bound estimate from Eq. (1.11)

$$\Delta\Gamma_s^{\mathrm{CP}}/\Gamma_s \geq 2(\mathcal{B}(B_s^0 \to D_s^{(*)-} D_s^{(*)+})) \geq 2(\mathcal{B}(B_s^0 \to D_s^- D_s^+)). \tag{9.2}$$

Substituting (9.1), we obtain

$$\Delta\Gamma_s^{\mathrm{CP}}/\Gamma_s \geq 0.012 \text{ at } 95\% \text{ C.L.} \tag{9.3}$$

Chapter 10

Conclusion

In this thesis, we use the data sample collected with the CDF detector between February 2002 and August 2004 in $p\overline{p}$ collisions at $\sqrt{s} = 1.96$ TeV and corresponding to about 355 pb^{-1} integrated luminosity.

We make the first observation of the exclusive $B_s^0 \to D_s^- D_s^+$ decay mode with the significance of better than 7.5 standard deviations. We measure the ratio of branching fractions $\mathcal{B}(B_s^0 \to D_s^- D_s^+)/\mathcal{B}(B^0 \to D^- D_s^+)$ shown in Table 10.1, combining statistical and systematic uncertainties, and excluding uncertainties from other sources. Using the world average for the $\mathcal{B}(B^0 \to D^- D_s^+)$ branching fraction we find the absolute branching fraction $\mathcal{B}(B_s^0 \to D_s^- D_s^+)$.

$$\mathcal{B}(B_s^0 \to D_s^- D_s^+) = (9.4^{+4.4}_{-4.2}) \times 10^{-3}, \tag{10.1}$$

and estimate that $\Delta\Gamma_s^{\rm CP}/\Gamma_s$ is

$$\frac{\Delta\Gamma_s^{\rm CP}}{\Gamma_s} \geq 0.012 \text{ at } 95\% \text{ C.L.} \tag{10.2}$$

We observe the double-charm decay of the B meson for the first time at the Tevatron Collider. We measure the ratio of branching fraction $\mathcal{B}(B^0 \to D^- D_s^+)/\mathcal{B}(B^0 \to D^- \pi^+ \pi^+ \pi^-)$ with the accuracy better than the world average (Table 10.1). We measure ratios of branching fractions $\mathcal{B}(B^0 \to D^{(*)-} D_s^{(*)+})/\mathcal{B}(B^0 \to D^- D_s^+)$, which do not depend on the other branching fractions.

Mode	Our Measurement	PDG
$\mathcal{B}(B_s^0 \to D_s^- \pi^+ \pi^+ \pi^-)/\mathcal{B}(B^0 \to D^- \pi^+ \pi^+ \pi^-)$	1.05 ± 0.24	N.A.
$\mathcal{B}(B^0 \to D^- D_s^+)/\mathcal{B}(B^0 \to D^- \pi^+ \pi^+ \pi^-)$	1.51 ± 0.24	0.8 ± 0.4
$\mathcal{B}(B^0 \to D^{*-} D_s^-)/\mathcal{B}(B^0 \to D^- D_s^+)$	0.89 ± 0.22	1.4 ± 0.5
$\mathcal{B}(B^0 \to D^- D_s^{*+})/\mathcal{B}(B^0 \to D^- D_s^+)$	1.47 ± 0.46	1.3 ± 0.7
$\mathcal{B}(B^0 \to D^{*-} D_s^{*+})/\mathcal{B}(B^0 \to D^- D_s^+)$	2.59 ± 0.53	4.0 ± 1.5
$\mathcal{B}(B_s^0 \to D_s^- D_s^+)/\mathcal{B}(B^0 \to D^- D_s^+)$	$1.44^{+0.49}_{-0.45}$	N.A.
$\mathcal{B}(B_s^0 \to D_s^- D_s^+)/\mathcal{B}(B_s^0 \to D_s^- \pi^+ \pi^+ \pi^-)$	$2.07^{+0.65}_{-0.57}$	N.A.

Table 10.1: The ratios of branching fractions with uncertainties.

We make the first observation of the $B_s^0 \to D_s^- \pi^+ \pi^+ \pi^-$ decay mode and measure its branching fraction with respect to the $\mathcal{B}(B^0 \to D^- \pi^+ \pi^+ \pi^-)$ mode. The reconstructed $B_s^0 \to D_s^- \pi^+ \pi^+ \pi^-$ meson candidates with $D_s^- \to \phi \pi^-$, $K^{*0} K^-$, and $\pi^+ \pi^- \pi^-$ were also used for the measurement of the frequency of the $B_s^0 - \overline{B_s^0}$ oscillations at CDF [13].

Appendix A

Tables

A.1 Monte Carlo Decay Tables.

```
Decay anti-B0
0.0090   a_1-  D+               SVS;
0.0005   D+    rho0  pi-         PHSP;
0.0005   D+    pi-   pi+  pi-    PHSP;
Enddecay
#
Decay D+
0.0900   K-    pi+   pi+         D_DALITZ;
Enddecay
#
Decay a_1-
0.6      rho0  pi-               VVS_PWAVE 1.0 0.0 0.0 0.0 -0.1 0.0;
Enddecay
#
Decay rho0
1.000    pi+   pi-               VSS;
Enddecay
```

Table A.1: Decay table for $B^0 \to D^-\pi^+\pi^+\pi^-$ signal Monte Carlo simulation.

```
Decay B0
#
## Signal ##
0.0090  a_1+ D-            SVS;
0.0005  D-   rho0 pi+      PHSP;
0.0005  D-   pi-  pi+  pi+ PHSP;
#
## D* reflection ##
0.0130  D*-  a_1+          SVV_HELAMP 0.336 0.0 0.88 0.0 0.336 0.0;
0.0010  D*-  rho0 pi+      PHSP;
0.0077  D*-  pi-  pi+ pi+  PHSP;
#
## Cabibbo suppressed ##
0.0090  K_1+ D-            SVS;
0.0005  D-   rho0 K+       PHSP;
0.0005  D-   pi-  K+  pi+  PHSP;
Enddecay
#
Decay D-
0.0900  K+   pi-  pi-      D_DALITZ;
Enddecay
```

Table A.2: Decay table for $B^0 \to D^{*-}\pi^+\pi^+\pi^-$ and the Cabibbo suppressed templates.

```
Decay anti-B0
#
# Signal
0.0090   a_1-  D+               SVS;
0.0005   D+    rho0  pi-        PHSP;
0.0005   D+    pi-   pi+  pi-   PHSP;
#
# Cabibbo Suppressed
0.0005   K_1-  D+               SVS;
0.0005   D+    rho0  K-         PHSP;
0.0005   D+    K-    pi+  pi-   PHSP;
#
# D* Reflection
0.0130   D*+   a_1-             SVV_HELAMP 0.336 0.0 0.88 0.0 0.336 0.0;
0.0010   D*+   rho0  pi-        PHSP;
Enddecay
#
Decay D*+
0.3060   D+    pi0              VSS;
0.0110   D+    gamma            VSP_PWAVE;
Enddecay
#
Decay D+
0.0900   K-    pi+   pi+        D_DALITZ;
Enddecay
#
Decay a_1-
0.6      rho0  pi-              VVS_PWAVE 0.995 0.0 0.0 0.0 -0.1 0.0;
Enddecay
#
Decay rho0
1.000    pi+   pi-              VSS;
Enddecay
```

Table A.3: Decay table for $B^0 \to D^- \pi^+ \pi^+ \pi^-$ signal, B^0 meson Cabibbo suppressed decay modes, and $B^0 \to D^{*-} \pi^+ \pi^+ \pi^-$ modes Monte Carlo simulation.

```
Decay B_s0
0.0090   a_1+  D_s-              SVS;
0.0005   D_s-  rho0  pi+         PHSP;
0.0005   D_s-  pi-   pi+   pi+   PHSP;
Enddecay
#
Decay D_s-
0.0228   K*0   K-                SVS;
0.0180   phi   pi-               SVS;
0.0090   K-    K+    pi-         PHSP;
0.0004   rho0  pi-               SVS;
0.0100   f_0   pi-               PHSP;
0.0020   f_2   pi-               PHSP;
0.0033   f'_0  pi-               PHSP;
Enddecay
#
Decay K*0
0.6657   K+    pi-               VSS;
Enddecay
Decay phi
0.4910   K+    K-                VSS;
Enddecay
Decay f_0
0.5200   pi+   pi-               PHSP;
0.4800   K+    K-                PHSP;
Enddecay
Decay f_2
0.5650   pi+   pi-               TSS;
Enddecay
Decay f'_0
0.5200   pi+   pi-               PHSP;
Enddecay
Decay a_1+
0.6      rho0  pi+               VVS_PWAVE 1.0 0.0 0.0 0.0 -0.1 0.0;
Enddecay
Decay rho0
1.000    pi+   pi-               VSS;
Enddecay
```

Table A.4: Decay table for $B_s^0 \to D_s^- \pi^+ \pi^+ \pi^-$signal Monte Carlo simulation.

```
Decay B_s0
0.0122   D_s*-  a_1+                SVV_HELAMP  1.0 0.0 1.0 0.0 1.0 0.0;
0.0010   D_s*-  rho0   pi+          PHSP;
0.0077   D_s*-  pi-    pi+    pi+   PHSP;
0.0005   D_s-   rho0   K+           PHSP;
0.0005   D_s-   pi-    K+     pi+   PHSP;
0.0090   K_1+   D_s-                SVS;
0.01     D_s+   D-                  PHSP;
Enddecay
#
Decay D_s-
0.0228   K*0    K-                  SVS;
0.0180   phi    pi-                 SVS;
0.0004   rho0   pi-                 SVS;
0.0057   f_0    pi-                 PHSP;
0.0020   f_2    pi-                 PHSP;
0.0033   f'_0   pi-                 PHSP;
Enddecay
#
Decay D-
0.0900   K+     pi-    pi-          D_DALITZ;
Enddecay
#
Decay K*0
0.6657   K+     pi-                 VSS;
Enddecay
#
Decay phi
0.4910   K+     K-                  VSS;
Enddecay
#
Decay f_0
0.5200   pi+    pi-                 PHSP;
Enddecay
#
Decay f_2
0.5650   pi+    pi-                 TSS;
Enddecay
#
Decay f'_0
0.5200   pi+    pi-                 PHSP;
Enddecay
```

Table A.5: Decay table for Monte Carlo simulation of reflections into the $B_s^0 \to D_s^- \pi^+ \pi^+ \pi^-$ reconstructed mass distribution.

```
Decay anti-B0
0.0096   D+   D_s-             PHSP;
Enddecay
#
Decay D+
0.0900   K-   pi+   pi+        D_DALITZ;
Enddecay
#
Decay D_s-
0.0228   K*0  K-               SVS;
0.0180   phi  pi-              SVS;
0.0101   pi-  pi-   pi+        PHSP;
Enddecay
#
Decay K*0
0.6657   K+   pi-              VSS;
Enddecay
#
Decay phi
0.4910   K+   K-               VSS;
Enddecay
End
```

Table A.6: Decay table for $B^0 \to D^- D_s^+$ mixed signal Monte Carlo simulation.

```
Decay anti-B0
0.0080   D+     D_s-            PHSP;
0.0107   D*+    D_s-            SVS;
0.0100   D_s*-  D+              SVS;
0.0190   D_s*-  D*+             SVV_HELAMP 0.48 0.0 0.734 0.0 0.48 0.0;
Enddecay
#
Decay D+
0.0900   K-     pi+   pi+       D_DALITZ;
Enddecay
#
Decay D_s-
0.0228   K*0    K-              SVS;
0.0180   phi    pi-             SVS;
0.0090   K+ K-  pi-             PHSP;
0.0004   rho0   pi-             SVS;
0.0100   f_0    pi-             PHSP;
0.0020   f_2    pi-             PHSP;
0.0033   f'_0   pi-             PHSP;
Enddecay
#
Decay K*0
0.6657   K+     pi-             VSS;
Enddecay
Decay phi
0.4910   K+     K-              VSS;
Enddecay
Decay f_0
0.5200   pi+    pi-             PHSP;
0.4800   K+     K-              PHSP;
Enddecay
Decay f_2
0.5650   pi+    pi-             TSS;
Enddecay
Decay f'_0
0.5200   pi+    pi-             PHSP;
Enddecay
```

Table A.7: Decay table for $B^0 \to D^{(*)-} D_s^{(*)+}$ signal Monte Carlo simulation.

```
Decay B_s0
0.008      D_s-      D_s+        PHSP;
Enddecay
#
Decay D_s+
0.0228     anti-K*0  K+          SVS;
0.0180     phi       pi+         SVS;
0.0090     K+        K-   pi+    PHSP;
0.0004     rho0      pi+         SVS;
0.0100     f_0       pi+         PHSP;
0.0020     f_2       pi+         PHSP;
0.0033     f'_0      pi+         PHSP;
Enddecay
#
Decay K*0
0.6657     K+   pi-             VSS;
Enddecay
#
Decay phi
0.4910     K+   K-              VSS;
Enddecay
#
Decay f_0
0.5200     pi+  pi-             PHSP;
0.4800     K+   K-              PHSP;
Enddecay
#
Decay f_2
0.5650     pi+  pi-             TSS;
Enddecay
#
Decay f'_0
0.5200     pi+  pi-             PHSP;
Enddecay
```

Table A.8: Decay table for $B_s^0 \to D_s^- D_s^+$ signal Monte Carlo simulation.

```
Decay anti-B0
0.0060   a_1- D+          SVS;
0.0011   D+  rho0    pi-  PHSP;
0.0022   D+  pi+ pi- pi-  PHSP;
Enddecay
```

```
Decay anti-B0
0.0090   a_1- D+          SVS;
0.0005   D+  rho0    pi-  PHSP;
0.0005   D+  pi- pi+ pi-  PHSP;
Enddecay
```

Table A.9: Monte Carlo decay table for 3π resonant content before correction (left) and after correction (right).

```
Decay D_s-
0.0004    rho0   pi-    SVS;
0.0057    f_0    pi-    PHSP;
0.0020    f_2    pi-    PHSP;
0.0033    f'_0   pi-    PHSP;
Enddecay
```

```
Decay D_s-
0.0101    pi+ pi-  pi-   PHSP;
Enddecay
#
#
#
```

Table A.10: Decay tables for $D_s^- \to \pi^+\pi^-\pi^-$ sample composition study.

A.2 Selection Cuts

Cut	Value
B^0 $L_{xy}/\sigma(L_{xy})$	> 16
B^0 d_0	< 0.0065 cm
B^0 $\chi^2_{r\phi}$	< 14
D^- $L_{xy}/\sigma(L_{xy})$	> 15
D^- $L_{xy}^{\leftarrow B}$	> 0.015 cm
D^- $\chi^2_{r\phi}$	< 10
Track Min p_T	> 0.35 GeV/c

Table A.11: $B^0 \to D^-\pi^+\pi^+\pi^-$ optimized selection cuts.

Cut	$\phi\pi^-$	$\bar{K}^{*0}K^-$	$\pi^+\pi^-\pi^-$
B_s^0 $\frac{L_{xy}}{\sigma(L_{xy})}$	> 15	> 18	> 21
B_s^0 d_0	< 0.006 cm	< 0.005 cm	< 0.0055 cm
B_s^0 $\chi^2_{r\phi}$	< 10	< 8	< 10
D_s^- $\frac{L_{xy}}{\sigma(L_{xy})}$	> 10	> 15	> 20
D_s^- $L_{xy}^{\leftarrow B}$	> -0.01 cm	> 0.01 cm	> 0.015 cm
D_s^- $\chi^2_{r\phi}$	< 10	< 10	< 10
ϕ Mass	$[1.010, 1.029]$ GeV/c^2		
$\bar{K}^*$ Mass		$[0.84, 0.94]$ GeV/c^2	
Track Min p_T	> 0.35 GeV/c	> 0.35 GeV/c	> 0.48 GeV/c

Table A.12: $B_s^0 \to D_s^-\pi^+\pi^+\pi^-$ optimized selection cuts for different D_s^- decay channels.

Cut	$\phi\pi^-$	$K^{*0}K^-$	$\pi^+\pi^-\pi^-$
B $\frac{L_{xy}}{\sigma(L_{xy})}$	> 6	> 6	> 4
B $d0$	< 0.008 cm	< 0.008 cm	< 0.0075 cm
B $\chi^2_{r\phi}$	< 20	< 17	< 13
D_s^- $\frac{L_{xy}}{\sigma(L_{xy})}$	> 5	> 5	> 10
D_s^- $L_{xy}^{\leftarrow B}$	> -0.02 cm	> 0.0 cm	> -0.02 cm
D_s^- $\chi^2_{r\phi}$	< 15	< 15	< 15
D^+ $\frac{L_{xy}}{\sigma(L_{xy})}$	> 6	> 13	> 12
D^+ $L_{xy}^{\leftarrow B}$	> -0.02 cm	> 0.0 cm	> -0.02 cm
D^+ $\chi^2_{r\phi}$	< 15	< 15	< 15
ϕ Mass	$[1.010, 1.029]$ GeV/c^2		
K^* Mass		$[0.84, 0.94]$ GeV/c^2	
Track Min p_T	> 0.35 GeV/c	> 0.35 GeV/c	> 0.35 GeV/c

Table A.13: $B^0 \to D^- D_s^+$ optimized selection cuts for different D_s^- decay channels.

Cut	$\phi\pi^-$	$K^{*0}K^-$	$\pi^+\pi^-\pi^-$
B $\frac{L_{xy}}{\sigma(L_{xy})}$	> 5	> 6.5	> 10
B $d0$	< 0.011 cm	< 0.007 cm	< 0.009 cm
B $\chi^2_{r\phi}$	< 22	< 18	< 11
D_s^- $L_{xy}^{\leftarrow B}$	> -0.01 cm	> -0.01 cm	> -0.01 cm
D_s^- $\chi^2_{r\phi}$	< 15	< 15	< 15
D_s^- $L_{xy}^{\leftarrow B}$	> -0.01 cm	> -0.01 cm	> -0.01 cm
D_s^- $\chi^2_{r\phi}$	< 15	< 15	< 15
ϕ Mass	$[1.010, 1.029]$ GeV/c^2	$[1.010, 1.029]$ GeV/c^2	$[1.010, 1.029]$ GeV/c^2
K^* Mass		$[0.84, 0.94]$ GeV/c^2	
D^+ Veto Mass		$[1.845, 1.893]$ GeV/c^2	
Track Min p_T	> 0.5 GeV/c	> 0.5 GeV/c	> 0.55 GeV/c

Table A.14: $B_s^0 \to D_s^- D_s^+$ optimized selection cuts for different D_s^- decay channels.

Appendix B

Plots

B.1 Comparison of Data and Monte Carlo

We perform a detailed comparison of the Monte Carlo simulation with data using our most populated channel $B^0 \to D^-\pi^+\pi^+\pi^-$. For sideband subtractions we use the signal mass interval including 95.45% of the $B^0 \to D^-\pi^+\pi^+\pi^-$ signal and only right sideband with clean combinatorial background as shown on Figure B-1.

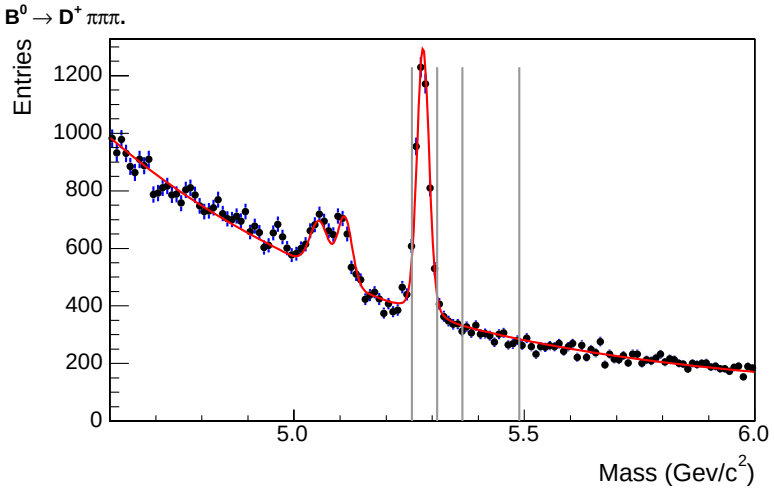

Figure B-1: Sideband and signal region used for compartison of data with Monte Carlo simulations in $B^0 \to D^-\pi^+\pi^+\pi^-$ mode.

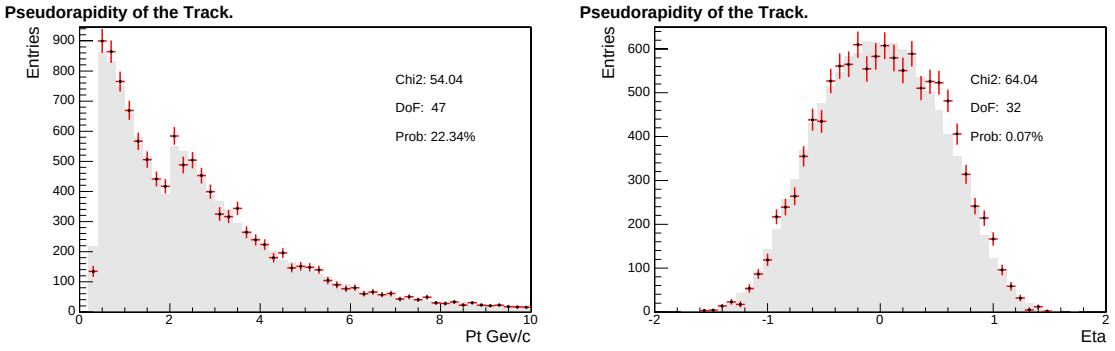

Figure B-2: Transverse momentum and pseudo-rapidity of the track.

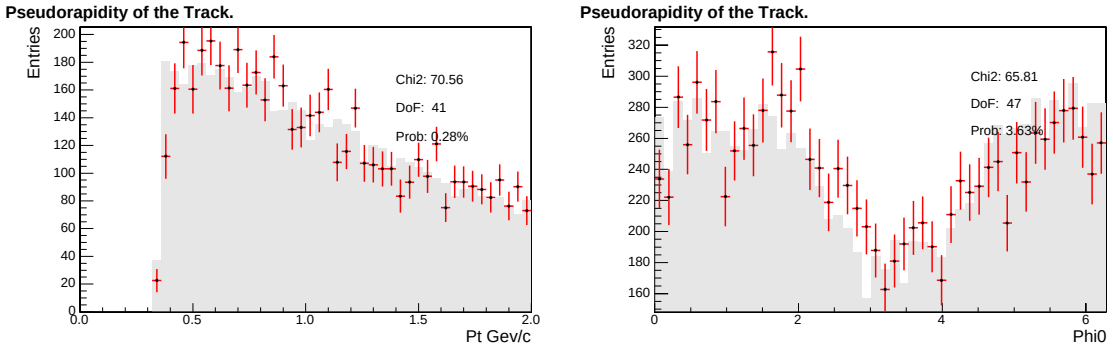

Figure B-3: Transverse momentum and ϕ_0 angle of the track

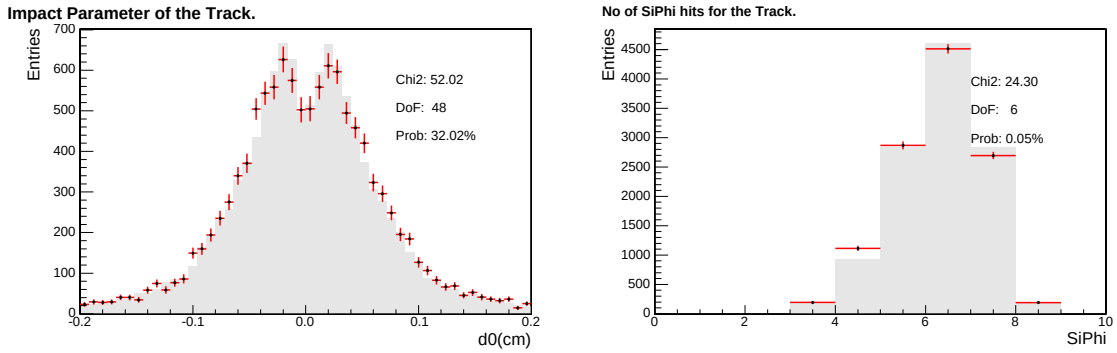

Figure B-4: Impact parameter of the track and number of $R\phi$ silicon hits per track.

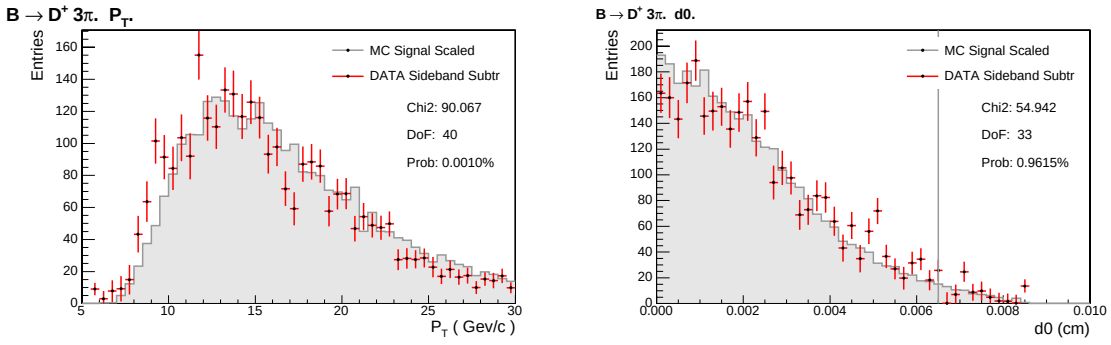

Figure B-5: Transverse momentum and impact parameter of the B^0 meson.

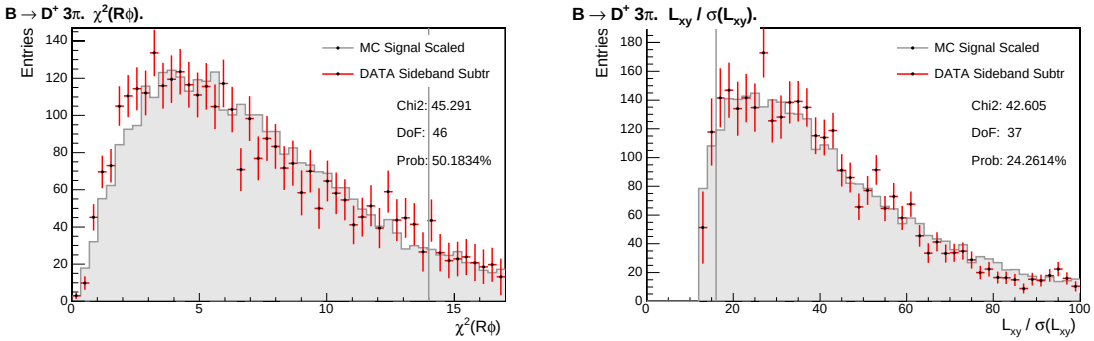

Figure B-6: $\chi^2_{R\phi}$ and $L_{xy}/\sigma(L_{xy})$ of the B^0 meson.

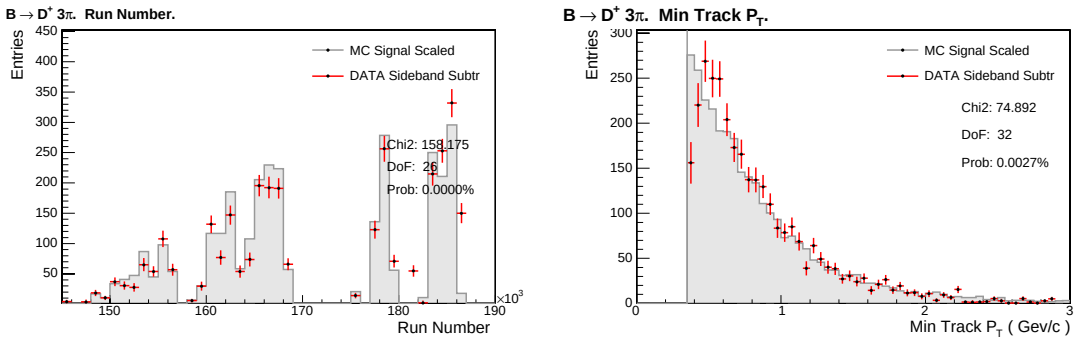

Figure B-7: Run number of candidate and minimum track p_T.

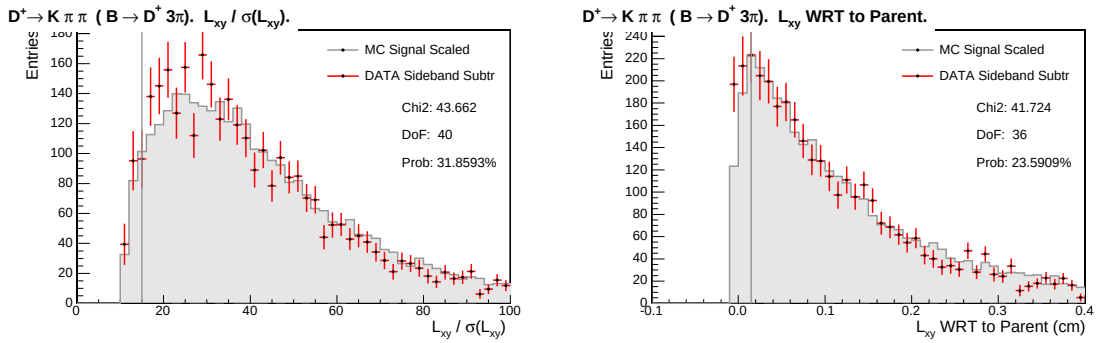

Figure B-8: $L_{xy}/\sigma(L_{xy})$ of the D^- meson and L_{xy} of the D^- meson with respect to B^0 meson.

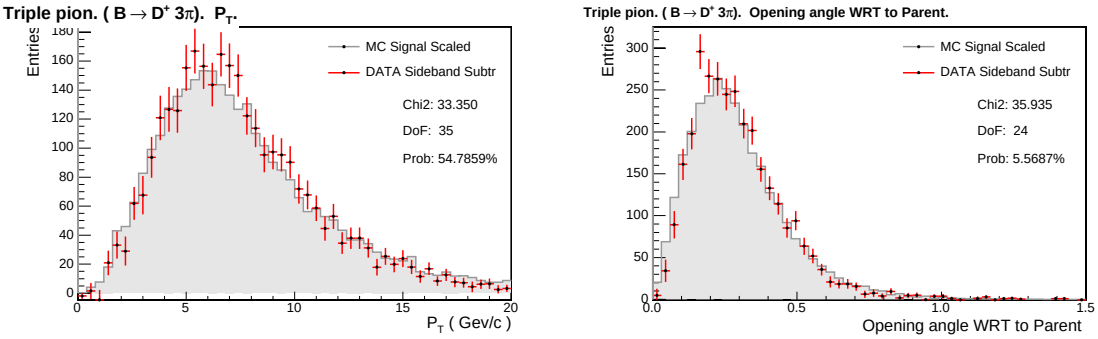

Figure B-9: p_T of the 3π treated as a resonance and an opening angle of such a resonance with respect to B^0 meson..

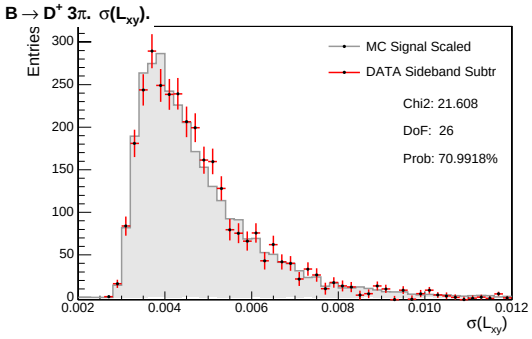

Figure B-10: $\sigma(L_{xy})$ of B^0 meson.

B.2 Optimization Plots

The final values of the selection cuts are chosen with the help of the optimization procedure. In short: we apply a set of selection cuts, fit the combinatorial background in the data, extrapolate it under the signal, calculate the expected significance, and repeat the sequence with another set of selection cuts. To integrate the signals we use the region equivalent of the two standard deviations of the effective signal width.

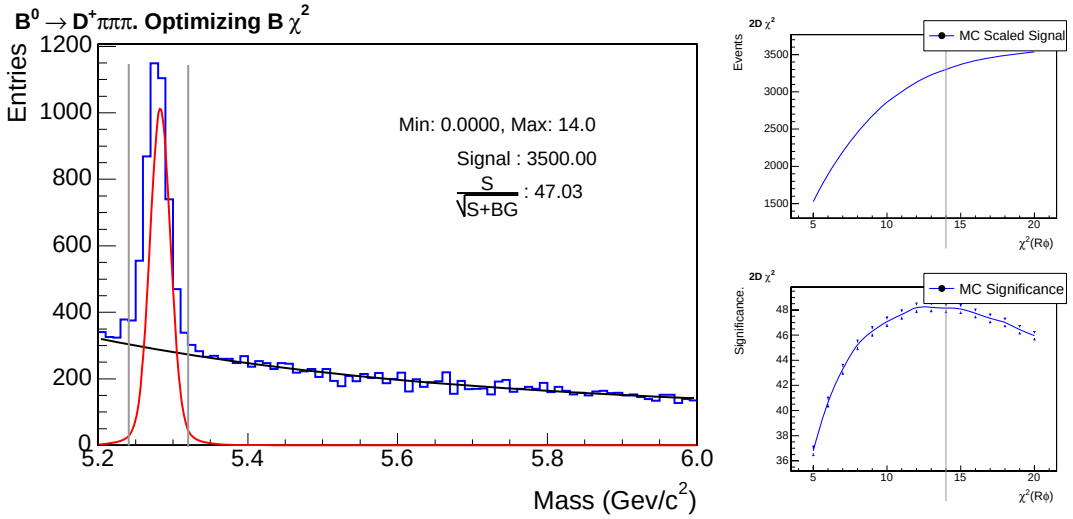

Figure B-11: A snapshot of the optimization process for χ^2 of the B^0 meson vertex fit for $B^0 \to D^-\pi^+\pi^+\pi^-$ mode (left). Grey lines show the region used to calculate the signal significance. The output of the optimization procedure for the same selection cut is on the right with efficiency curve on top and significance curve on the bottom. The gray line shows the default cut value.

Modes with high statistics are optimized with respect to Gaussian significance using the number of signal and background events in the signal region

$$S(\mathcal{G}) = \frac{N_{\text{signal}}}{\sqrt{(N_{\text{signal}} + N_{\text{background}})}}. \tag{B.1}$$

For $B_s^0 \to D_s^- D_s^+$ modes, we use a parametrized significance for low statistics modes [44]. The prescription effectively adds a constant term to the background to avoid unrealistically high values of significance for an empty background.

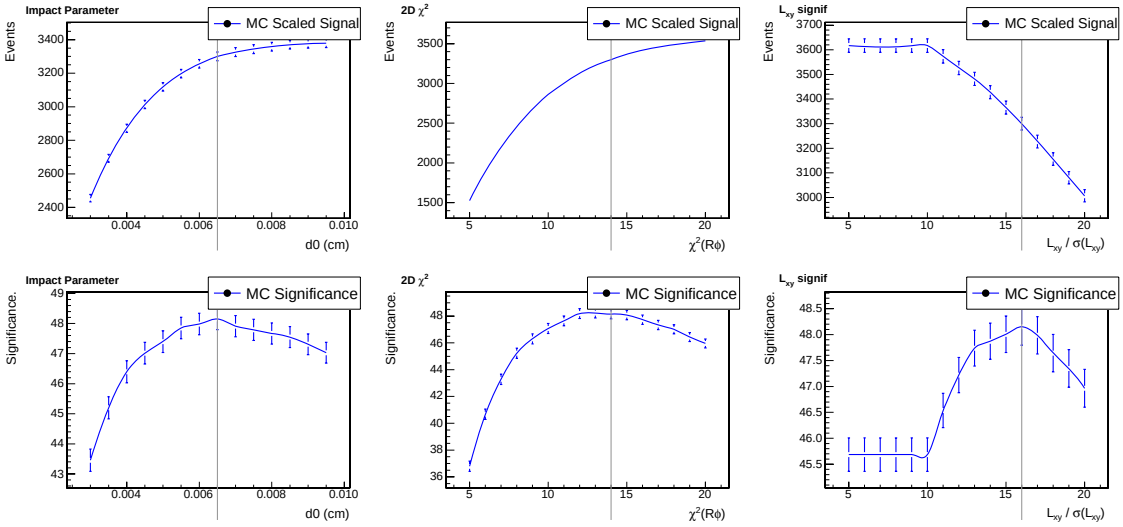

Figure B-12: Cut optimization plots for $B^0 \to D^-\pi^+\pi^+\pi^-$ mode. L_{xy} of the B^0, impact parameter of the B^0, and $\chi^2_{R\phi}$ of the B^0.

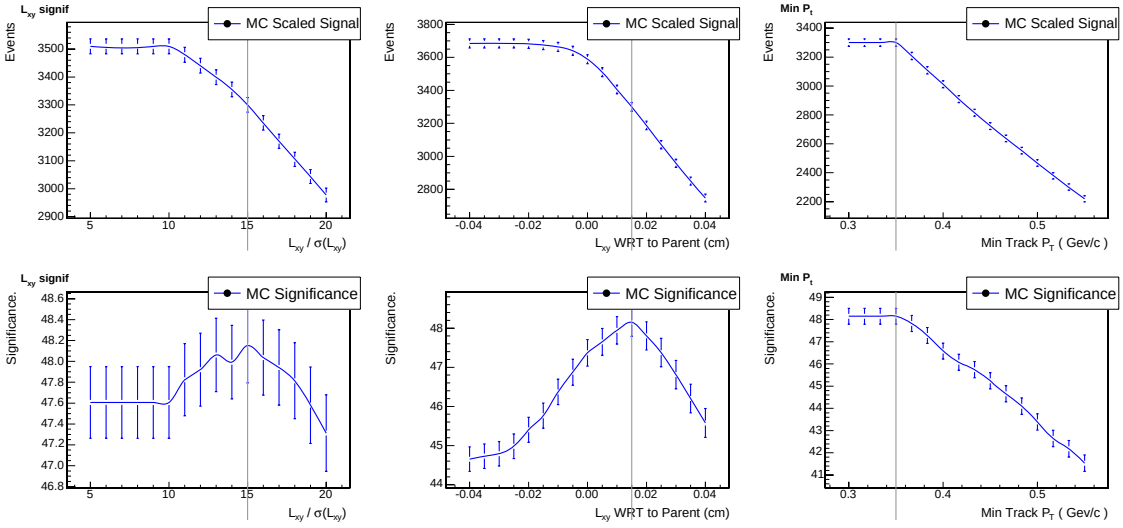

Figure B-13: Cut optimization plots for $B^0 \to D^-\pi^+\pi^+\pi^-$ mode. $L_{xy}/\sigma(L_{xy})$ of the D^-, L_{xy} of the D^- with respect to B^0 and minimum p_T of the track.

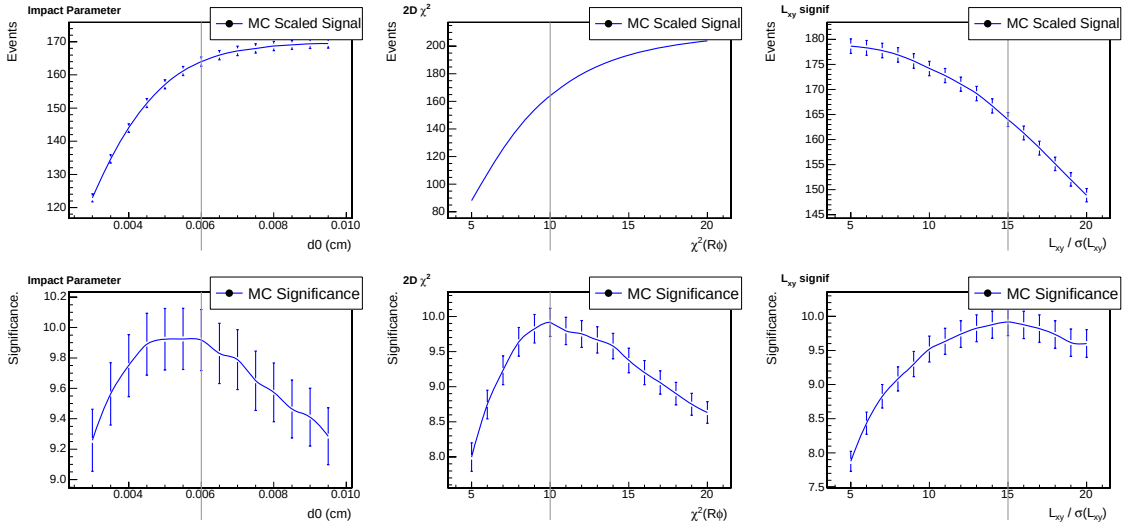

Figure B-14: Cut optimization plots for $B_s^0 \to D_s^-(\phi\pi^-)\pi^+\pi^+\pi^-$ mode. $L_{xy}/\sigma(L_{xy})$ significance of the B^0, impact parameter of the B^0, and $\chi^2_{R\phi}$ of the B^0.

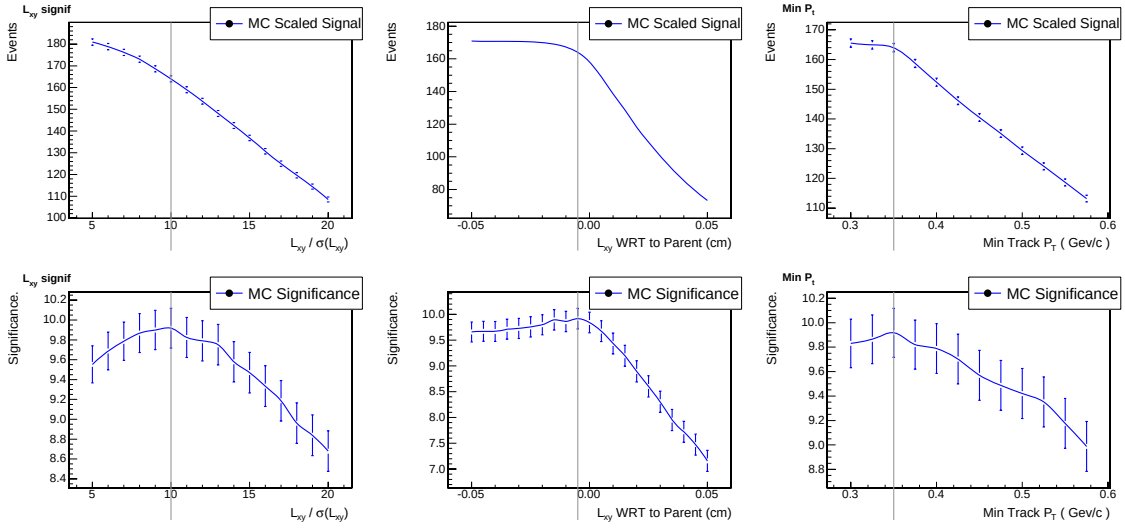

Figure B-15: Cut optimization plots for $B_s^0 \to D_s^-(\phi\pi^-)\pi^+\pi^+\pi^-$ mode. $L_{xy}/\sigma(L_{xy})$ of the D^-, L_{xy} of the D^- with respect to B_s^0 and minimum p_T of the track.

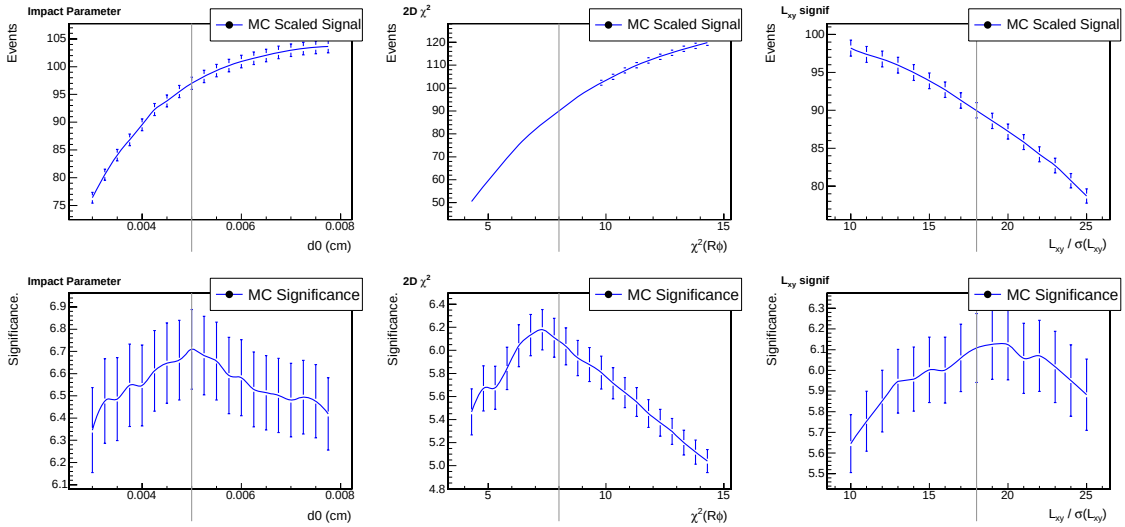

Figure B-16: Cut optimization plots for $B_s^0 \rightarrow D_s^-(K^{*0}K^-)\pi^+\pi^+\pi^-$ mode. $L_{xy}/\sigma(L_{xy})$ of the B_s^0, impact parameter of the B_s^0, and $\chi^2_{R\phi}$ of the B_s^0 for B_CHARM and LOWPT combined .

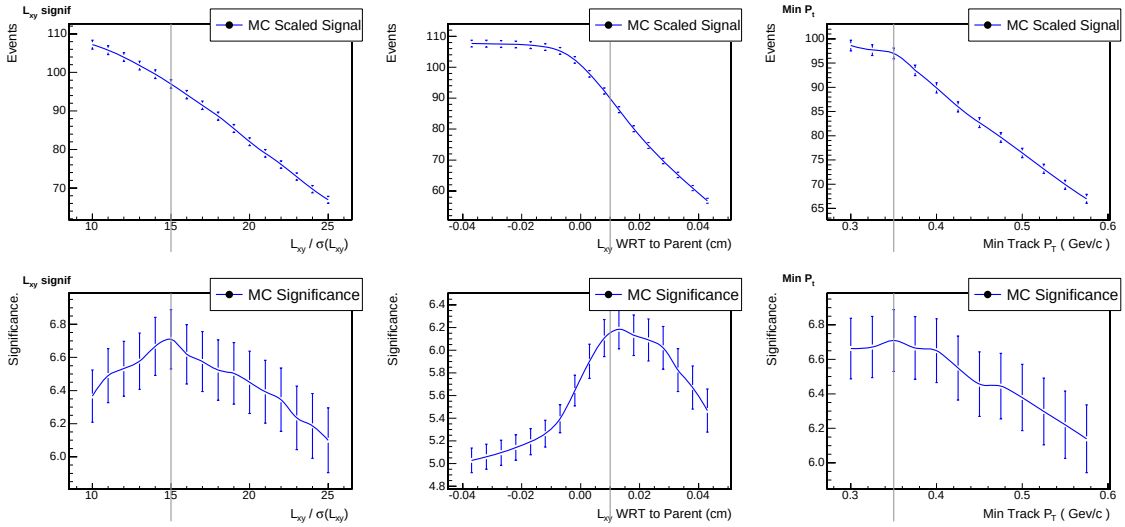

Figure B-17: Cut optimization plots for $B_s^0 \rightarrow D_s^-(K^{*0}K^-)\pi^+\pi^+\pi^-$ mode. $L_{xy}/\sigma(L_{xy})$ of the D^-, L_{xy} of the D^- with respect to B_s^0 and minimum p_T of the track.

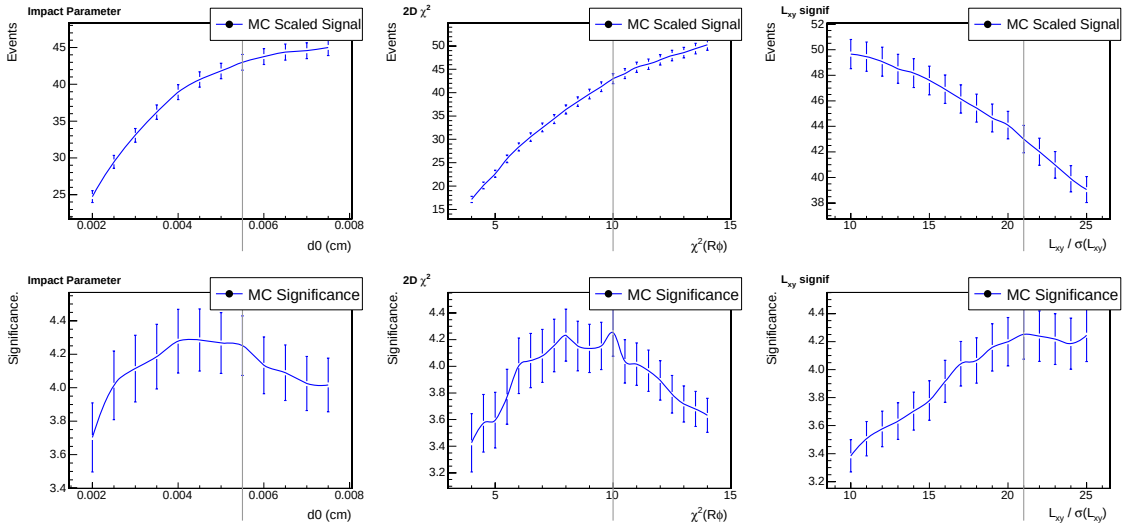

Figure B-18: Cut optimization plots for $B_s^0 \rightarrow D_s^-(\pi^+\pi^-\pi^-)\pi^+\pi^+\pi^-$ mode. $L_{xy}/\sigma(L_{xy})$ of the B_s^0, impact parameter of the B_s^0, and $\chi^2_{R\phi}$ of the B_s^0.

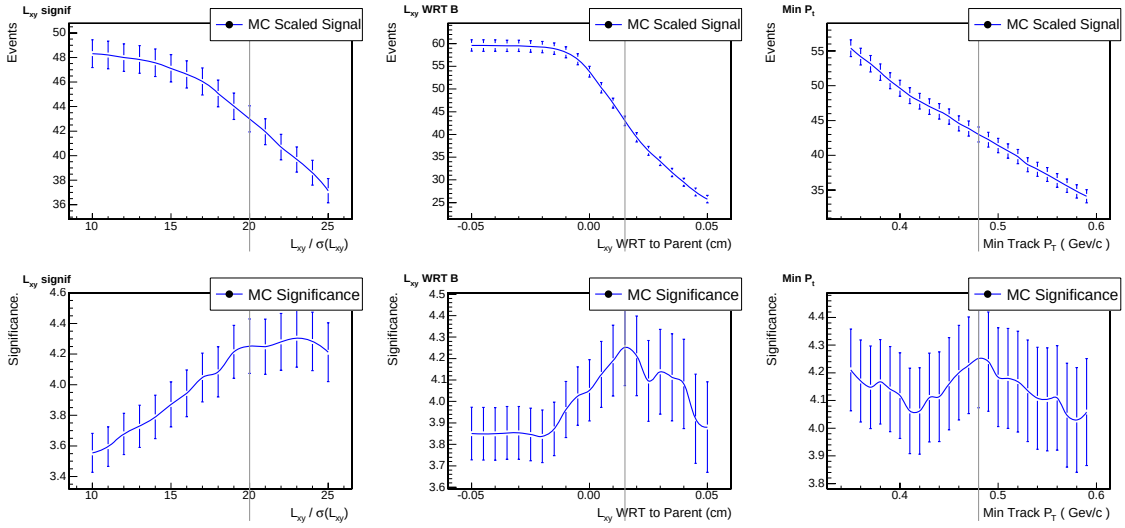

Figure B-19: Cut optimization plots for $B_s^0 \rightarrow D_s^-(\pi^+\pi^-\pi^-)\pi^+\pi^+\pi^-$ mode. $L_{xy}/\sigma(L_{xy})$ of the D^-, L_{xy} of the D^- with respect to B_s^0 and minimum p_T of the track.

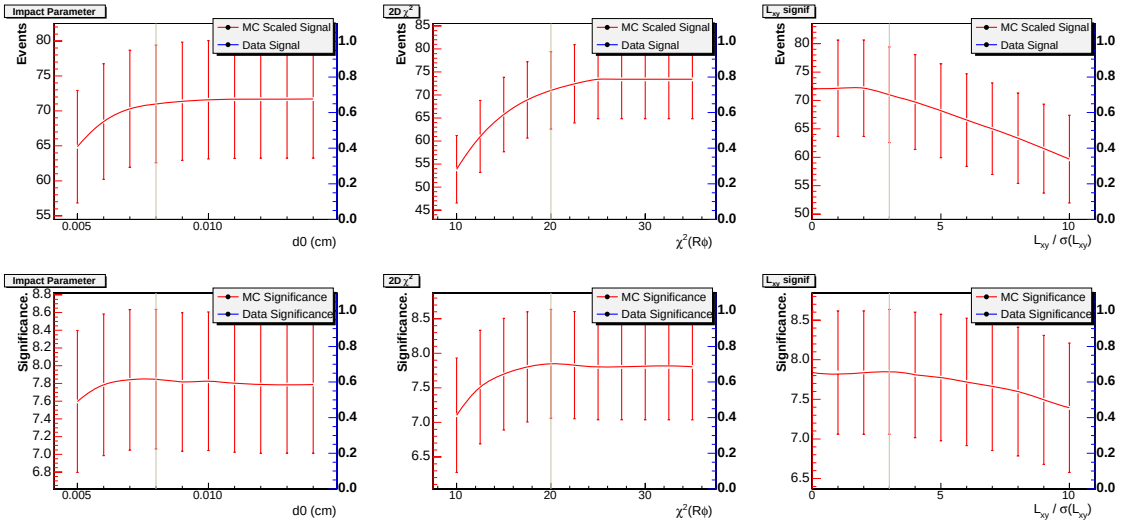

Figure B-20: Cut optimization plots for $B^0 \to D^- D_s^+(\phi\pi^+)$ mode. $L_{xy}/\sigma(L_{xy})$ of the B^0, impact parameter of the B^0, and $\chi^2_{R\phi}$ of the B^0.

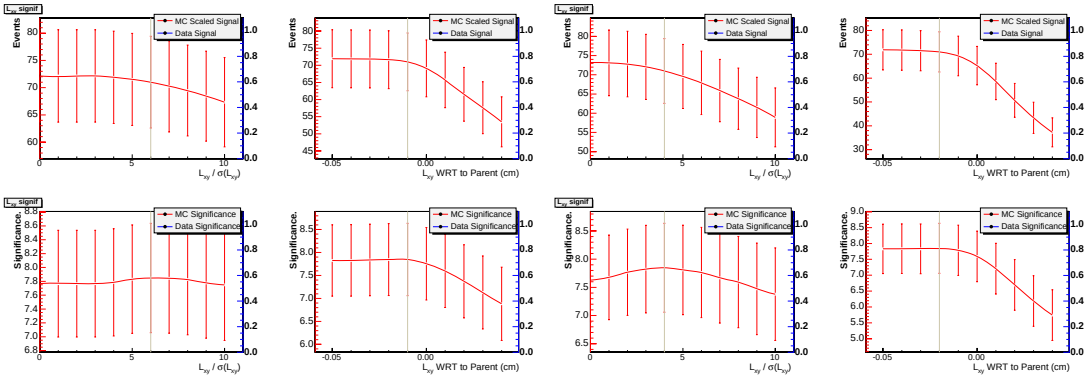

Figure B-21: Cut optimization plots for $B^0 \to D^- D_s^+(\phi\pi^+)$ mode. $L_{xy}/\sigma(L_{xy})$ of the D^-, L_{xy} of the D^- with respect to B^0, $L_{xy}/\sigma(L_{xy})$ of the D_s, L_{xy} of the D_s with respect to B^0.

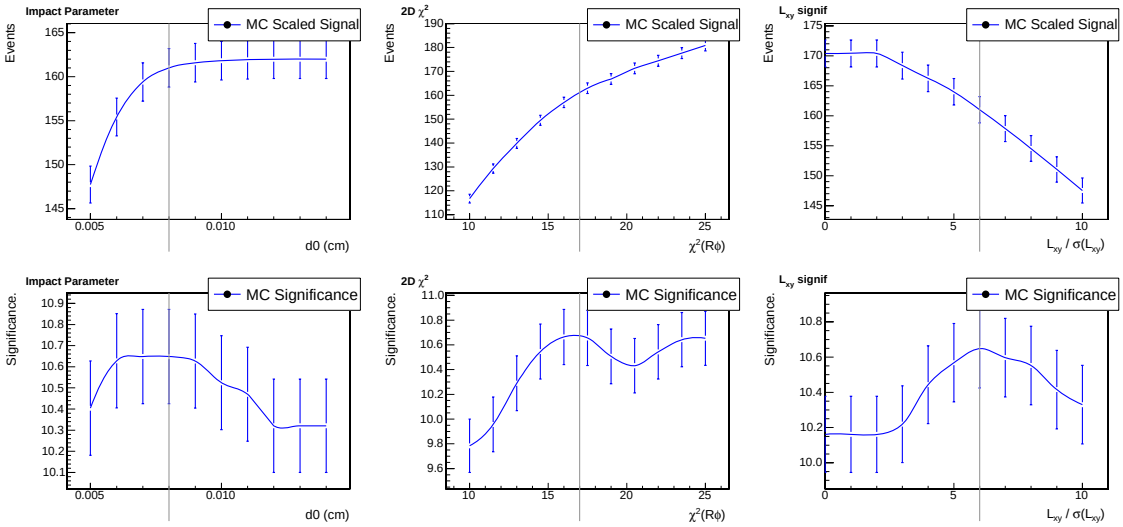

Figure B-22: Cut optimization plots for $B^0 \to D^- D_s^+ (K^{*0} K^+)$ mode. $L_{xy}/\sigma(L_{xy})$ of the B^0, impact parameter of the B^0, and $\chi^2_{R\phi}$ of the B^0 .

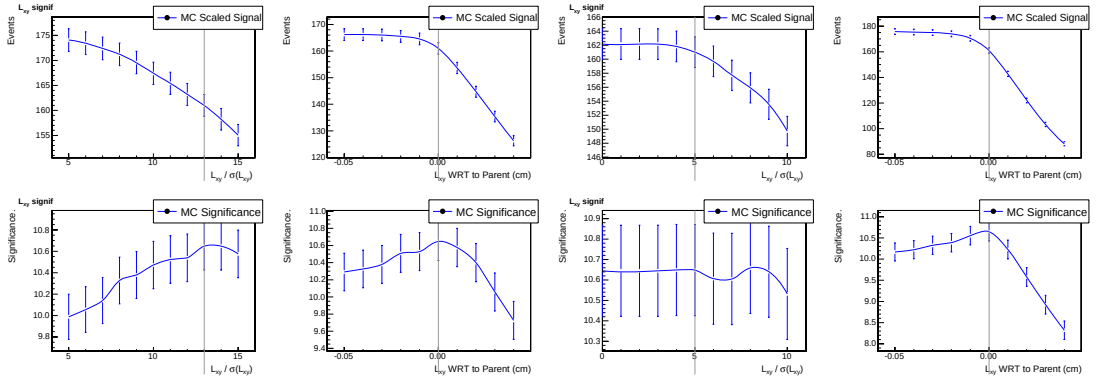

Figure B-23: Cut optimization plots for $B^0 \to D^- D_s^+ (K^{*0} K^+)$ mode. $L_{xy}/\sigma(L_{xy})$ of the D^-, L_{xy} of the D^- with respect to B^0, $L_{xy}/\sigma(L_{xy})$ of the D_s, L_{xy} of the D_s with respect to B^0.

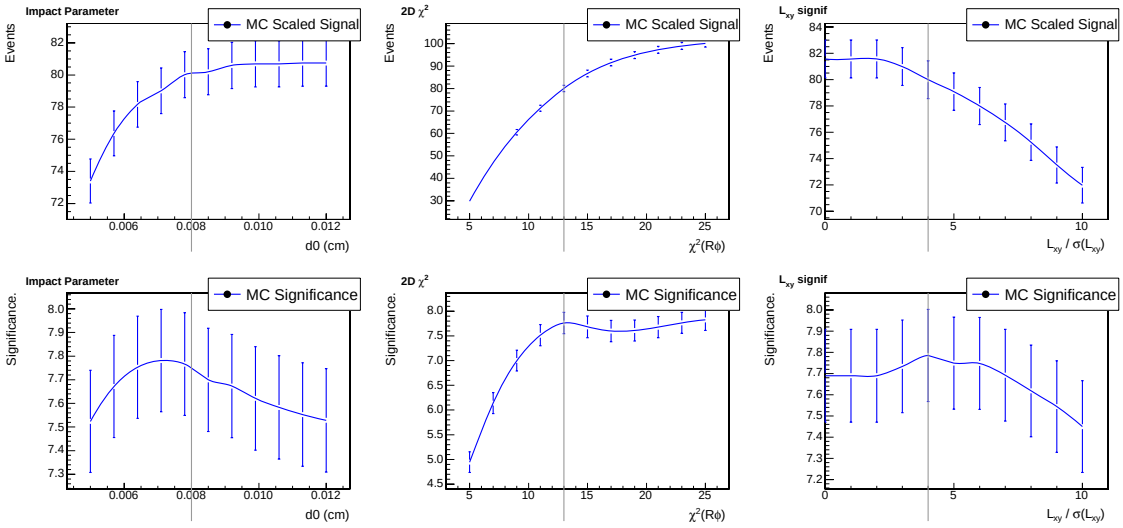

Figure B-24: Cut optimization plots for $B^0 \to D^- D_s^+(\pi^+\pi^+\pi^-)$ mode. $L_{xy}/\sigma(L_{xy})$ of the B^0, impact parameter of the B^0, and $\chi^2_{R\phi}$ of the B^0.

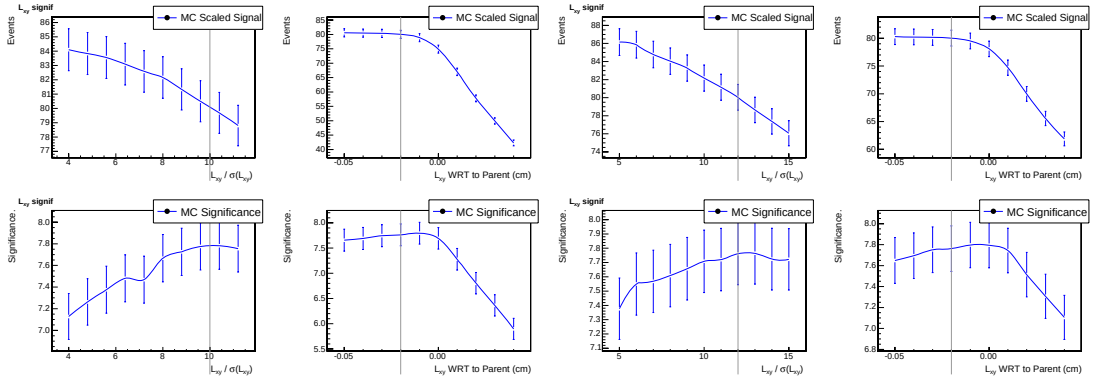

Figure B-25: Cut optimization plots for $B^0 \to D^- D_s^+(\pi^+\pi^+\pi^-)$ mode. $L_{xy}/\sigma(L_{xy})$ of the D^-, L_{xy} of the D^- with respect to B^0, $L_{xy}/\sigma(L_{xy})$ of the D_s, L_{xy} of the D_s with respect to B^0.

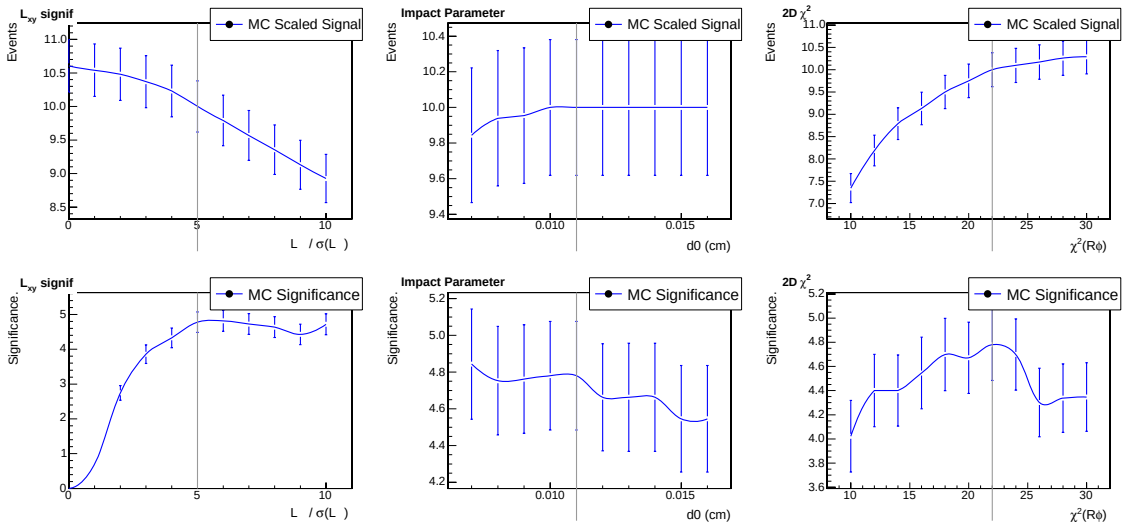

Figure B-26: Cut optimization plots for $B_s^0 \to D_s^-(\phi\pi^-)D_s^+(\phi\pi^+)$ mode. $L_{xy}/\sigma(L_{xy})$ of the B, impact parameter of the B_s^0, and $\chi^2_{R\phi}$ of the B_s^0

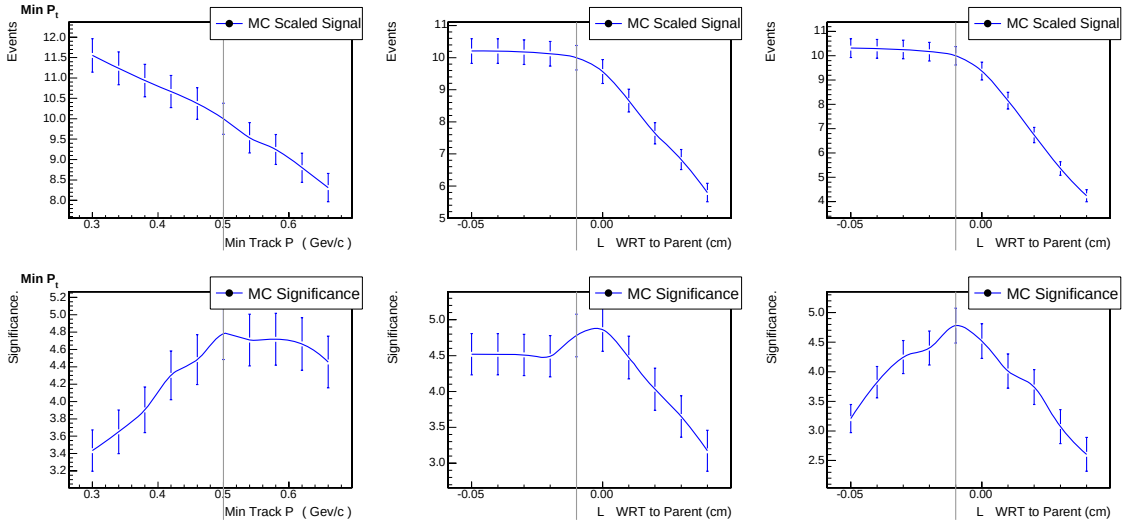

Figure B-27: Cut optimization plots for $B_s^0 \to D_s^-(\phi\pi^-)D_s^+(\phi\pi^+)$ mode. Min p_T of the track, L_{xy} of the first D_s with respect to B_s^0, L_{xy} of the second D_s with respect to B_s^0.

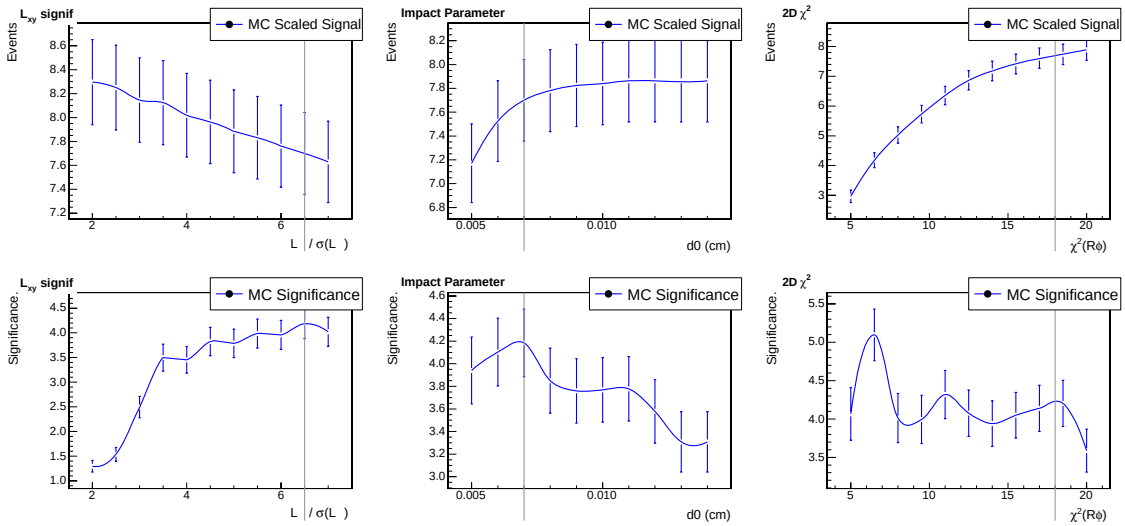

Figure B-28: Cut optimization plots for $B_s^0 \rightarrow D_s^-(\phi\pi^-)D_s^+(K^{*0}K^+)$ mode. $L_{xy}/\sigma(L_{xy})$ of the B_s^0, impact parameter of the B_s^0, and $\chi^2_{R\phi}$ of the B_s^0.

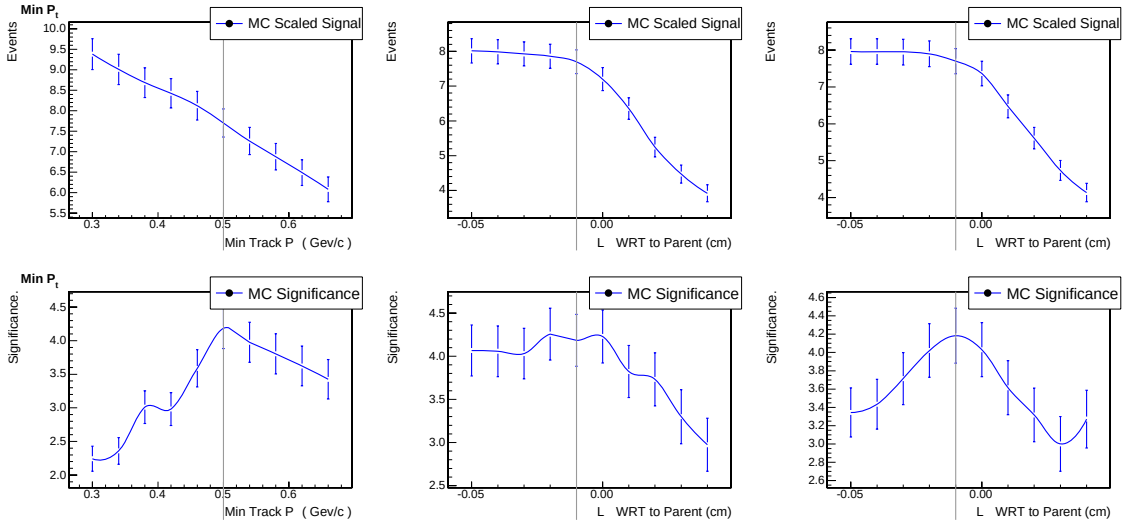

Figure B-29: Cut optimization plots for $B_s^0 \rightarrow D_s^-(\phi\pi^-)D_s^+(K^{*0}K^+)$ mode. Min p_T of the track, L_{xy} of the first D_s with respect to B_s^0, L_{xy} of the second D_s with respect to B_s^0.

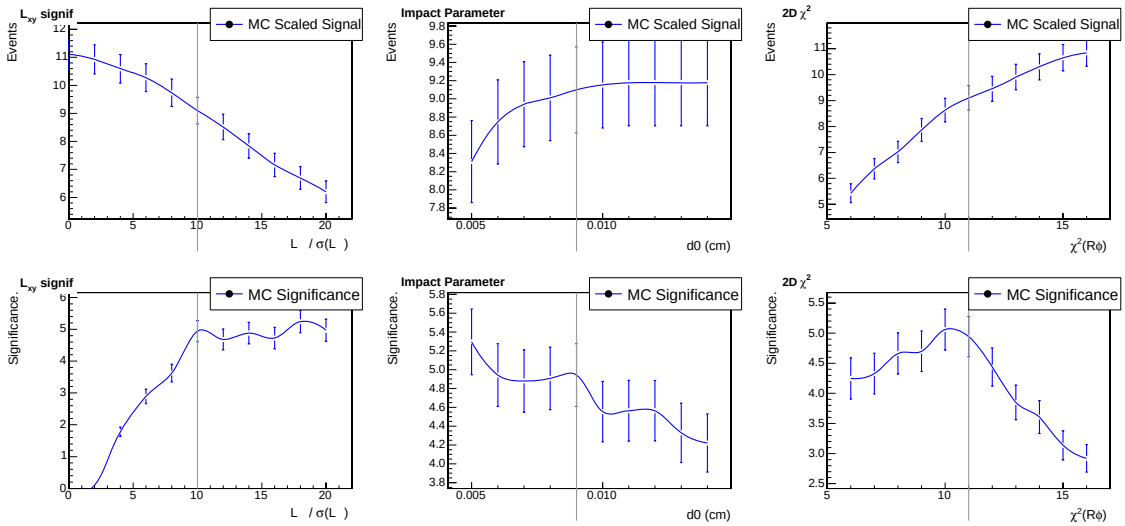

Figure B-30: Cut optimization plots for $B_s^0 \rightarrow D_s^-(\phi\pi^-)D_s^+(\pi^+\pi^+\pi^-)$ mode. $L_{xy}/\sigma(L_{xy})$ of the B_s^0, impact parameter of the B_s^0, and $\chi^2_{R\phi}$ of the B_s^0.

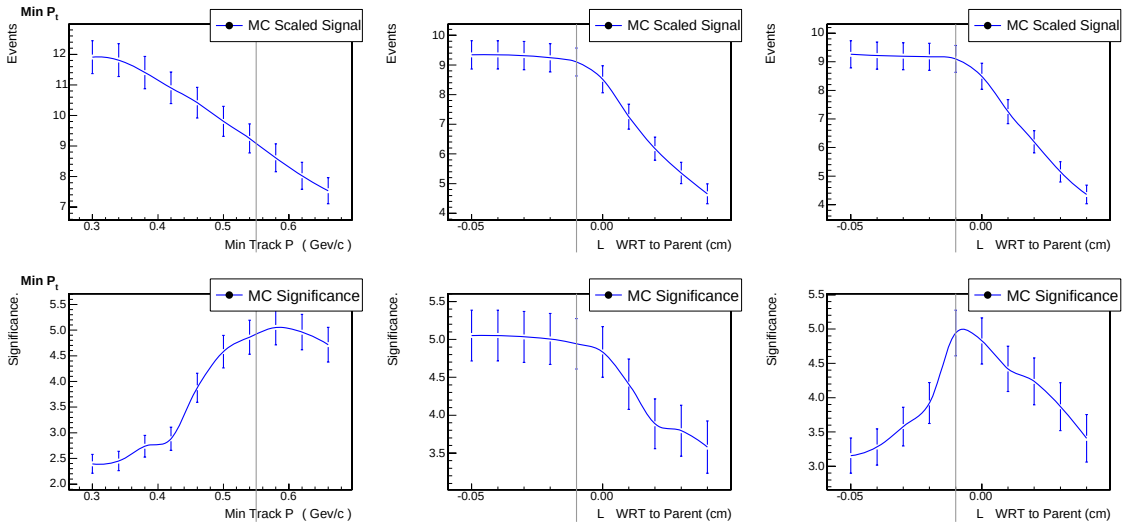

Figure B-31: Cut optimization plots for $B_s^0 \rightarrow D_s^-(\phi\pi^-)D_s^+(\pi^+\pi^+\pi^-)$ mode. Min p_T of the track, L_{xy} of the first D_s with respect to B_s^0, L_{xy} of the second D_s with respect to B_s^0.

B.3 Templates

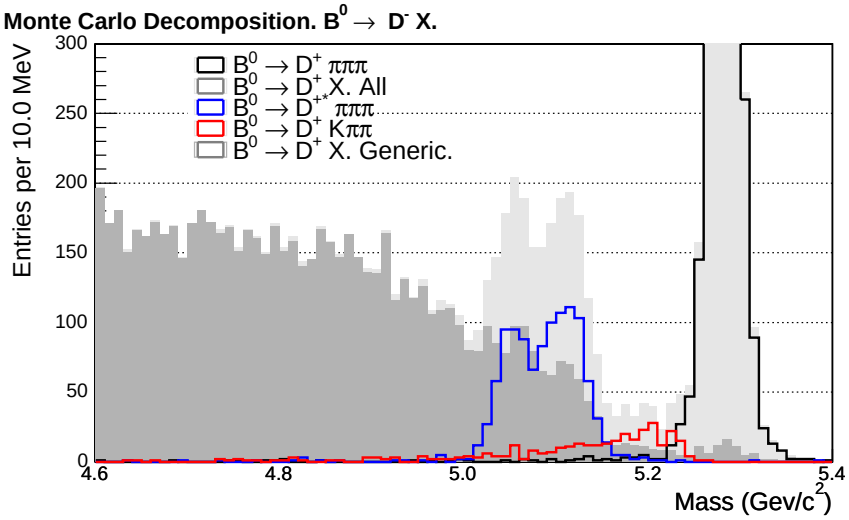

Figure B-32: The decomposition of the semi-generic $B^0 \to D^-\pi^+\pi^+\pi^-$ Monte Carlo simulation into the signal, Cabibbo suppressed part, $B^0 \to D^{*-}\pi^+\pi^+\pi^-$ reflection, and generic background.

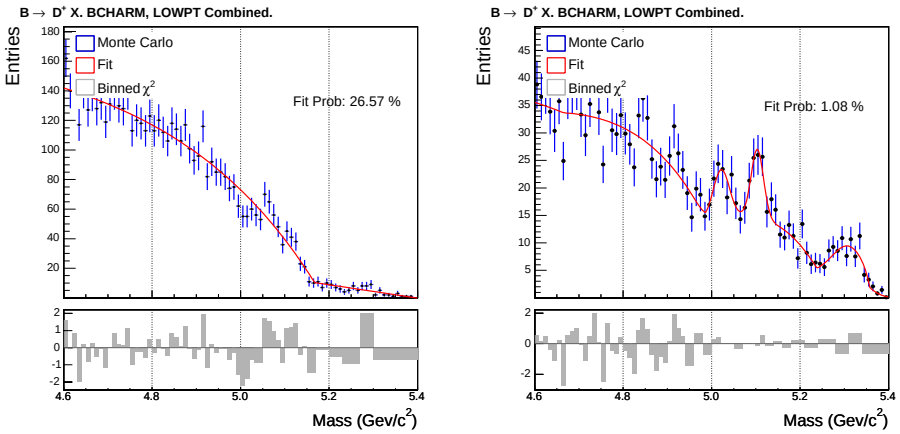

Figure B-33: Templates for the generic background used in $B^0 \to D^-\pi^+\pi^+\pi^-$ fit.

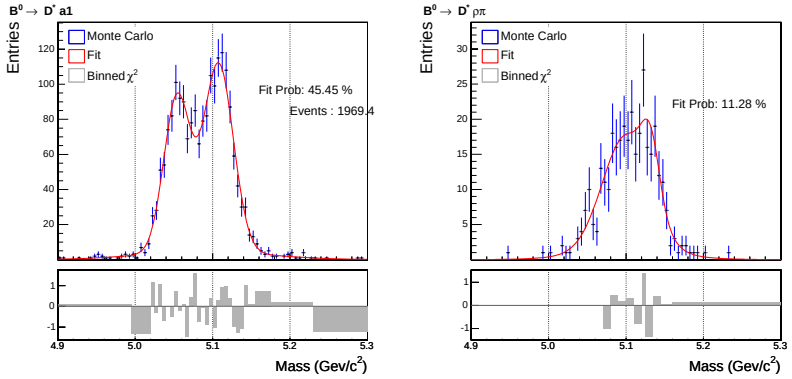

Figure B-34: Templates for $B^0 \to D^* a_1$ and $B^0 \to D^* \rho\pi$ used to fit $B^0 \to D^- 3\pi$.

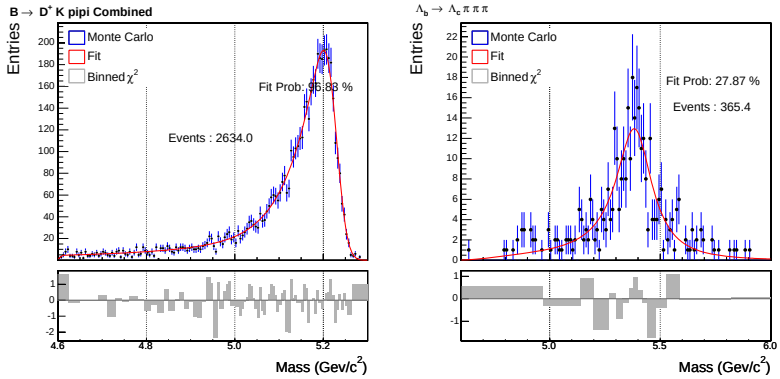

Figure B-35: Templates for Cabibbo suppressed B^0 meson decays and $\Lambda_b \to \Lambda_c \pi\pi\pi$ used to fit $B^0 \to D^- \pi^+ \pi^+ \pi^-$.

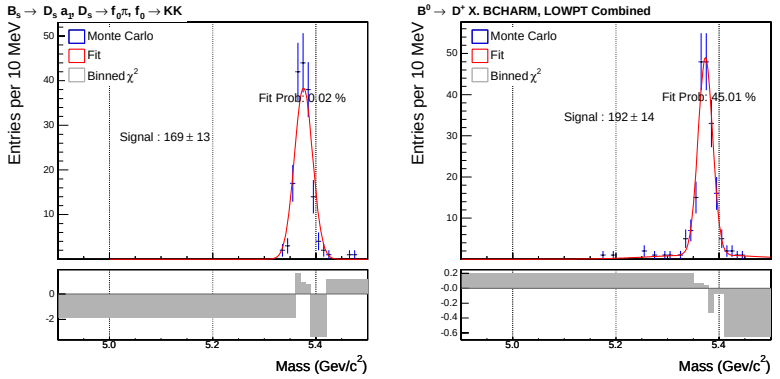

Figure B-36: Crosstalk templates for $B_s^0 \to D_s^-(\phi\pi^-)\pi^+\pi^+\pi^-$ and $B_s^0 \to D_s^-(K^{*0}K^-)\pi^+\pi^+\pi^-$.

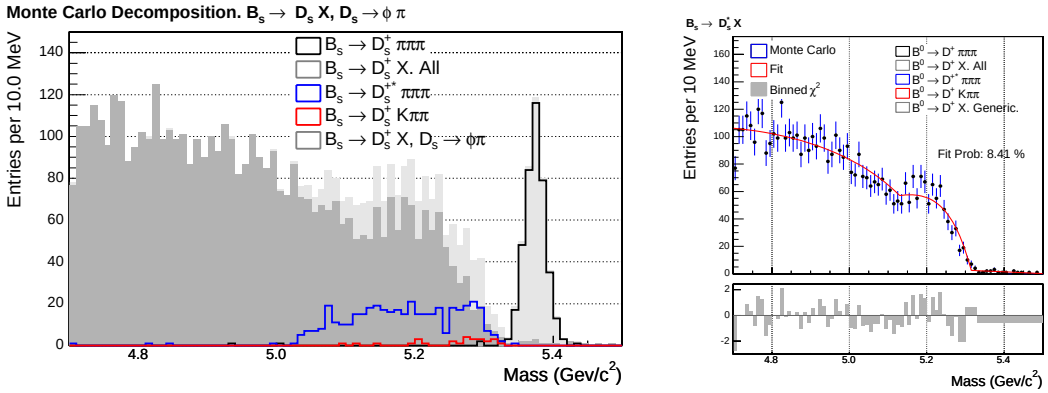

Figure B-37: Background decomposition and generic background template for $B_s^0 \to D_s^-(\phi\pi^-)\pi^+\pi^+\pi^-$ mode.

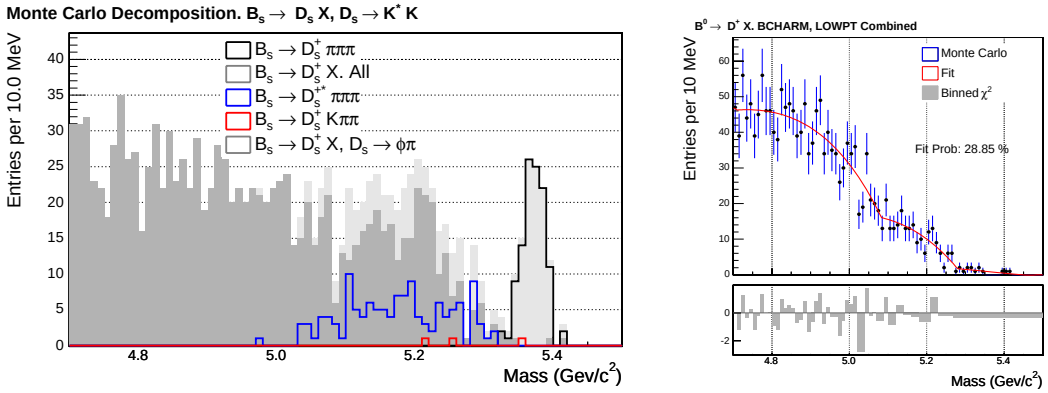

Figure B-38: Background decomposition and generic background template for $B_s^0 \to D_s^-(K^{*0}K^-)\pi^+\pi^+\pi^-$ mode.

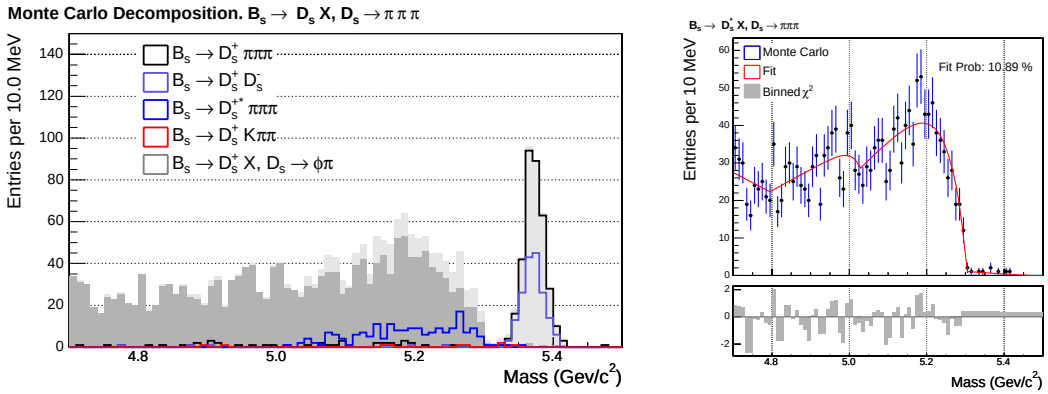

Figure B-39: Background decomposition and generic background template for $B_s^0 \to D_s^-(\pi^+\pi^-\pi^-)\pi^+\pi^+\pi^-$mode.

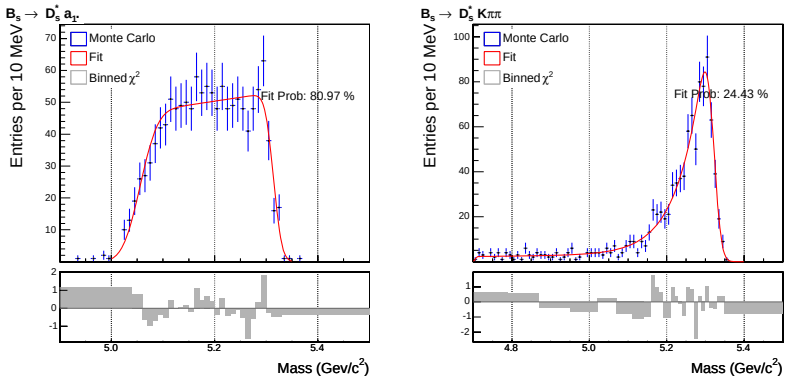

Figure B-40: $B_s^0 \to D_s^{*-}\pi^+\pi^-\pi^-$ template and Cabibbo supressed B_s^0 meson decay template for $B_s^0 \to D_s^-(\phi\pi^-)\pi^+\pi^+\pi^-$ mode.

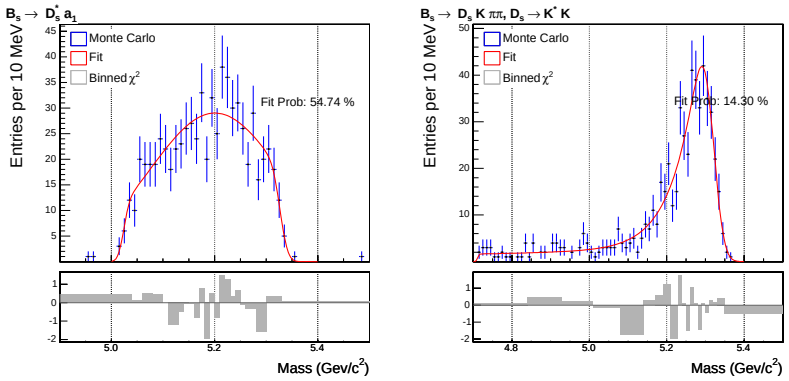

Figure B-41: $B_s^0 \to D_s^{*-}\pi^+\pi^-\pi^-$ template and Cabibbo supressed B_s^0 meson decay template for $B_s^0 \to D_s^-(K^{*0}K^-)\pi^+\pi^+\pi^-$ mode.

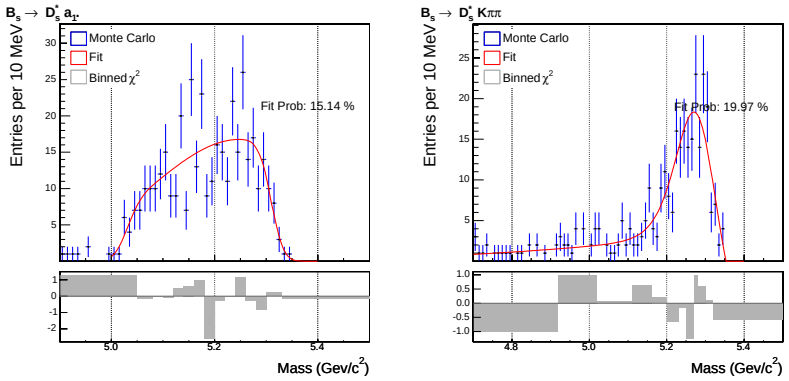

Figure B-42: $B_s^0 \to D_s^{*-}\pi^+\pi^-\pi^-$ template and Cabibbo supressed B_s^0 meson decay template for $B_s^0 \to D_s^-(\pi^+\pi^-\pi^-)\pi^+\pi^+\pi^-$ mode.

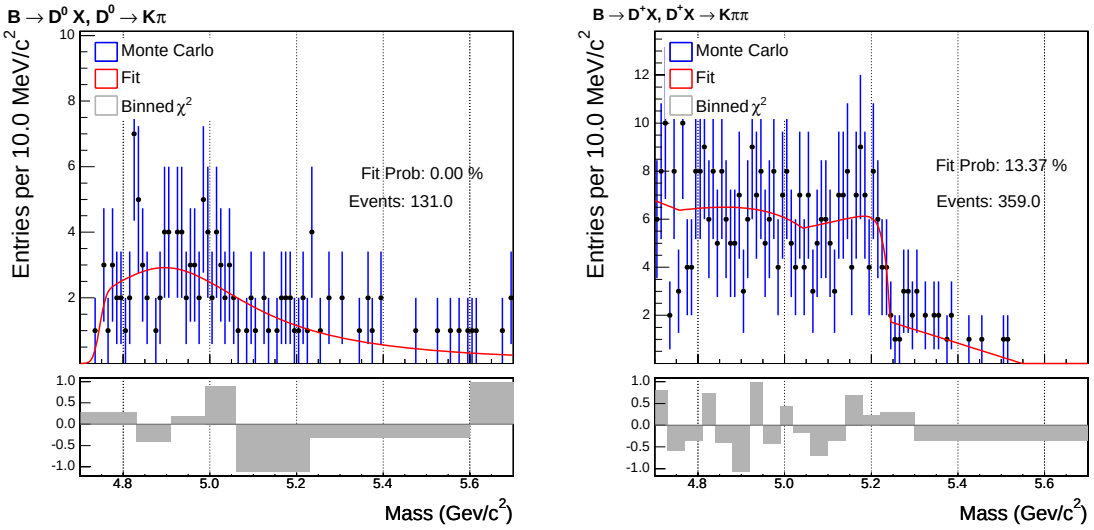

Figure B-43: $B \to D^0 X, D^0 \to K\pi$ and $B \to D^- X, D^- \to K^+\pi^-\pi^-$ semi-generic templates for $B_s^0 \to D_s^-(K^{*0}K^-)\pi^+\pi^+\pi^-$ mode. $B^0 \to D^-\pi^+\pi^+\pi^-$ is removed.

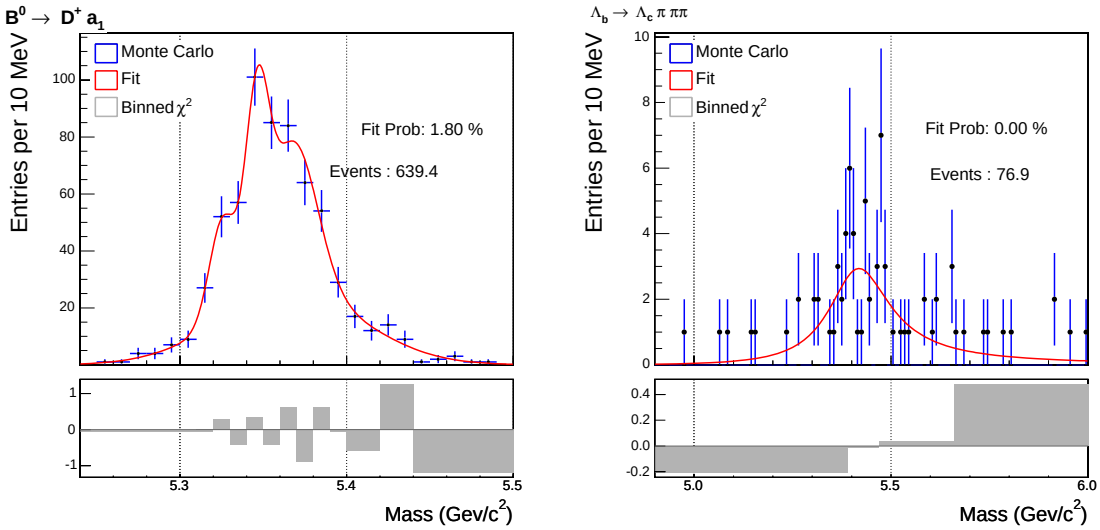

Figure B-44: $B^0 \to D^-\pi^+\pi^+\pi^-$ and $\Lambda_b \to \Lambda_c\pi^+\pi^+\pi^-$ templates for $B_s^0 \to D_s^-(K^{*0}K^-)\pi^+\pi^+\pi^-$ mode.

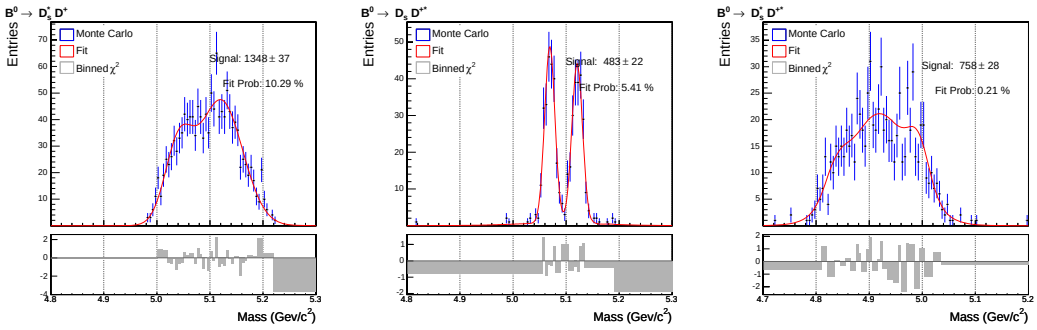

Figure B-45: $B^0 \to D_s^{(*)-} D^{(*)+}$ templates for $B^0 \to D^- D_s^+ (\phi\pi^+)$ mode.

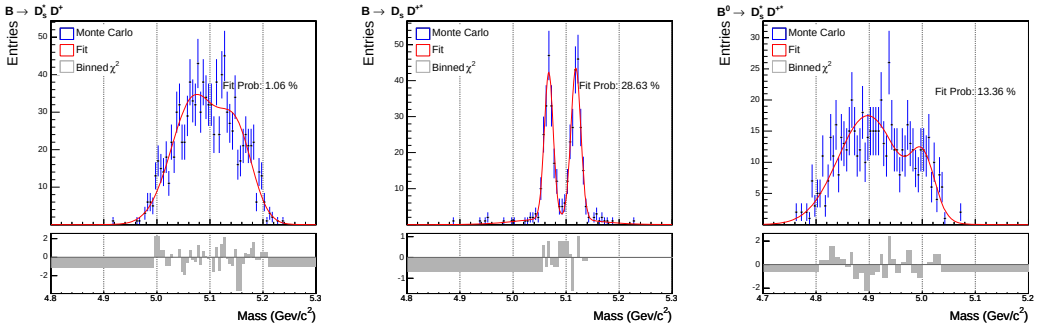

Figure B-46: $B^0 \to D_s^{(*)-} D^{(*)+}$ templates for $B^0 \to D^- D_s^+ (K^{*0} K^+)$ mode.

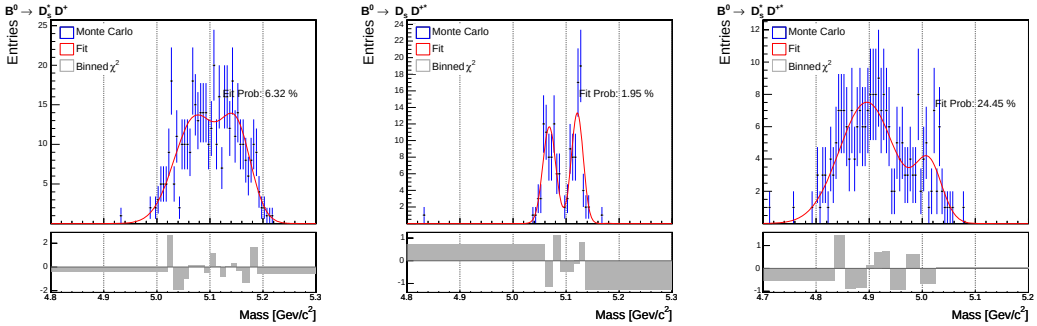

Figure B-47: $B^0 \to D_s^{(*)-} D^{(*)+}$ templates for $B^0 \to D^- D_s^+ (\pi^+\pi^+\pi^-)$ mode.

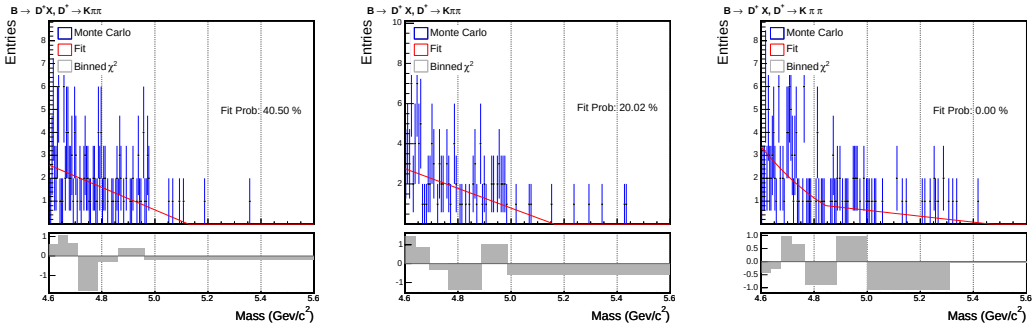

Figure B-48: $B^0 \to D^-(K^+\pi^-\pi^-)X$ templates for $B^0 \to D^- D_s^+$ modes.

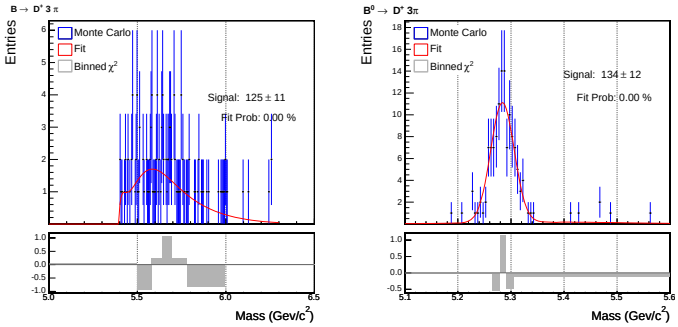

Figure B-49: $B^0 \to D^-\pi^+\pi^+\pi^-$ templates for $B^0 \to D^- D_s^+(\phi\pi^+)$ and $B^0 \to D^- D_s^+(K^{*0}K^+)$ modes.

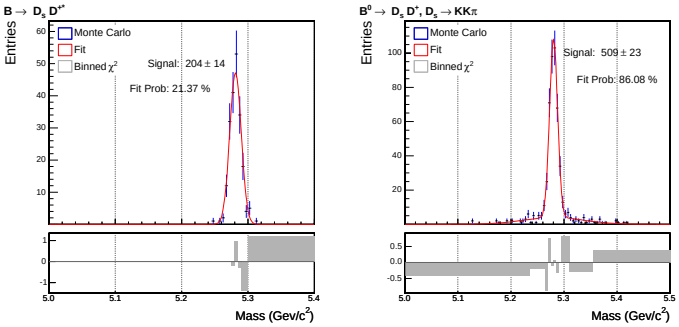

Figure B-50: Crosstalk templates for $B^0 \to D^- D_s^+(\phi\pi^+)$ and $B^0 \to D^- D_s^+(K^{*0}K^+)$ modes.

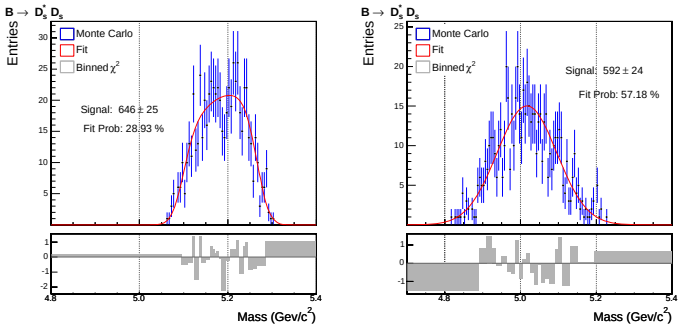

Figure B-51: $B_s^0 \to D_s^{(*)-} D_s^{(*)+}$ templates for $B_s^0 \to D_s^-(\phi\pi^-)D_s^+(\phi\pi^+)$ mode.

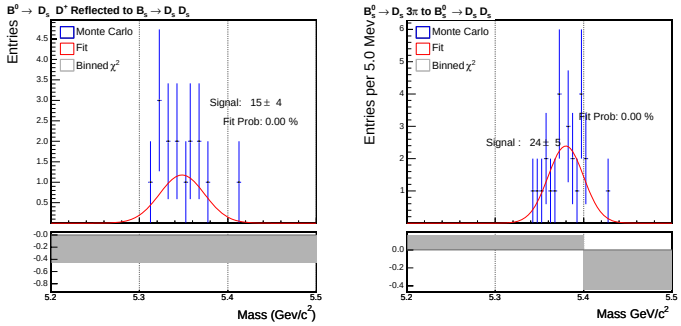

Figure B-52: $B^0 \to D^- D_s^+(\phi\pi^+)$ template for $B_s^0 \to D_s^-(\phi\pi^-)D_s^+(K^{*0}K^+)$ mode and $B_s^0 \to D_s^-(\pi^+\pi^-\pi^-)\pi^+\pi^+\pi^-$ template for $B_s^0 \to D_s^-(\phi\pi^-)D_s^+(\pi^+\pi^+\pi^-)$ mode.

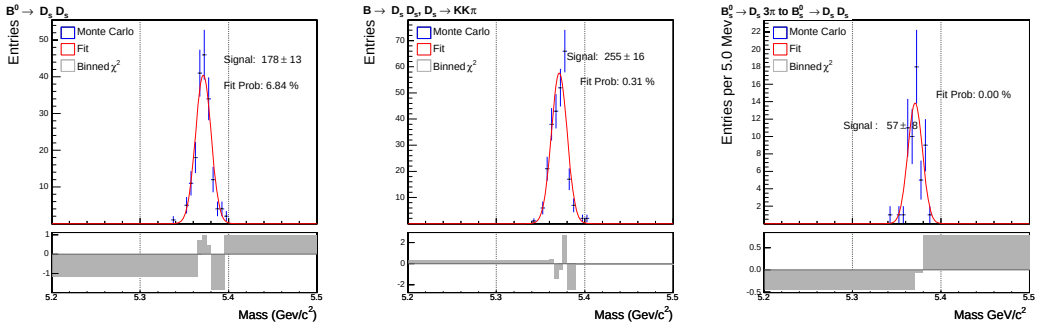

Figure B-53: $B_s^0 \to D_s^+(\phi\pi^-)D_s^-(K^+K^-\pi^-)$ templates for $B_s^0 \to D_s^-(\phi\pi^-)D_s^+(\phi\pi^+)$, $B_s^0 \to D_s^-(\phi\pi^-)D_s^+(K^{*0}K^+)$ and $B_s^0 \to D_s^-(\phi\pi^-)D_s^+(\pi^+\pi^+\pi^-)$ modes.

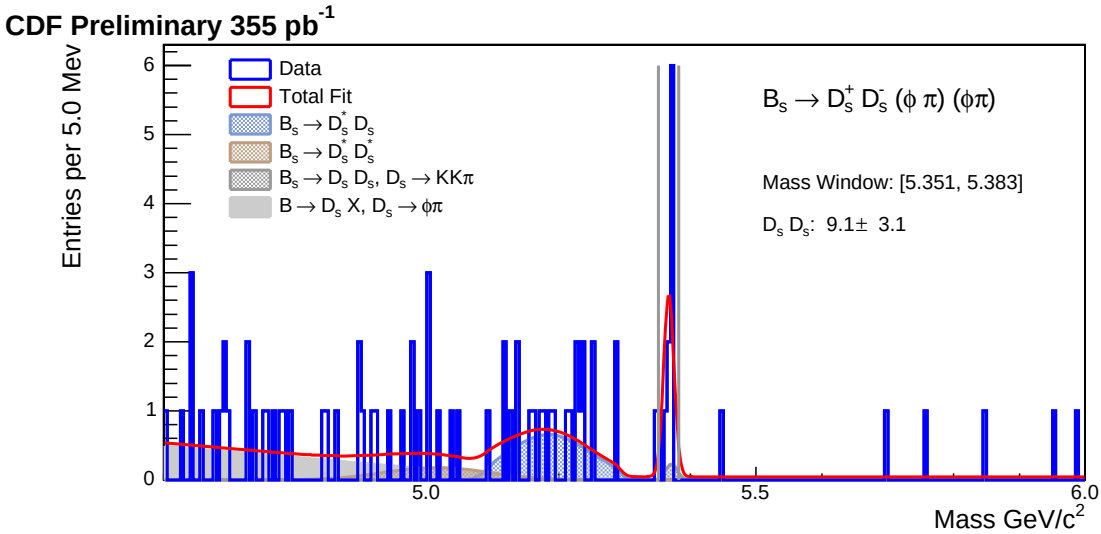

Figure B-54: Reconstructed $B_s^0 \to D_s^-(\phi\pi^-)D_s^+(\phi\pi^+)$ mass distribution with fitted $B_s^0 \to D_s^{(*)-} D_s^{(*)+}$ signals.

Bibliography

[1] W.-M. Yao *et al.,* [Particle Data Group], Journal of Physics **G 33**, 1 (2006).

[2] See, for example, F. Halzen, A. Martin, *Quarks and Leptons*, (1984).

[3] See for example S. Weinberg, *The Quantum Theory of Fields*, (2000).

[4] D. Acosta *et al.,* [CDF Collaboration], *Pentaquark searches at CDF*, arxiv:hep-ex/0408025.

[5] See for example K.S. Thorn *Gravitation* (2000).

[6] See for example J. Schwinger, *Quantum Mechanics*, Dover Publications Inc., New York (1958).

[7] D.J. Gross and F. Wilczek, Phys. Rev. Lett. **30**, 1343 (1973);
H.D. Pollitzer, Phys. Rev. Lett. **30**, 1346 (1973).

[8] G. Arniston *et al.*, [UA1 Collaboration], Phys. Lett. **B 122**, 103 (1983).
P. Bagnaia *et al.*, [UA2 Collaboration], Phys. Lett. **B 122**, 476 (1983).

[9] G. Arniston *et al.*, [UA1 Collaboration], Phys. Lett. **B 126**, 398 (1983).
P. Bagnaia *et al.*, [UA2 Collaboration], Phys. Lett. **B 129**, 130 (1983).

[10] N. Cabibbo, Phys. Rev. Lett. **10**, 531 (1963).
M. Kobayashi and T. Masakawa, Prog. Theor. Phys. **49**, 652 (1973).

[11] L. Wolfenstein, Phys. Rev. Lett. **51**, 1915 (1983).

[12] L.L. Chau and W.Y. Keung, Phys. Rev. Lett. **53**, 1802 (1984).

[13] D. Acosta *et al.,* [CDF Collaboration], Phys. Rev. Lett. 97, 242003 (2006).

[14] I. Dunietz, R. Fleischer, U. Nierste, Phys. Rev. **D63**, 114015 (2001).

[15] R. Barate *et al.*, [ALEPH Collaboration] Phys. Lett. B **486** 286 (2000).

[16] A. Lenz and U. Nierste, *Theoretical update of* $B_s^0 - \overline{B_s^0}$ *mixing*, arxiv:hep-ph/0612167 (2006).

[17] See for example D.H. Perkins *Introduction to High Energy Physics* (2000).

[18] [Particle Data Group], Phys. Rev. Lett. **10**, 531 (1963).

[19] E. Eichtein and B. Hill, PhysLett. **B 234**, 511 (1990).

[20] A. Abulencia *et al.,* [CDF Collaboration], Phys. Rev. Lett. 96, 191801 (2006).

[21] D. Boutigny *et al.,* `SLAC-R-0457`.

[22] A. Abulencia *et al.,* [CDF Collaboration], Phys. Rev. Lett. 98, 061802, (2007).

[23] P. Colangelo and R. Fernandes, Phys. Lett. B **627**, 77 (2005).

[24] S.W. Herb *et al.*, Phys. Rev. Lett. **39**, 252 (1977).

[25] F. Abe *et al.*, Phys. Rev. Lett. **74**, 2626 (1995).

[26] R. Blair *et al.*, *The CDF-II detector: Technical design report* , FERMILAB-PUB-96/390-E (1996).

[27] T. K. Nelson *et al.*, FERMILAB-CONF-01/357-E.

[28] A. Sill *et al.*, Nucl. Instrum. Meth., **A447**, 1–8 (2000).

[29] T. Affolder *et al.*, Nucl. Instrum. Meth., **A485** , 6–9 (2002).

[30] A. Sill *et al.*, Nucl. Instrum. Meth. **A447**, 1 (2000).

[31] A. Belloni *et al.*, *Event Builder and Level 3 at the CDF Experiment*, FERMILAB-CONF-03/172-E (2003).

[32] E. J. Thomson *et al.*, IEEE Trans. Nucl. Sci **49**, 1063 (2002).

[33] W. Ashmanskas *et al.*, Nucl. Instrum Methods Phys Res. A **447**, 218 (2000), W. Ashmanskas *et al.*, FERMILAB-CONF-02/035-E, A. Bardi *et al.*, Nucl. Instrum Methods Phys Res. A **485**, 6 (2002).

[34] J. Marriner, *Secondary Vertex Fit with Mass and Pointing Constraints (CTVMFT)*, CDF Note 1996 (1993).

[35] A. Cerri, R. Miquel, *Studying the SVT Efficiency and Resolution with J/ψ Data*, CDF Note 5838.

[36] B. Ashmanskas, A. Cerri, see CdfCode browser:
`http://cdfcodebrowser.fnal.gov/CdfCode/source/svtsim/` .

[37] K. Anikeev, P. Murat, Ch. Paus, *Description of Bgenerator II*, CDF Note 5092.

[38] P. Nason, S. Dawson and R.K. Ellis, Nucl. Phys. **B303** (1988) 607; Nucl. Phys. **B327** (1989) 49.

[39] C. Peterson *et al.*, Phys. Rev. **D27** (1983) 105.

[40] W. Bell, J.P. Fernandez, L. Flores, F. Wuerthwein, R.J. Tesarek, *User Guide for* `EvtGen` *CDF*, CDF Note 5618.

[41] R. Brun, K. Hakelberg, M. Hansroul, and J.C. Lasalle, CERN-DD-78-2-REV; CERN-DD-78-2.

[42] A. Cerri, M. Rescigno, *The CDFII Realistic Simulation Package* - CDF Note in preparation.

[43] H.W. Zhao *Study of B Decays into the Final State $D^{(*-)}\pi^+\pi^+\pi^-$ at BaBar*, hep-ex/0409055.

[44] G. Punzi, *Sensitivity of Searches for New Signals and Its Optimization* eConf **C030908**, MODT002 (2003);
arXiv:physics/0308063.

[45] D. Acosta *et al.,* [CDF Collaboration] *Measurement of* $\mathcal{B}(\Lambda_b \to \Lambda_c\pi)/\mathcal{B}(B^+ \to D^-\pi^+) \cdot \sigma(\Lambda_b)/\sigma(B^+)$ CDF Note 7427.

[46] Frabetti *et al.,* [FNAL E687 Collaboration] PL B351 591, Dalitz fit, 701 evts.

[47] B^0 Mixing group *Updated Study of* B^0 *Oscillations* CDF Note 7722.

[48] S. Eidelman *et al.*, [Particle Data Group], Phys. Lett. B **592**, 1 (2004).

[49] S. Giagu *et. al.*, *Relative branching fractions and CP-violating decay rate asymmetries in Cabibo suppressed decays of the* D^0 *meson.* CDF Note 6391.

[50] K. Hagiwara *et al.*, [Particle Data Group], Phys. Rev. D **66**, 010001 (2002).

[51] M. Bishai *et. al., The Measurement of the b-hadron Inclusive Cross-section in CDF Run II using* $b \to J/\psi X$, CDF Note 6285,.